Modeling of Magnetic Optic for the Short Pulse Mode Operation of Energy Recovery Linac based Light Sources

DISSERTATION

zur Erlangung des akademischen Grades

doctor rerum naturalium
(Dr. rer. nat.)
im Fach Physik
Spezialisierung: Experimentalphysik

eingereicht an der
Mathematisch-Naturwissenschaftlichen Fakultät
Humboldt-Universität zu Berlin

von
Terry Atkinson

Präsident der Humboldt-Universität zu Berlin:
Prof. Dr. Jan-Hendrik Olbertz

Dekan der Mathematisch-Naturwissenschaftlichen Fakultät:
Prof. Dr. Elmar Kulke

Gutachter:
1. Prof. Dr. Alexander Matveenko
2. Prof. Dr. Eberhard Jaeschke
3. Prof. Dr. Kurt Aulenbacher

eingereicht am: 24.03.2015
Tag der mündlichen Prüfung: 03.09.2015

Abstract

Synchrotron light sources are entering a new era. No matter how elaborate, all the next generation proposals share a common necessity, the production of ultra-short electron bunches. There is an evolution in the field of science under investigation using the high peak brilliance generated from such bunches. The user community is demanding not just pictures but videos of atomic substructures and the processes that define them. Existing 3rd generation facilities are modifying their magnetic lattices and upgrading the acceleration schemes in order to keep up with this trend of generating short pulses with ultimate brilliance for time resolved experiments.

A possible candidate for the next generation light source is one based on ERL technology. Using long linacs to accelerate to high energies overcomes the present limitation of emittance equilibrium in storage rings. By implementing independent arcs for acceleration and deceleration while recuperating the beams energy, ERL based sources are theoretically capable of efficiently producing high energy femtosecond long bunch lengths. The study of the longitudinal motion of the beam through single pass magnetic optic in combination with linacs is the main topic of this thesis.

Dedicated start-to-end simulations in the framework of the Femto-Science Factory large scale light source are undertaken. The expectations and restrictions on the short pulse mode (SPM) operation are comprehensively examined in this work. Particular attention is given to the 6D electron beam properties and with it the beam degradation caused by the production of ultra-short bunches.

Intricate schemes that suppress transversal emittance growth due to radiation, reduce the effect of non-linear aberrations and recover the longitudinal emittance of the injector are presented. The effectiveness of these analytical tools and their associated optic are verified again using particle tracking simulations.

A potential weakness of offering a SPM in multi-turn ERL facilities is the longitudinal beam break-up instability. This instability due to the beam-cavity interaction and dispersive aspects of the time of flight in the recirculation optic can limit the beam current. The threshold currents first for simple and then more elaborate ERL facilities are estimated.

Experiments were performed to help characterize the longitudinal beam dynamics at two ERL accelerator laboratories. Models were used to explain the measured values in the low energy sections and optimize beam transport.

Keywords: ERL, beam dynamics, femtosecond short bunches, synchrotron radiation, emittance growth suppression, start-to-end simulations, longitudinal instability.

Zusammenfassung

Das Forschungsfeld der Synchrotronstrahlungsquellen hat sich in den letzen Jahren entscheidend weiterentwickelt. Alle Zukunftsideen, unabhängig von ihrer Komplexität, haben dennoch eines gemeinsam: die Erzeugung kurzer Pulse. Die Naturwissenschaften haben die Spitzenbrillanz, die mit Hilfe kürzester Pulse produziert werden kann, als neues Schlüsselwerkzeug entdeckt. Die Nutzergemeinschaft verlangt nicht mehr nur ein statisches Bild, sondern vielmehr eine Reihe von bewegten Aufnahmen atomarer Substrukturen und den dazugehöringen Prozessen. Existierende dritte Generation Synchrotronstrahlungsquellen werden an die neuen Herausforderungen angepasst: Verbesserungen an der Magnet-Optik sowie der Einbau modernster Beschleunigertechnologie ermöglichen die Erzeugung kürzester Pulse mit höchster Brillanz für zeitaufgelöste Experimente.

Ein möglicher Kandidat für die Lichtquelle der nächsten Generation ist ein Linear-Beschleuniger mit Energierückgewinnung. Durch die Verwendung langer Beschleunigungsstrukturen kann es, selbst bei hohen Energien, nicht zur Ausbildung des Emittanzgleichgewichts wie in Speicherringen kommen. Durch die Verwendung Impulsabhängiger-Umlaufbahnen und der Rückgewinnung der Strahlenergie ist es mit 'Energy Recovery Linac' (ERL)-basierten Quellen energieeffizient möglich, hochenergetische Elektronen-Pulse im Femtosekundenbereich zu erzeugen. Die longitudinale Elekronstrahldynamik solcher ERLs ist eines der Hauptthemen dieser Arbeit.

Umfangreiche Simulationen über die gesamte Maschine wurden im Rahmen der 'Femto-Science Factory' Lichtquellen Studie durchgeführt. Die Begrenzungen des Kurzpulsmodus Betriebes wurden untersucht und mit den Erwartungen verglichen. Besondere Aufmerksamkeit lag dabei auf den 6D Elektronenstrahleigenschaften, insbesondere auf der Vermeidung von Strahlaufweitungen, die mit der Erzeugung von Ultra-Kurzpulsen einhergehen können.

Im Rahmen dieser Arbeit wurden komplexe Schemata zur Überwindung verschiedener Limitierungen entwickelt, die das transversale Emittanzwachstum infolge der Emission von Synchrotronstrahlung reduzieren, den Einfluss nichtlinearer Effekte minimieren oder die longitudinalen Emittanz des Injektors wiederherstellen. Die Effektivität der abgeleiteten, analytische Lösungen und ihre magnetoptische Umsetzung wurde mit Hilfe von Teilchen-Tracking-Simulationen verifiziert.

Eine potentielle Schwachstelle des ERLs im Kurzpulsmodus ist die 'Longitudinal Beam Break-Up' Instabilität, die durch eine Strahl-Kavitäten Wechselwirkung im Zusammenspiel mit der Energieabhängigkeit der Umlaufzeit den erreichbaren Strom begrenzen kann. Dieser Grenzstrom wurde zunächst für vereinfachte, danach für komplexe ERLs abgeschätzt.

Verschiedene Experimente an zwei ERL Beschleunigern haben dazu beigetragen, deren longitudinale Elektronstrahldynamik näher zu charakterisieren. Anhand von Modellen wurden die gemessenen Werte im Niederenergiebereich erklärt und Optimierungen beim Strahltransport vorgenommen.

Contents

1. Introduction

The motivation for this thesis is driven by the high demand of the next generation of light sources. With over half a century of affluent history which started out as a parasitic effect in ring based colliders, Synchrotron Radiation (SR) is out coupled from these accelerators across the world to many hundreds of users per year. Dedicated facilities presently in their 3rd generation circulate high average current beams to produce light from infrared to hard X-ray wavelengths to dozens of user stations at any one time. There are steady state equilibriums associated with storage rings that limit the bunch properties. The next generation promise to relieve these physical restraints.

The modern trend is proposals based on linear accelerators (linacs). The quality of the electron beam, and hence the emitted light, is determined by the source. The main advantage over storage rings is the possibility using linacs to preserve the initial emittance from the injector. The transverse emittance is adiabatically damped during acceleration therefore the normalized emittance can be used as a figure of merit. In order to maximize the efficiency, facilities based on Energy Recovery Linac (ERL) technology are of immediate interest. With an ERL the beam is not stored, there is only one single pass per bunch so no equilibrium is reached and the beam properties remain flexible. Here, recuperation of the beam energy after acceleration is achieved using dedicated optic to deliver the beam back to the same linac for deceleration. The energy of the decelerated beam is recuperated into the linac cavities where it can be reused to accelerate the next fresh bunch [1]. The beam is dumped safely at a reasonable energy and the power supply requirement for the linac is reduced in sense, to maintaining the electromagnetic fields. This means that high current electron beams of many GeV energies can be produced and maintained with a few MW of power.

The most plenteous multi-turn ERL is the NovoFEL facility in Russia [2]. Here normal conducting RF linacs are used to drive multiple Free Electron Lasers (FEL) to produce coherent light. The global tendency however is towards facilities based on superconducting RF (SRF) technology. The most advanced of which is the Jlab ERL in the USA [3]. Only with SRF technology can the acceleration of high average current beams of low energy spread and ultra-short electron bunches of high brilliance be achieved. These critical beam parameters that are reaching their limit for storage ring based light sources are investigated in this thesis.

The technological challenges associated with SRF ERLs are researched in compact test facilities such as ALICE in the UK [4]. The operational thresholds of low energy, high duty beams are becoming more reliable and beam quality is under constant scrutiny. Future large scale facility upgrades [5] need to operate in a non-linear high charge, ultra-short pulse regime where collective effects play a major role in order to produce light that a storage ring cannot. Beam quality preservation using emittance compensation schemes are seen as a prerequisite to operation in this complex system. Theoretical investigations in this thesis give an insight into the phase space evolution and the fundamental limitations expected when producing an ultra-short bunch.

The desire for Short Pulse Mode (SPM) operation has triggered a series of workshops throughout the

user and accelerator facility community. Science such as that at the hard X-ray diffraction limit [6] is often discussed. Organizers and participants focus their incentives on the science achievable using the next generation of beams. In order to better understand complex materials, improvements in time resolution measurements from pico (ps) to femtosecond (fs) studies are a recurring theme [7]. Examples such as the reluctance of certain proteins to crystallize can be overcome by sequentially studying the diffraction pattern of a stream of crystal microdrops during nucleation [8] at kHz rates on fs timescales.

Not all structures can be nor need to be crystallized. Through dedicated 'Tickle and Probe' [9] experiments, the transport of excitation energy within biomimetic molecules can be studied. Temporal (sub-ps) and spatial (nm) resolution enable X-ray scattering measurements to produce a description of the valence excitations in real-time. The concept of real-time observation is becoming an essential tool in understanding fundamental chemical reactions the community has simply taken so far for granted. Recently, catalytic processes on the surface of carbon monoxide [10] have been investigated using high intensity, ultra-short X-rays produced by a FEL.

The abundance of light produced from next generation light sources reflects well with the amount of publications and new applications in physics. Taking for example the FEL at Jlab in the final few years before the shutdown for the upgrade, the list is extensive [11]. The full range of these studies is beyond the scope of this thesis.

The Extreme Ultraviolet Lithography (EUVL) community is actively searching for the next generation of EUV sources [12]. Presently EUV optics is associated with the production of etched substrates at a wavelength of 13.5 nm. The industry is particularly interested in accelerator technology as production at scales lower than this wavelength would require kW average output power. Foreseen is a facility that will embrace the ultra-bright light produced during the FEL process with the high repetition rates and the efficiency of ERLs.

The motivation is clear for SPM operation, even more so that 3rd generation machines are now modifying their optics and power supplies [13] or installing multiple SRF cavities [14] in order to implement short pulse low-α optic. Here though the bunch length is restricted to at best 1 ps. To date fs science at these facilities is associated with bunch slicing techniques [15] rather than using the full bunch properties. The next generation needs to produce optic for fs scale bunch lengths without these restrictions.

The remainder of this chapter finishes with an introduction to linear magnetic optic and the description of particle motion in six-dimensional (6D) phase space. The second chapter familiarizes the reader with the general theories of the restrictions on the bunch properties due to radiation effects. Analytical expressions are derived from these fundamental arguments which are then referred to throughout. The third and fourth chapters present the experimental aspects of longitudinal motion. The injector bunch length and energy spread are measured at a SRF compact ERL and dedicated studies into longitudinal dispersion measurements are undertaken. The fifth chapter describes the theoretical methods one can use to compensate for the radiation effects that are intrinsic to short bunch operation. Novel approaches are given and validated through particle tracking simulations. The sixth and longest chapter presents the relevant work from the young investigators group at the Hemholtz-Zentrum Berlin. A candidate for a fourth generation light source is introduced. The Femto-Science Factory (FSF) is intended to be a multi-turn 6 GeV ERL based accelerator. Although the main operation mode is designed for high average brilliance (low transversal emittance) the magnetic optic can also be tuned to generate 10 fs bunches. The results of the start-to-end particle tracking simulations are given. The chapter also establishes a third operational mode to produce

an electron bunch capable of generating a FEL from the undulators. High repetition rate combined with coherent emission highlights the great potential of this mode. The final chapter reports on the methods used to estimate the longitudinal stability of ERLs.

Matrix multiplication [16] is a common way to express the transport of a particle through a system of magnets. By representing the particle position, angle and momentum with respect to a specified reference trajectory as a vector, one can describe the action of the magnet on the particles coordinates using the transport matrix R

$$X_1 = RX_0 \tag{1.1}$$

where $X_0 = \left(x, x', y, y', c\Delta t, \delta\right)_0$. x is the horizontal coordinate, x' is the slope and likewise for the vertical coordinate y. The path length difference $c\Delta t$ and fractional momentum deviation $\delta = \Delta p/p$ make up this typical accelerator theory description of particle motion in 6D phase space. An alternative description using canonical variables is discussed in Chapter 4.1.2.

This tracking principle is analogous to the tracing of rays through an optical system of lenses. Particles simply continue on their trajectory through the open space that is a drift. A bend introduces a dispersive aspect to the particle trajectory. This energy dependent aspect of the particle coordinate plays an essential role in this thesis. Quadrupoles are used to act like a lens to focus and defocus the beam. Together these linear elements can be used to control the longitudinal dispersion R_{56} and transform the initial particle coordinates to produce a shorter bunch, as described in Chapter 3.1.

Liouville's theorem states that the density of the phase space remains constant under the influence of conservative forces. This allows one to independently represent the particles in the beam to occupy a certain region in phase space called the beam emittance ε. The longitudinal emittance is given by

$$\varepsilon_z^2 = \langle (c\Delta t)^2 \rangle \langle \delta^2 \rangle - \langle c\Delta t \delta \rangle^2 \tag{1.2}$$

The 1σ phase ellipse shown in Fig. 1.1 is used to describe the emittance invariant

$$\varepsilon_z = \gamma (c\Delta t)^2 + 2\alpha (c\Delta t)\delta + \beta \delta^2 \tag{1.3}$$

where $\alpha,\ \beta,\ \gamma$ are the Twiss-parameters that describe the geometric properties of an ellipse such that $\beta\gamma - \alpha^2 = 1$. The betatron function β describes an envelope surrounding the particles as the beam propagates. The same principle of phase space distributions is used for all planes. The electron

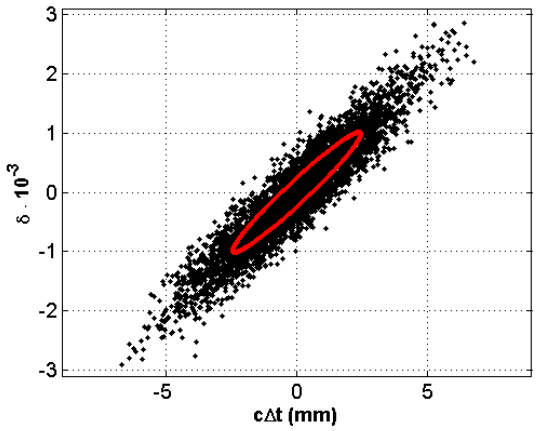

Figure 1.1: Ellipse in phase space representing the longitudinal emittance in $c\Delta t, \delta$ plane.

beam size is given by both the transversal geometrical emittance and the relevant energy dependent terms

$$\sigma_x = \sqrt{\varepsilon_x \beta_x + \eta_x^2 \sigma_E^2} \tag{1.4}$$

where η_x is the value of the horizontal dispersion and σ_E is the relative energy spread of the beam.

In order to more rigorously study beam optics, the matrix calculation is truncated to higher orders using a Taylor expansion about the reference trajectory as investigated in Chapter 5. Collective effects common to high charge, ultra-short bunches modify the 6D phase space defining the beam transition through the optic and requires dedicated particle tracking simulations as presented in this thesis.

2. Bunch Length Restrictions due to Radiation Effects

This chapter introduces the restrictions on the bunch length due to radiation. Light sources are so conceived to transport bunches of electrons through magnetic optic and generate radiation. Simply by doing so, the longitudinal properties of the bunch are constrained. If the energy of a particle in the bunch changes, then its arrival time varies accordingly and limits the fundamental bunch length.

The first section in this chapter develops the general theory of electromagnetic fields associated with a moving particle for the far field ultra-relativistic case. The interaction theory of the fields within a bunch is continually referred to throughout the thesis as it plays a crucial role in beam degradation.

The second section estimates the fundamental bunch length due to incoherent synchrotron radiation (ISR). Radiation effects due to the quantum fluctuations that increase the energy spread of a populated bunch through a standard optic are investigated. The heavy dependence on particle energy is analytically derived and the zero-current bunch length for the FSF is estimated.

The final section highlights the more damaging effects due to coherent synchrotron radiation (CSR). The power of the electromagnetic field dependence on the bunch length is presented. A two electron model is described and developed into a rectangular bunch model, as commonly found in literature. The energy change of the front electron due to the radiation emitted from the trailing electrons is used to approximate the increase in energy spread across the bunch. The investigations indicate that for a bunch charge greater than 1 pC, the minimal bunch length achievable in the FSF is determined by CSR effects.

2.1 Synchrotron Radiation in a Bending Magnet

The Lienard-Wiechert potentials describe electromagnetic fields emitted from a single particle moving on an arbitrary trajectory. The potentials φ and A can be found rigorously following [17] using the wave equations. When the emitted field from the particle at point P' is observed at point P, the particle will have continued on its trajectory with velocity $v = \beta c$. The general principle of the retarded notion at an observation point a distance L away is shown in Fig. 2.1.

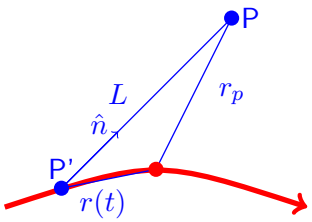

Figure 2.1: General coordinates of the Lienard-Wiechert potentials.

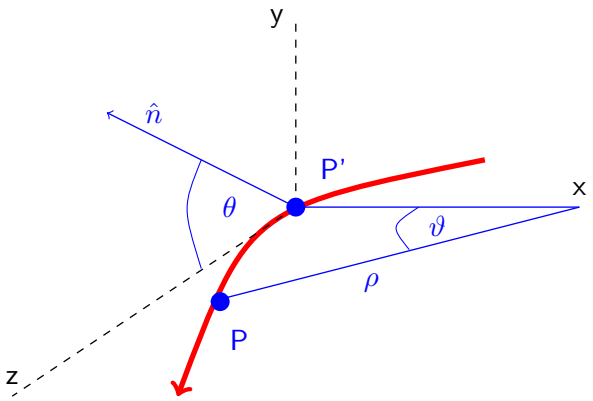

Figure 2.2: Circular coordinates of a x-z bending plane.

The potentials can be simplified to

$$\varphi = \frac{e}{L} = \frac{e}{|r_p - r(t)|} \qquad A = \frac{ev}{L} = \frac{ev}{|r_p - r(t)|} \tag{2.1}$$

where $t - t' = L/c$. The electric field associated with these potentials is given by

$$\mathcal{E} = -\nabla\varphi - \frac{\partial A}{\partial t} \tag{2.2}$$

one finds

$$\mathcal{E} = \frac{e}{4\pi\epsilon_0}\left[\frac{1}{\gamma^2 L^2}\frac{(n-\beta)}{(1-n\cdot\beta)^3} + \frac{n\times[(n-\beta)\times\dot{\beta}]}{cL(1-n\cdot\beta)^3}\right] \tag{2.3}$$

The first term in Eq. (2.3) is the Coulomb field and is independent of the acceleration $\dot{\beta}$. It is proportional to $1/(\gamma L)^2$ and does not contribute to the radiation of energy in the far field in the ultra-relativistic limit. The second term however describes such field and is often referred to as the radiation term.

In order to comprehensively describe these radiation effects in a magnet, the point P is shifted to a point on the trajectory in the bending plane as shown in Fig. 2.2. Consider a magnet of bending radius ρ so that $L = 2\rho\sin(\vartheta/2)$. Using the Cartesian components for circular motion in a bending plane,

$$r = \Big(\rho\big(1-\cos\vartheta\big), 0, \rho\sin\vartheta\Big) \qquad n = \Big(0, \sin\theta, \cos\theta\Big)$$

where angle $\vartheta = \beta ct/\rho$, the electric field Eq. (2.3) in the direction of motion to the radiation field becomes

$$\mathcal{E}_z = \frac{e\beta^2\cos(\vartheta/2)\sin^2\theta}{\rho^2\big(1-\beta\cos\theta\cos\vartheta\big)^3} \tag{2.4}$$

This solution can be readily used to plot the radiation field for a given velocity.

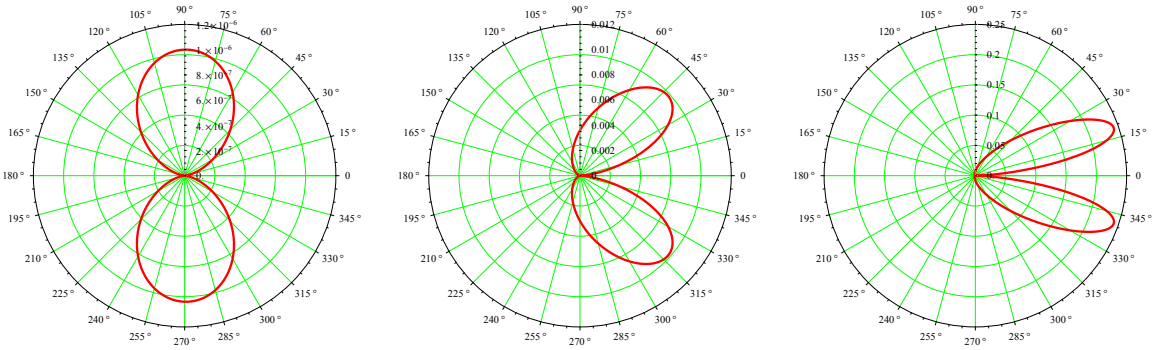

(a) $\beta \sim 0$ (b) $\beta = 0.6$ (c) $\beta = 0.9$

Figure 2.3: Radiation field polar plots due to particle velocity.

Fig. 2.3 shows the evolution of the angle of maximum radiation field with increased particle velocity from the dipole rest frame Fig. 2.3a to the relativistic lobe shown in Fig. 2.3c. The inclination angle of maximum radiation field in the relativistic limit can be approximated from the polar plots as $\theta \sim \sqrt{1-\beta^2}$

Fig. 2.4 shows that as the particle becomes ultra-relativistic a significant increase in the radiation power occurs and the radiation is spread solely in the direction of the velocity.

These geometric considerations for a moving charge have introduced an intense projection of the electric field in the direction of motion for ultra-relativistic particles. The notion that the observation point of such radiation is moved into the bending plane is developed further in Chapter 2.3.1 to describe a two electron model. The following section introduces the incoherent nature of radiation in a bunch. Statistical fluctuations due to such incoherent radiation cause an energy spread and fundamentally limit the minimum bunch length.

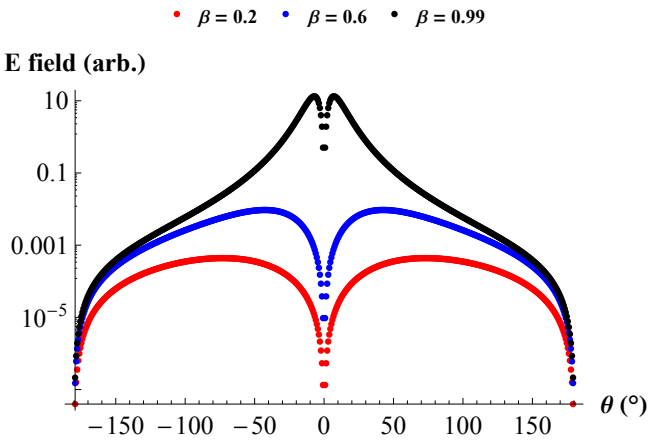

Figure 2.4: Radiation power over the polar angle as the particle velocity increases.

2.2 Quantum Fluctuations Estimation

Bunch lengthening occurs because quantum fluctuations of synchrotron radiation increase the energy spread of the beam. Therefore, less energetic particle trajectories slip during the passage through the bend and cause a time delay due to dispersion. For an arc of length L, the trajectory delay caused by the emission of a photon is given by

$$c\Delta t = -R_{56}(s, L)\frac{\hbar\omega}{E_b} \tag{2.5}$$

The probability of this photon emission can be expressed in terms of its spectral power density [18] using the delay function

$$\sigma^2_{c\Delta t} = \left\langle (c\Delta t)^2 \right\rangle - \left\langle (c\Delta t) \right\rangle^2 \tag{2.6}$$

The delay is the sum of the ds trajectory contributions within a frequency dω and is given by

$$\sigma^2_{c\Delta t} = \frac{55}{24\sqrt{3}}\frac{r_0^2}{\alpha}\gamma^5 \int_0^L \frac{R_{56}^2}{\rho^3}\,\mathrm{d}s \tag{2.7}$$

where r_0 and α are the classical electron radius and the fine structure constant respectively. This statistical energy spread approach depends heavily on the beam energy γ. For a fixed radius of curvature, Eq. (2.7) can be simplified and expressed as a relative bunch length

$$\frac{\Delta\sigma^2}{\gamma^5} \sim \int_0^L \frac{R_{56}^2}{\rho^3}\,\mathrm{d}s \tag{2.8}$$

Fig. 2.5 introduces a simple isochronous Triple Bend Achromat (TBA) lattice on which this quantum fluctuation estimation can be studied. A beamline is isochronous when the time of flight rather than the path length is equal for all particles. As the name suggests, in a TBA the middle dipole is separated from the outer two by three quadrupoles. The common quadrupole scenario is that the sum of the two outer ones combine to be approximately equal but opposite the middle one. The profile plotted in blue symbolizes the magnetic arrangement. Black and red show the horizontal and longitudinal dispersion R_{56} respectively.

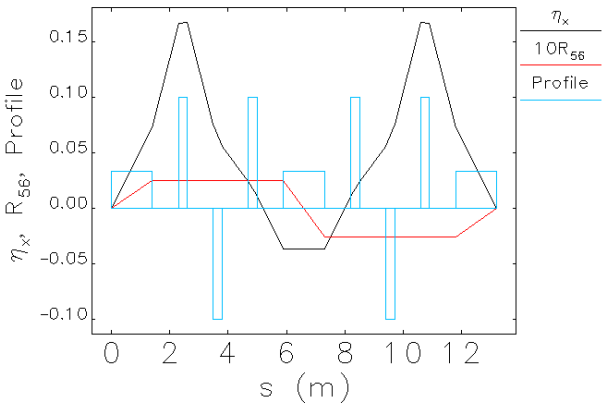

Figure 2.5: Dispersion functions of an achromatic and isochronous TBA lattice.

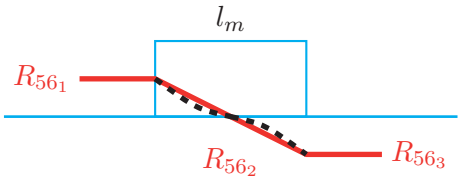

Figure 2.6: Linear approximation of R_{56} through the middle dipole.

Taking the first dipole with a small angle approximation

$$R_{56_1} = \rho(\sin\theta - \theta) \sim \frac{\rho\,\theta^3}{3!} \xrightarrow{s=\rho\,\theta} \frac{s^3}{6\rho^2} \tag{2.9}$$

$$\frac{\sigma_1^2}{\gamma^5} \sim \frac{1}{36}\int_0^L \frac{s^6}{\rho^7}\,\mathrm{d}s = \frac{\theta^7}{252} \tag{2.10}$$

In an identical manner the relation for the third dipole can be readily deduced.

$$\frac{\sigma_3^2}{\gamma^5} = \frac{\theta^7}{252} \tag{2.11}$$

In the middle dipole one can assume R_{56} is curvature independent and falls linearly with distance as shown in Fig. 2.6.

$$R_{56_2} = \frac{L^2}{3\rho^2}\left(\frac{L}{2} - s\right) \tag{2.12}$$

$$\frac{\sigma_2^2}{\gamma^5} \sim \int_0^L \frac{L^4}{9\rho^7}\left(s^2 - sL - \frac{L^2}{4}\right)\mathrm{d}s = \frac{\theta^7}{108} \tag{2.13}$$

The understanding of this is simply that the middle dipole of the TBA shown in Fig. 2.5 compensates for the outer dipoles to nullify R_{56} and hence contributes approximately double to the R_{56} integral. Since $\sigma^2 \sim \gamma^5$ these $\sigma_{1,2,3}$ relations can be used to estimate the impact of quantum fluctuations for future high energy light sources. Taking the FSF case study in Chapter 6 as an example the total contributions of all beam energies to the bunch length from quantum fluctuations depending on the bending angle $\theta = l_m/\rho$ are given in Table 2.1.

Table 2.1: FSF bunch length due to quantum fluctuations.

Bend angle θ (°)	5	10	15
Bunch length (fs)	0.12	1.31	5.40

The FSF was initially intended to be a low transverse emittance facility. The bending angle was intuitively chosen to be between 5 and 10 ° to keep the emittance growth small, see Chapter 6.3. In this case the results from Table 2.1 show that the contribution from quantum fluctuations will limit the bunch length to a femtosecond. This incoherent radiation theory is independent of bunch charge and presents theoretical zero-current values for the bunch length. The following section investigates the radiation effects within a charged bunch of realistic length.

2.3 Coherent Synchrotron Radiation

A model describing incoherent statistical fluctuations has been used in the previous section to find a fundamental limit on the bunch length. Choosing an appropriate optic one can suppress this incoherent limit to a 1 fs. A more damaging limitation on the fundamental bunch length is due to the coherent nature of radiation. As the name suggests, when the bunch length becomes comparable to the emitted wavelength, the electrons start to emit coherently as one and the power P, scales with the square of the number of particles N so that

$$P(\omega) = p(\omega)\left[N + N(N-1)g^2\right] \tag{2.14}$$

where $p(\omega)$ is the power of a single electron and g is a form factor that depends on the bunch length and wavelength λ.

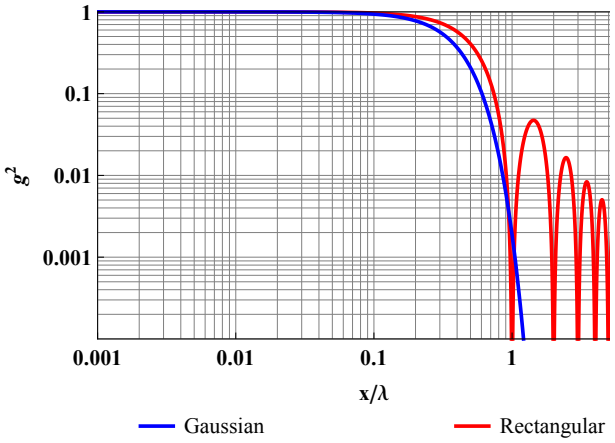

Figure 2.7: CSR form factor for a Gaussian and rectangular bunch.

Fig. 2.7 shows the CSR power spectrum form factor as a function of bunch length for two common bunch distributions. One can see that the CSR form factor $g^2 \to 1$ for wavelengths greater than the bunch length $x < \lambda$ and maximum coherent power is achieved for bunch lengths $x < 0.1\lambda$ in both cases. The spectrum of the rectangular distribution extends at higher frequencies compared to its Gaussian counterpart, as it contains sharp extremities in its particle density which require a broader spectrum in the Fourier transform [19]. In the following subsections models will be used to describe the change in energy of the front electrons due to the emission of radiation of the trailing electrons within a short bunch. This in turn causes a non-linear energy loss along the bunch and increases the longitudinal emittance and hence limits the fundamental minimal bunch length.

2.3.1 Two Electron Model

The Lienard-Wiechert formula Eq. (2.3) for a moving charge about an arbitrary trajectory was previously introduced and simplified to Eq. (2.4) to describe the radiation field. Consider now a two particle system in the framework of the model of circular motion of an electron depicted in [20]. The radiation field of the trailing electron produced at a retarded point P' at time t' reaches the front electron at a later time t at point P, as shown in Fig. 2.8.

The radiation field Eq. (2.4) neglects the Coulomb term and describes the radiation as solely in the direction of motion. The rate of energy change dW/dt of the front electron due to radiation from

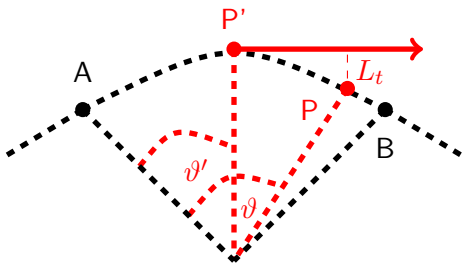

Figure 2.8: Radiative interaction of two electrons moving on a circular trajectory.

the trailing electron is given by

$$\frac{\mathrm{d}W}{\mathrm{d}t} = e\frac{\mathrm{d}r}{\mathrm{d}t}\cdot\mathcal{E} \tag{2.15}$$

and the energy loss due to CSR can be approximated as

$$\Delta E_{\mathsf{CSR}} \sim ev\cdot\mathcal{E}_z \tag{2.16}$$

$$\Delta E_{\mathsf{CSR}} = \frac{e^2\beta^3\cos\theta\cos\left(\vartheta/2\right)\left(\beta-\cos\theta\cos\vartheta\right)}{\rho^2\left(1-\beta\cos\theta\cos\vartheta\right)^3} \tag{2.17}$$

Substituting $\beta = 1$ and $\theta = 0$ the estimation simplifies to

$$\Delta E_{\mathsf{CSR}} = \frac{e^2\sin\vartheta}{8\rho^2(\sin\vartheta/2)^5} \tag{2.18}$$

Here, the retarded angle $u = (\vartheta - \vartheta')$ and the distance $(s - s')$ between the electrons remains within the magnetic boundary A $\rightarrow$ B under the small angle approximation. Taylor series expansion of ϑ leads to

$$\Delta E_{\mathsf{CSR}} \simeq \frac{4e^2}{\rho^2u^4} + \ldots \tag{2.19}$$

The slippage length can be used to define the bunch length criteria for the distance $(s - s')$ in which these cooperative effects materialize

$$(s-s')_{\mathsf{max}} = \mathsf{arc(P'P)} - |\mathsf{P'P}| \simeq \frac{u^3\rho}{24} \tag{2.20}$$

For the lower boundary as $\beta \rightarrow 1$ then $(s - s')_{\mathsf{min}} \rightarrow 0$ allowing

$$(s-s')_{\mathsf{min}} = (1-\beta)\rho u \tag{2.21}$$

These two boundary conditions form the relation

$$(s-s') = u(1-\beta)\rho + \frac{u^3\rho}{24} \tag{2.22}$$

therefore the overtaking angle $u = \left[\frac{24(s-s')}{\rho}\right]^{1/3}$ gives the typical distance $L_0 = u\rho$ required for the radiation to catch up the front electron. This relation can be inserted into Eq. (2.19) to give the commonly known steady state approximation.

$$\Delta E_{\mathsf{CSR}} \simeq \frac{e^2}{\rho^{2/3}(s-s')^{4/3}} \tag{2.23}$$

Another useful geometrical condition, the characteristic transverse distance [21],

$$L_t = \frac{uL_0}{2} = 2\big(9(s-s')^2\rho\big)^{1/3}$$

arises from the retarded cooperative radiation process depicted in Fig. 2.8. This distance can be readily compared to other transversal parameters such as bunch size and vacuum chamber diameter to estimate when CSR shielding is important [22], or if a 1D CSR wake model is sufficient, see Chapter 6.6.

Although described in this subsection as a model using just two electrons, one can already appreciate that the CSR effect depends heavily on the position within the bunch $(s-s')$ and hence the total bunch length σ_z. To further develop this theory one can associate a density function F that describes the 'wake' as a non-linear energy loss throughout the bunch at position s and the number of charged particles N

$$\Delta E_{\text{CSR}} \simeq \frac{1}{4\pi\epsilon_0}\frac{Ne^2}{\rho^{2/3}\sigma_z^{4/3}}F(s/\sigma_z) \tag{2.24}$$

Fig. 2.9 shows the rate of an electron energy change as a function of its position along the Gaussian bunch passing through a magnet as a solid blue line where

$$F(\xi) = \int_{-\infty}^{\xi}\frac{\mathrm{d}\xi'}{(\xi-\xi')^{1/3}}\frac{\mathrm{d}}{\mathrm{d}\xi'}\,e^{-(\xi)^2/2} \tag{2.25}$$

Also shown as a dashed line is the bunch profile. The parameters were chosen with the high energy arcs of the FSF in mind. For the SPM one excepts $q = 5\,\text{pC}$, $\rho = 15\,\text{m}$ and $\sigma_t = 20\,\text{fs}$. The head of the bunch is given to the LHS of the origin and is seen to be energy modulated due to CSR.

One can integrate the interpolation of the two curves to estimate the energy loss due to CSR for a Gaussian bunch in a typical bend in the FSF arcs as $\Delta E_{\text{CSR,bend}}$ = -0.04 MeV/m. Given the arcs contain 48 bending magnets, each a metre long, then the total loss is comparable with the results in Table 2.2 in the follow section. Here a more elaborate analytical expression is derived for the transient nature of the CSR produced from a rectangular bunch entering, passing through and exiting a bend.

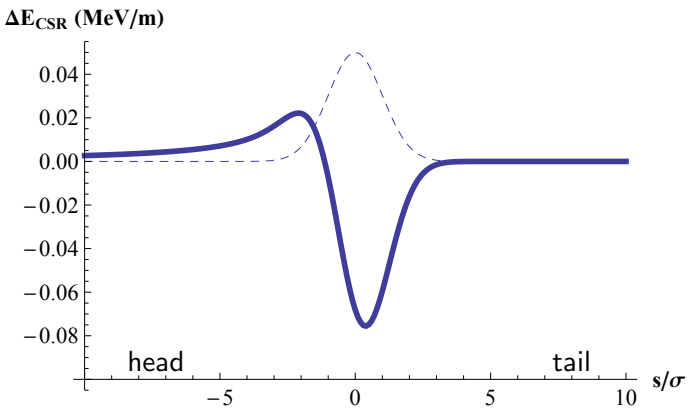

Figure 2.9: Steady state CSR induced energy loss of an electron in a Gaussian bunch.

2.3.2 Rectangular Bunch Model

Consider the coherent radiation of a rectangular bunch as comprehensively introduced in [20], passing through a bending magnet with the conditions; 'long' magnet, 'long' bunch and magnet is 'longer' than bunch. A linear charge density is assumed.

Fig. 2.10 to Fig. 2.12 show an electron at point s within the bunch at angle ϑ_s entering, passing through and exiting a magnet. In these three regimes, the density function F is given by Eq. (2.26) Eq. (2.27) and Eq. (2.28) respectively. ϑ_m and ϑ_b are the angles suppressed between the magnet and the extremities of the electron bunch. In this model the limits $\vartheta_m \gg 1$ and from Eq. (2.22), $\vartheta_b \simeq \sqrt[3]{24 l_b} \gg 1$ exist. The radiation interaction region of the bunch is chosen as one sigma $2^{-\frac{2}{3}}\vartheta_s$ about the bunch length l_b.

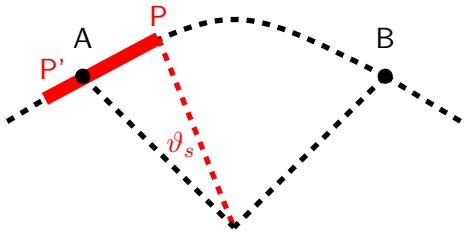

Figure 2.10: Bunch entering the bend.

$$F_1 \propto \begin{cases} 0 & \vartheta < 2^{-\frac{2}{3}}\vartheta_s \\ -1/\vartheta & 2^{-\frac{2}{3}}\vartheta_s < \vartheta < \vartheta_s \end{cases} \tag{2.26}$$

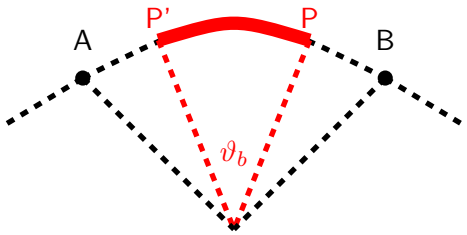

Figure 2.11: Bunch within the bend.

$$F_2 \propto -\frac{1}{\vartheta} \qquad \vartheta_s < \vartheta < \vartheta_m \tag{2.27}$$

As the bending angle is small, one can introduce a decay term defined over the slippage length $2s$, On exiting the magnet the interaction region is much larger than ϑ_s.

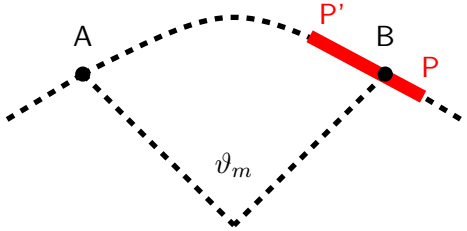

Figure 2.12: Bunch exiting the bend.

$$F_3 \propto -\frac{1}{\vartheta} + \frac{1}{s} \qquad \vartheta_s \ll \vartheta < 2s \tag{2.28}$$

Table 2.2: Estimation of energy loss and spread in a bunch due to CSR for the 6 GeV arc.

q (pC)	σ_t (fs)	ΔE_{CSR} (MeV)	P_{CSR} (kW)	ΔE/E 10^{-4}
5	20	4.0	26	6.7
5	15	5.6	37	9.4
1	10	1.8	2.4	3.0

Summation of these integrals across the bunch

$$\Delta E_{\mathsf{CSR}} = \int_{2^{-2/3}\vartheta_s}^{\vartheta_s} \Delta E_{\mathsf{CSR}}(F_1)\,\mathrm{d}\vartheta + \int_{\vartheta_s}^{\vartheta_m} \Delta E_{\mathsf{CSR}}(F_2)\,\mathrm{d}\vartheta + \int_{\vartheta_m}^{2s} \Delta E_{\mathsf{CSR}}(F_3)\,\mathrm{d}\vartheta \tag{2.29}$$

allows one to analytically describe the total energy loss of the bunch per n bends and is given by

$$\Delta E_{\mathsf{CSR}} \simeq -\left(\frac{3^{2/3}\,q^2}{\rho^{2/3}\,l_b^{4/3}}\right)(\rho\,\vartheta_m)\left(1+\frac{3^{1/3}4}{9}\,\frac{l_b^{1/3}}{\rho^{1/3}\,\vartheta_m}\left[\ln\left(\frac{l_b\gamma^3}{\rho}\right)-4\right]\right) \tag{2.30}$$

This formula includes the steady-state term already derived in Eq. (2.24) and a logarithmic term that describes the additional energy loss on exiting the magnet. Taking the design parameters of the FSF in Table 6.1 one can calculate the expected power of the CSR wake

$$P_{\mathsf{CSR}} = \frac{n}{4\pi\epsilon_0} f_0 \Delta E_{\mathsf{CSR}} = \frac{f_0\,q^2\rho^{1/3}}{4\sqrt[3]{2}\,\epsilon_0\,\sigma_z^{4/3}}\left(1+n\,\frac{2\sqrt[3]{2}}{3\pi\sqrt{3}}\,\frac{\sigma_z^{1/3}}{\rho^{1/3}}\left[\ln\left(\frac{\sqrt{12}\sigma_z\gamma^3}{\rho}\right)-4\right]\right) \tag{2.31}$$

and with it estimate the energy spread of the beam in the 6 GeV arc as

$$\frac{\Delta E}{E} = \frac{P_{\mathsf{CSR}}}{I_b E_b} \tag{2.32}$$

where $l_b = \sqrt{12}\sigma_z$ and $\vartheta_m\, n = \pi$. A simple approximation for the minimum rms energy spread required for the optimum radiation from the 3000 period long undulator section is $\sigma_{\scriptscriptstyle E} \sim 1/N_{\mathsf{u}} = 3.3\cdot 10^{-4}$. The values estimated in Table 2.2 for a rectangular bunch are comparable to $\sigma_{\scriptscriptstyle E}$. This means that CSR will increase the energy spread above the minimum value of $\sigma_{\scriptscriptstyle E}$ needed for high peak brilliance radiation from the undulators. The results also indicate that a reduced charge $q < 5$ pC will be required to produce a 10 fs long bunch with an acceptable energy spread. This notion is verified using particle tracking simulations in Chapter 6.4.3.

The slippage length of the undulator emitting at wavelengths of 1Å is $N_{\mathsf{u}}\lambda = 0.3\,\mu$m $\Rightarrow$ 1 fs. Therefore, the light from the bunch tail will not overtake the head in the undulator. The calculation would be more accurate if the sliced energy spread was taken into account. The properties of individual slices within a bunch are developed further in Chapter 6.6 as part of the FEL studies.

The next two chapters report on the experimental procedures and the measurements to characterize the key longitudinal beam parameters at low energies of ERL based light sources.

3. The ALICE Compact ERL

To exploit new fields in synchrotron radiation research, new compact light sources based on energy recovery accelerators are under development worldwide. The UK ERL light source, ALICE (Accelerators and Lasers In Combined Experiments), at Daresbury has been operating in a recovery modus since December 2008. The machine is used for a wealth of different experiments [23]. Focus in this thesis is on the common machine layout Fig. 3.1, and how the magnetic optic is designed to generate a short pulse.

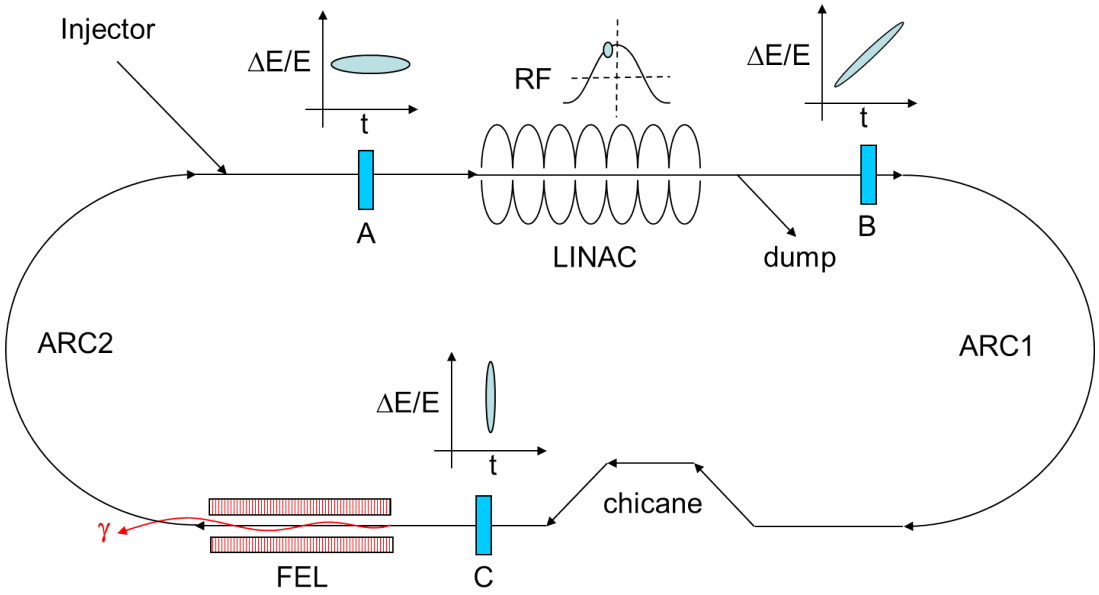

Figure 3.1: Schematic of the compact ERL ALICE.

A photoinjector is used to generate a picosecond electron bunch of high charge. Following a merger section the low energy 5 MeV electron bunch enters the ERL ring at position A and is accelerated to a maximum energy of 50 MeV using a SRF linac. In order to compress the bunch in following sections, the acceleration is slightly off-crest imprinting a correlated energy spread on the longitudinal phase space, seen at position B.

The ALICE outgoing achromatic ARC1 is either set as isochronous or used to slightly compress the bunch and to optimize the transversal beam parameters. Historically, only the chicane is used for

Table 3.1: ALICE parameters for FEL operation.

Beam Energy	Rep. Rate	Charge	Bunch length
26.5 MeV	16.25 MHz	60 pC	1 ps

compression since one of the out coupling mirrors of the FEL, is strategically positioned within the space encompassed by the chicane. There is no reason why ARC1 could not be used for compression as it contains all the relevant optic; dipoles to generate and quadrupoles to control the longitudinal dispersion, and sextupoles to correct 2nd order effects. Instead however, a chicane composing of four simple dipoles is used to manipulate the longitudinal parameters. After the chicane the longitudinal phase space at position C should be vertically upright depicting the shortest bunch and largest energy spread. Although the chicane breaks the symmetry of this compact ERL machine, it is more than adequate to provide full compression when the injector properties are optimized. See Chapter 3.2. for injector measurements.

After passing trough the FEL the bunch is then returned to the SRF structure via ARC2. In turn, the optic in ARC2 is set to increase the bunch length back to the original injection value of a few picoseconds. The path length $(N+1/2)\lambda_{\mathrm{RF}}$ is chosen such that deceleration and energy recovery is possible before the bunch is safely dumped.

3.1 Generating a Short Bunch

The dipole magnets of the chicane shown in Fig. 3.2, are used to generate the required longitudinal dispersion R_{56} for full compression. The transport matrix R that describes the action of a single sector dipole magnet (SECT) on the particle coordinates $0 \rightarrow 1$ is given by

$$\begin{pmatrix} x \\ x' \\ y \\ y' \\ c\Delta t \\ \delta \end{pmatrix}_1 = \begin{pmatrix} \cos\theta & \rho\sin\theta & 0 & 0 & 0 & \rho(1-\cos\theta) \\ -\frac{1}{\rho}\sin\theta & \cos\theta & 0 & 0 & 0 & \sin\theta \\ 0 & 0 & 1 & \rho\theta & 0 & 0 \\ 0 & 0 & 0 & 1 & 0 & 0 \\ -\sin\theta & \rho(\cos\theta-1) & 0 & 0 & 1 & \rho(\theta-\sin\theta) \\ 0 & 0 & 0 & 0 & 0 & 1 \end{pmatrix} \begin{pmatrix} x \\ x' \\ y \\ y' \\ c\Delta t \\ \delta \end{pmatrix}_0 \tag{3.1}$$

The transversal beam properties are given in the upper 4x4 section of the matrix and the longitudinal surround them. The energy dependent (dispersive) elements in the horizontal bending plane are $\eta_x = R_{16}$, $\eta'_x = R_{26}$ and the relevant bunch length elements are

$$c\Delta t_1 \quad = \quad R_{51}x_0 + R_{52}x'_0 + c\Delta t_0 + R_{56}\delta_0 \tag{3.2}$$

Particles follow trajectories depending on their energy through the chicane shown in Fig. 3.2. Particles with energies greater (red) than the reference (green) take a shorter path through the chicane. Those with lower energies (blue) follow a longer path. The net effect is that the particles arrive at the chicane exit at a more similar time, hence shortening the bunch length. Absolute compression is not possible even in this linear approximation as the bunch has an initial energy spread created at the injector.

Optimization of linear and higher order optics [24] is essential for preserving beam quality, effective bunch compression and reducing particle loss. Without any errors the coordinates of the central orbit for an off-momentum particle in an achromat $\eta = \eta' = 0$ are given by

$$c\Delta t_1 \quad = \quad R_{56}\delta_0 + T_{566}\delta_0^2 + U_{5666}\delta_0^3 + ... \tag{3.3}$$

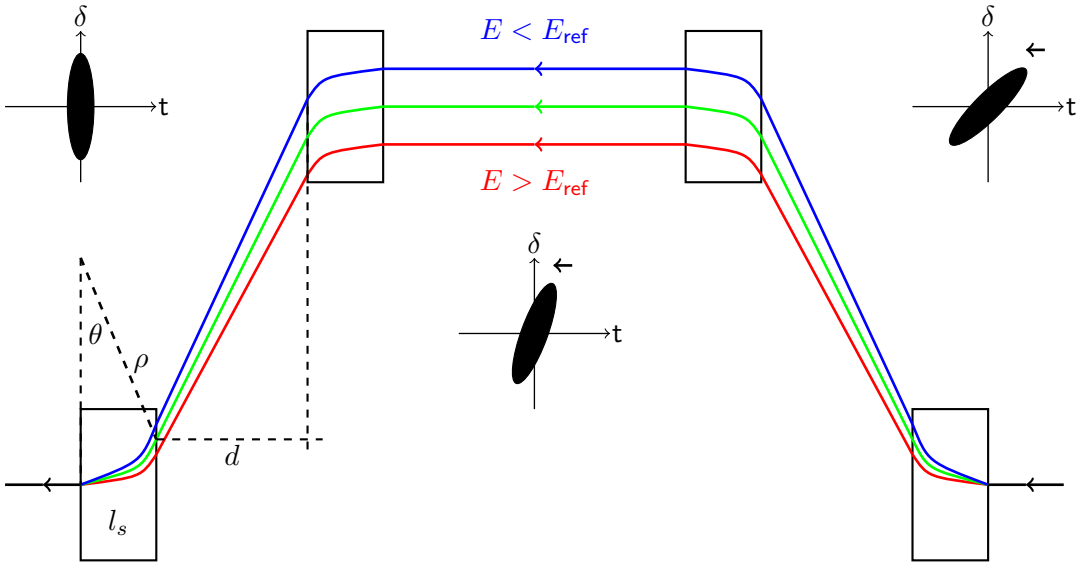

Figure 3.2: Linear bunch compression in the ALICE chicane.

Sextupoles and octupoles can be explicitly used to control the 2nd (T) and 3rd (U) order terms respectively. This thesis concentrates on the first two orders of manipulation. R_{56} acts so that each particle experiences a linear translation in the horizontal $c\Delta t$ plane causing a tilt of the longitudinal phase space ellipse as shown in Fig. 3.2. Whereas the T_{566} value imprints non-linear components on the phase space as it manipulates the 2nd order energy term δ_0^2. The value of R_{56} depends on the magnet type chosen for a given chicane. For the ALICE chicane one could have one of the following scenarios given in Table 3.2. θ is the bending angle and θ_1 and θ_2 are the entrance and exit angles of the first dipole respectively.

The difference in R_{56} in Table 3.2 is not negligible. The following analytic calculations [25] help one understand these discrepancies. Fig. 3.2 shows the chicane using Type A parallel rectangular (RECT) magnets. Using the symmetry relations one can express R_{56} in terms of its independent derivatives

$$R_{56} = \frac{c\Delta t}{\delta} = cp\frac{\Delta t}{\Delta p} = p\,\frac{\mathrm{d}s}{\mathrm{d}p} \quad \rightarrow \quad R_{56} = p\,\frac{\mathrm{d}s}{\mathrm{d}\theta}\,\frac{\mathrm{d}\theta}{\mathrm{d}\rho}\,\frac{\mathrm{d}\rho}{\mathrm{d}p} \tag{3.4}$$

In the following, each derivative is found separately, then substituted into back into Eq. (3.4). The magnet arc length $l_{\mathrm{arc}} = \rho\,\theta$ and drift length $d/\cos\theta$ shown in Fig. 3.2 depict a positive increment in the total path length $(\mathrm{d}l > 0)$. The beam trajectory through the full chicane l is the summation of the longitudinal displacement in the four magnets $l_s = \rho\sin\theta$ and the two drifts. The length of

Table 3.2: R_{56} chicane value depending on magnetic type.

Type	Name	$\theta(^\circ)$	θ_1	θ_2	R_{56} (m)
A	RECT	21.5	0	θ	-0.29792
B	RECT	21.5	$\theta/2$	$\theta/2$	-0.27829
C	SECT	21.5	0	0	-0.35205

the middle drift is irrelevant.

$$\begin{aligned} l &= 4l_s\Big(\frac{\theta}{\sin\theta}\Big) + 2d\Big(\frac{1}{\cos\theta}\Big) \\ \frac{\mathrm{d}s}{\mathrm{d}\theta} &= \frac{\mathrm{d}l}{\mathrm{d}\theta} \\ \frac{\mathrm{d}s}{\mathrm{d}\theta} &= 4l_s\Big(\frac{\sin\theta - \theta\cos\theta}{\sin^2\theta}\Big) + 2d\Big(\frac{\sin\theta}{\cos^2\theta}\Big) \end{aligned} \tag{3.5}$$

In a similar manner one can find the second derivate, the radial angle dependence as

$$\frac{\mathrm{d}l_s}{d\rho}\Big/\frac{\mathrm{d}l_s}{\mathrm{d}\theta} = \frac{\mathrm{d}\theta}{\mathrm{d}\rho} = \frac{\tan\theta}{\rho} \tag{3.6}$$

By definition, the deflection of an electron through a dipole field B is given by

$$\frac{1}{\rho} = e\frac{B}{p} \tag{3.7}$$

which leads one to the final differential

$$\frac{\mathrm{d}\rho}{\mathrm{d}p} = \frac{\rho}{p} \tag{3.8}$$

Substituting Eq. (3.5), Eq. (3.6) and Eq. (3.8) into Eq. (3.4) the analytical expression for the longitudinal energy dependent R_{56} term for the type A magnets becomes

$$R_{56}(\theta) = 4\rho\,(\theta - \tan\theta) - 2d\,\frac{\tan^2\theta}{\cos\theta} \tag{3.9}$$

Due to the initial definition of the dipole matrix in Eq. (3.1) where $R_{16} = -R_{52}$ a physical polarity exists such that $\mathrm{d}s/\mathrm{d}\theta = -\mathrm{d}l/\mathrm{d}\theta$. Using the optic parameters of the ALICE chicane an accurate comparison with Table 3.2 is found for the type A magnets

$$R_{56}(21.5\,^\circ) = -0.29792\,\mathrm{m}$$

The dispersion created in a single magnet is independent of the magnet type. However, magnet types B and C can not be as readily derived for a full chicane using the previous assumptions since the angular dispersion R_{26} depends on the exit angle θ_2. Multiplying Eq.(3.1) with the relevant edge matrices $R_{\mathrm{EDGE},\theta_2} \cdot R_{\mathrm{SECT},\theta} \cdot R_{\mathrm{EDGE},\theta_1}$ one finds

$$\eta' = R_{26} = \sin\theta + (1 - \cos\theta)\tan\theta_2 \tag{3.10}$$

The angular dispersion as given in Table 3.3 differs for example between type A and B differs by 20 % (a factor $1 - \tan^2\theta/2$) and propagates along the drift space $\eta_2 = \eta_1 + \eta_1' d/\cos\theta$ to produce different values for the dispersion on entering the second magnet. The dispersion dependence of R_{56} in a dipole can be derived from Eq. (3.4) for a given particle velocity β as follows:

$$R_{56} = \frac{c\Delta t}{\delta} = cp\frac{\Delta t}{\Delta p} = p\frac{\partial}{\partial p}\frac{l}{\beta}$$

Table 3.3: Dispersion derivative at the dipole exit.

Magnet type	A		B		C
Angular dispersion	$\tan\theta$	$\geq$	$2\tan\theta/2$	$\geq$	$\sin\theta$

this leads to

$$R_{56} = \frac{p}{\beta}\frac{\partial \Delta l}{\partial p} - \frac{lp}{\beta^2}\frac{\partial \beta}{\partial p} \tag{3.11}$$

The first term on the RHS of Eq. (3.11) is commonly described as the momentum compaction factor which is the variation of path length with momentum

$$\frac{\Delta l}{\Delta p/p} = \int \frac{\eta}{\rho}\,\mathrm{d}s \tag{3.12}$$

while the second term describes explicitly the curved trajectory in the dipole for a given momentum. Through differentiating $p = \beta\gamma m_0 c$ one finds

$$\frac{\partial p}{\partial \beta} = \gamma^3 m_0 c \tag{3.13}$$

Substituting the derivatives and canceling like terms, Eq. (3.11) becomes

$$\begin{aligned} R_{56} &= \frac{p}{\beta}\int \frac{\eta}{\rho}\frac{\mathrm{d}s}{p} - \int \frac{\mathrm{d}s}{\beta^2}\frac{p}{\gamma^3 m_0 c} \\ R_{56} &= \frac{1}{\beta}\int \left(\frac{\eta}{\rho} - \frac{1}{\gamma^2}\right)\mathrm{d}s \end{aligned} \tag{3.14}$$

As previously stated, the dispersion on entry to the second dipole is different for all magnet types due to the angular dispersion propagation in the drift space. The integral of the resulting dispersion will vary and hence produce the different R_{56} values given in Table 3.2.

Fig. 3.3 shows pictorially the variation of the longitudinal dispersion through the chicane. Since the total bend angle of the chicane is zero and there are no quadrupoles to manipulate the dispersion, the desired R_{56} value at the exit of the chicane also occurs in the third dipole. The bunch is initially over compressed and then in the fourth dipole compressed a second time. Therefore the shortest bunch length and hence the largest CSR contribution occurs twice in the chicane. The temporal transition in the third dipole is commonly referred to as a CSR burst and is often used in combination with ring based light sources using low-alpha optic [26]. The radiation generated in the third dipole is not used as the THz source at ALICE (though it is out coupled using a diamond window downstream of the fourth dipole [27]) it is solely an unavoidable source of beam degradation.

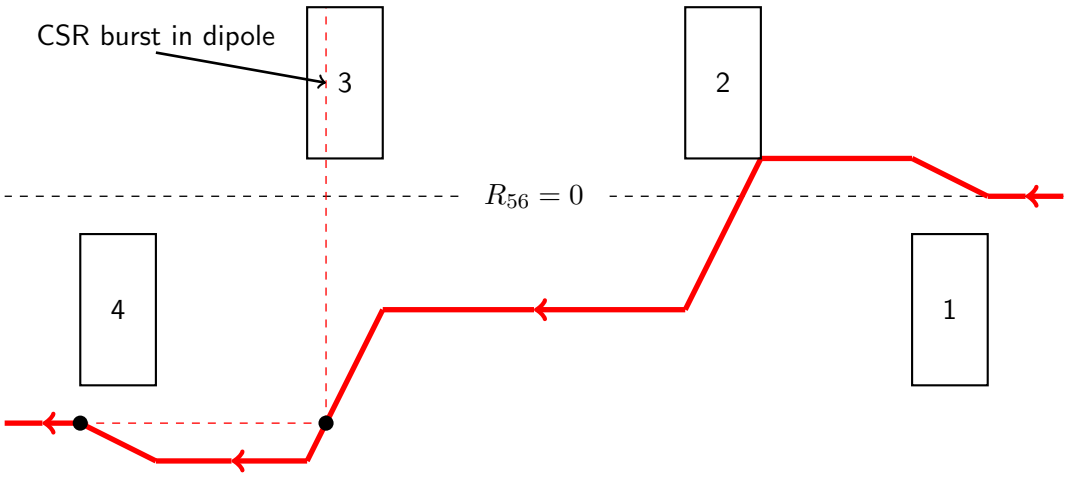

Figure 3.3: Longitudinal dispersion in the ALICE chicane.

Using Eq. (3.2) and setting the ALICE achromat chicane with $\eta = \eta' = 0$ on entry and exit, a 2 ps bunch would require $c\Delta t_1 = 0$ a correlated energy spread of $\Delta p/p \simeq 2 \cdot 10^{-3}$ for full compression. Through measurements, the following section addresses the longitudinal beam parameters of the ALICE machine, to portray the present expectations of high charge ERL injectors.

3.2 Measurement of Injector Bunch Length

A dedicated commissioning phase to characterize the longitudinal beam dynamics was undertaken in early 2012. The exploitation proposal was scheduled to cover injector, bunch sub-structures and post linac dynamics but due to unforeseen problems with the SRF linac, the availability of the machine was restricted to injector studies. The longitudinal transport of the beam in the low energy section is dictated by space charge and velocity bunching effects [28]. These dominant processes determine the phase space of the beam at the linac entrance and hence ultimately throughout the machine [29].

The injector comprises of a high voltage direct current photocathode gun, whereby laser light is used to release electrons from an arsenide cathode. This normal conducting setup for an injector is commonly used throughout the world at ERL test facilities due to its ability to produce reliable high charge (60 pC) electron bunches. The 81.25 MHz mode locked drive laser and optical system defines the bunch structure emitted from the cathode. A Pockels cell can be used to produce a longitudinally 'flat-top' macrobunch. The following investigations used a 900 ns long train of single bunches at a repetition of 20 Hz. The measurements are averaged over the train.

A scintillation screen positioned at a dispersive location, in the foreground of Fig. 3.4, was used to find the bunch length and energy spread of the beam using data from the beam image. Measuring the longitudinal parameters of a bunch using the zero-crossing method is a standard procedure at ALICE and the notable machine components are all integrated to aid this quick experimental technique. First, the bending magnets are degaussed then the buncher phase is scanned to find the relative zero-crossing phase of the second booster cavity. Here only the first booster cavity is used for acceleration, the second cavity gradient is slowly varied at a given phase relative to the buncher

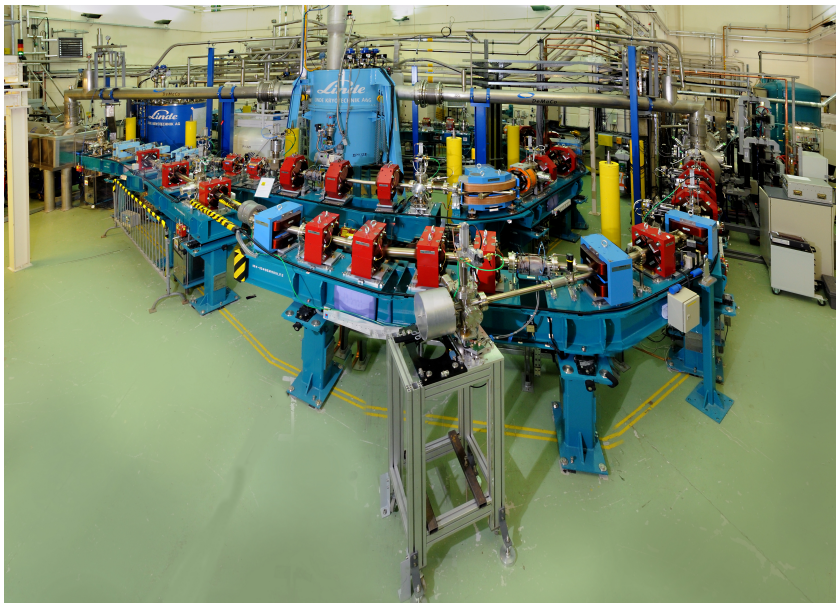

Figure 3.4: Photo of the magnetic lattice of the injection line at ALICE [30].

phase and the change in the horizontal beam centroid at the screen is recorded. The measurement is then iterative until a phase is found when the centroid position is independent of the gradient in the second booster cavity. Hence the phase setting for zero-crossing. The image on the screen is assumed to be dispersion dominated therefore

$$\begin{aligned} \sigma_x^2 &= \epsilon_x \beta_x + \eta_x^2 \sigma_E^2 \\ \sigma_x &\simeq \eta_x \sigma_E \end{aligned} \tag{3.15}$$

The uncorrelated energy spread was then directly measured from the beam size on the screen using Eq. (3.15) as 5 keV at 6.5 MeV then $\sigma_E \sim 1 \cdot 10^{-3}$. The gradient in the second booster cavity was then varied and again the image on the screen was recorded. Fig. 3.5 shows three such images, which needed to be post-processed in order to find the horizontal beam size.

Presently such post-processing image analysis is not integrated into the machines software, so a program was written to convert the pixel data of an arbitrary saved image. Here the image file is converted to a raw data file, it is then read and converted in to an array. The background is numerically removed, the color code is converted to greyscale for simplicity and the array is then subjected to data analysis. The region of highest intensity in both planes is deduced, the beam sizes are calculated and the data is binned in order to produce histograms as shown in Fig. 3.6. The vertical profile is shown for completeness.

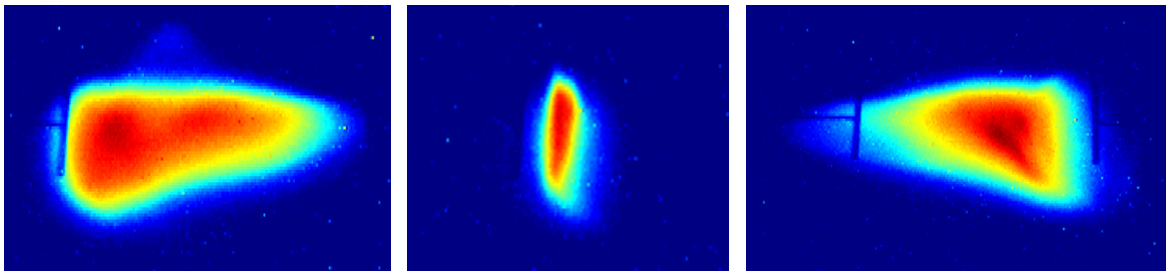

(a) 0.20 MV (b) 0.77 MV (c) 1.48 MV

Figure 3.5: Varying the beam size using the voltage settings of the 2nd booster cavity.

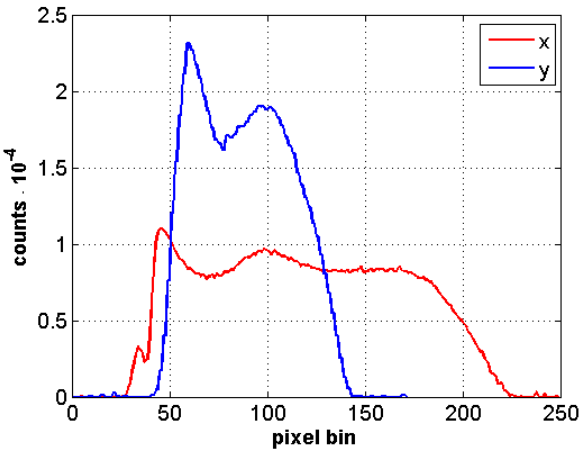

Parameter	Value	Unit
Voltage	0.20	MV
σ_x	2.442	mm
σ_y	1.1755	mm
Charge	55	pC
Nom. Energy	6.5	MeV
Laser Pulse	900	ns
Camera	INJ-5	
Pixel Size	0.05	mm
Dispersion	1.1	m

Figure 3.6: Image analysis of Fig. 3.5a example and data table.

The energy considerations at zero-crossing and the measured beam size in the horizontal plane σ_x can be used to approximate the bunch length as follows

$$\begin{aligned} E_1 &= E_0 + V\sin(\phi) \\ \Delta E &= V\cos(\phi)\Delta\phi \end{aligned}$$

at zero-crossing $\phi = 0$ then $\cos(\phi) = 1$ and therefore

$$\Delta E = V\Delta\phi \tag{3.16}$$

Substituting in Eq. (3.15) one finds

$$\frac{\sigma_x E_0}{\eta_x} = \Delta\phi\, V \tag{3.17}$$

σ_x is measured for a given booster cavity gradient V and both the nominal beam energy E_0 and η_x are taken from the data table in Fig. 3.6. The relative phase change $\Delta\phi = 2\pi f\sigma_t$ can be deduced from the gradient of the fitted data shown in Fig. 3.7 to find the bunch length σ_t.

The error analysis assumes that the largest error occurs in the measurement of beam size due to the pixel size limitation and a least squares fit is used. Shaded in green is the boundary of the uncorrelated energy spread found from Eq. (3.15). The tendency shown in Fig. 3.7 is not truly linear since the dispersion no longer dominates the geometrical beam properties at small beam sizes. The experimental data is sufficient to approximate the bunch length at the booster exit using Eq. (3.16) as $\sigma_t = (2 \pm 0.9)$ ps. Given the non Gaussian beam form on some images one may prefer to quote the full width half maximum bunch length as approximately 5 ps. The assumption that one would require a correlated energy spread of $\Delta p/p \sim 2 \cdot 10^{-3}$ for full compression in the post linac section seems reasonable given these measurements.

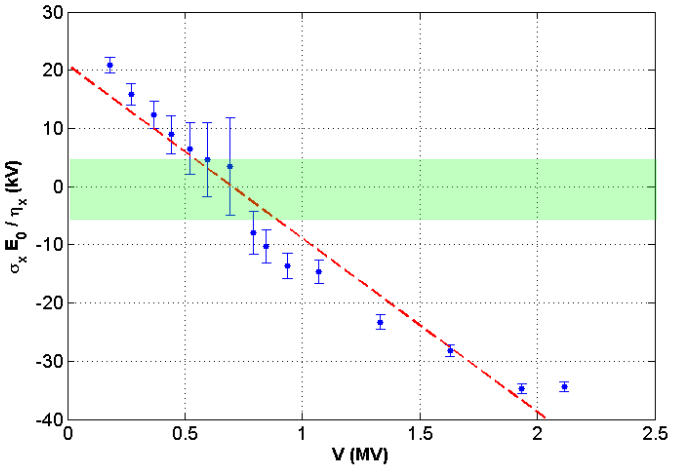

Figure 3.7: Linear fit of the measured data using Eq. (3.16) to deduce the bunch length.

The experiments at ALICE have provided measured values for two; $c\Delta t_0$ and σ_E of the three main linear longitudinal components. The next chapter focuses its attention on the measurement of the longitudinal dispersion and delivers insight into the physics that defines the R_{56} value at low injection energies.

4. The NovoFEL Multi-Turn ERL

The ERL at the Budker Institute of Nuclear Physics in Novosibirsk is one of the most developed machines of its kind in operation today. This rather complicated multi-turn facility comprises of both horizontal and vertical turns.

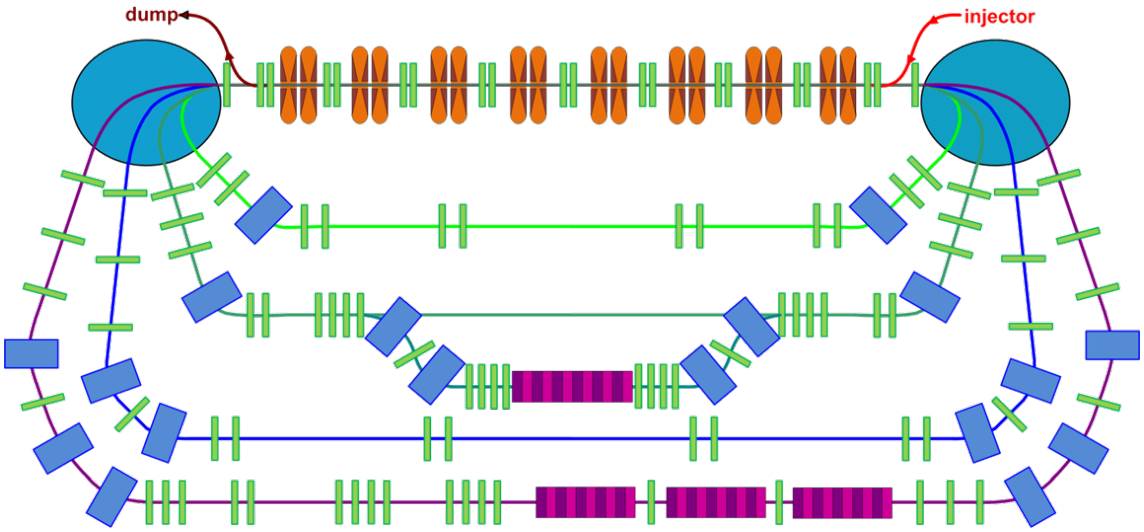

Figure 4.1: Schematic (horizontal plane) of the multi-turn ERL at the NovoFEL facility [31].

The four turn ERL can be treated as three different FELs sharing a common main linac. The RF cavities of the linac are shown in Fig. 4.1 in orange, the quadrupoles and the dipoles in the turns in green and blue respectively. The electron beam energy in the FEL undulators shown in purple, can be 12, 22 or 42 MeV depending on the number of turns. The longitudinal dynamics are such that the bunch length is approximately 100 ps in the first turn and then compressed by a magnitude in the high energy turns. All the cavities use low frequency normal conducting technology allowing large transversal and longitudinal acceptance so longer electron bunches with large emittances can be tolerated relaxing the demands on the injector. The magnetic structure is symmetric wherever possible and operational experience of the FELs led to the installation of additional sextupole coils into some quadrupoles to correct the 2^{nd} order aberrations which has reduced the overall beam loss during lasing.

The vertical plane commissioned in 2006 shown overleaf in Fig. 4.2, provides electrons for a dedicated THz FEL. Here two electromagnetic undulators of 12 cm period and the phase shifter are part of an optical cavity which out couples tunable coherent radiation in the wavelength range of 120 - 240 μm. The average output power is 500 W which corresponds to over 1 MW peak power, with a measured linewidth close to the Fourier limit [32].

First lasing of the horizontal plane FEL was achieved in 2009. Installed on a bypass at 22 MeV, as shown in Fig. 4.1, the second electromagnetic 12 cm period undulator is an upgrade of the first with

smaller aperture and higher magnetic field amplitude. The pole shapes are as in the vertical turn manufactured to provide equal electron beam focusing in both planes.

Commissioning of the third FEL in the fourth turn is still ongoing. This FEL will operate at 42 MeV using three permanent magnetic undulators with a 6 cm period. The preliminary lattice adjustments have shown 95 % of the beam current returns safely to the dump. This allowed operation of an average current of 5 mA to be maintained to initially demonstrate lasing.

With a maximum average current of 30 mA, 1 MW THz radiation and the near possibility of four turn acceleration the light source competes well on a world stage. The next critical stage in commissioning will focus its attention on the optimization of the longitudinal acceptance, as investigated in Chapter 4.2, in order to recuperate a beam of large energy spread. The operating phase ϕ of the horizontal n-turn ERL is determined by the final arc since its path length is not equal to standard ERL case but instead decelerates the bunch on the 'other side' of the the RF cycle $L_4 = \lambda_{rf}(n + 1/2 - \Delta\phi/\pi)$. This optic is designed to remove the energy spread created during the acceleration and the lasing processes. A similar concept is investigated in Chapter 6.4.5 for the FSF light source.

4.1 Longitudinal Dispersion Measurements

The beam diagnostics at the NovoFEL are extensive. Over 200 Beam Position Monitors (BPM) are situated around the many turns. These BPMs with the additional help of temperature sensors and radiation monitors work together to ensure a safe and correct passage through the multi-turn accelerator. The measurements undertaken for this thesis concentrate on the first turn of the NovoFEL.

Shown in Fig. 4.2 are the main accelerating structures of the first turn that bends in the vertical plane. The electron beam from the gun is injected into a buncher and then onwards through the chicane merger and into the main accelerating structure. On exit the beam traverses the magnetic optic through the FEL undulator and back to the linac for deceleration.

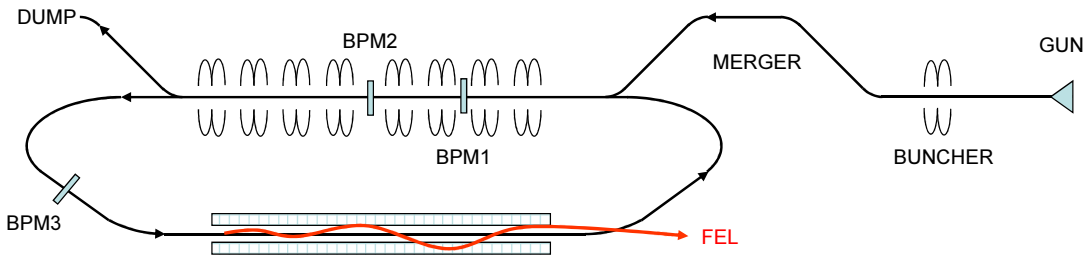

Figure 4.2: Schematic of the vertical turn of the NovoFEL.

Table 4.1: Parameters of the vertical turn.

Injection Energy (MeV)	2
Main Linac (MeV)	10
Charge per bunch (nC)	1.5
Norm. Emittance (mm mrad)	30
RF (MHz)	180.4
Rep. Rate (MHz)	22.5

4.1.1 R_{56} in the Vertical Arc

Two R_{56} measurements using the multiple BPM signals were undertaken in order to test the validity of the BPM analysis software recently installed at the NovoFEL facility. The hardware should not only be fast enough to separately detect both accelerated and decelerated beams but also calculate the variations in orbit length using the correlation function of two signals

$$G(\tau) = \int S_1(t) S_2(t+\tau) \mathrm{d}t \tag{4.1}$$

BPM2 located between the linac cavities in Fig. 4.2 was used to find R_{56} in the vertical turn. S_1 is the outgoing signal on acceleration and S_2 is the returning signal after traversing the full vertical turn. The two signals are separated in time by τ.

Two 'microtrons' (historically known as) are used to provide power to the main linac. The energy of each microtron given in Table 4.2 was found using the vertical beam displacement Δy at BPM3.

$$\Delta y \simeq \eta_y \frac{\Delta E}{E} \tag{4.2}$$

At BPM3 the vertical dispersion due to the first vertical bending magnet is $\eta_y \sim 0.5\,\mathrm{m}$ and the vertical displacement was measured as $\Delta y \sim 10\,\mathrm{mm}$ this corresponds to an energy deviation of $\Delta E/E \sim 2\,\%$. As in the case of the previous measurements at ALICE, the contribution from the geometrical emittance was again neglected. The measurement parameters and the resulting value of R_{56} in the vertical turn are given in Table 4.2. The full RF power for the 180 MHz linac is divided between two waveguide transport lines mic_1 and mic_2. Varying only the higher energy side mic_2 of the linac resulted in less beam loss compared to varying both simultaneously.

Table 4.2: R_{56} measurement in the vertical turn.

mic_1 (kV)	mic_2 (kV)	Orbit var. G (°)	t (ns)	$\Delta E/E$ (%)	R_{56} (cm)
6750	6000	216.30	3.33	1.77	141
6750	5750	221.47	3.41		

Simulations [33] of the complete turn comprising of two symmetric arcs suggest that this measurement of R_{56} is reasonable. For the standard FEL optic they show a longitudinal dispersion of $R_{56} = 160\,\mathrm{cm}$ and given the optic is in reality asymmetric the value in Table 4.2 is plausible.

4.1.2 R_{56} in the Merger

As mentioned in the previous section the standard operating mode is optimized for FEL lasing. This single goal has led to an optic that is neither achromatic nor isochronous rather to one whereby the quadrupole settings are adjusted to suit lasing. In theory, one would suggest closed dispersions, low betatron functions and the shortest bunch possible should produce the best lasing. The reality is that there are not always enough quadrupoles for matching, the injection energy is too low so that space charge dominates which results in large betatron functions. Upgrades are foreseen, for example the injector gun power supply will be replaced with one capable of producing a higher accelerating voltage to reduce this space charge focusing effect. The following measurements were undertaken at

a low bunch charge in order to limit the non-linear space charge contribution to bunch lengthening in the injector.

In order to experimentally determine an achromatic optic in the injector merger, an EPICs based optimizer was used to find the difference in beam position measurements of BPM1 and BPM2 shown in Fig. 4.2. Then the Pythagoras square of these two signals was minimized as the merger quadrupole settings were scanned. This procedure is relatively quick and was repeated for energy deviations up to $5\,\%$ until an optimal achromat was found and the exiting beam passed safely through the machine to the dump.

With the achromat set, the energy was varied by $1\,\%$ and the change in path length was deduced for the merger from the two signals again by way of the correlation function at BPM2. The resolution of the BPM analysis is at best $10\,$ps giving the measurement at least a $10\,\%$ error. The longitudinal dispersion was found to be $R_{56,\text{expt}} = (245 \pm 30)\,$cm

According to analytical tracking simulations using actual quadrupole settings for an achromatic merger optic $R_{56,\text{optic}} = 80\,$cm. This value is considerably less than experimentally found. However the simulation did not take into account the velocity spreading at low energies. To calculate its impact on the measurement one should take a closer look at this additional energy term associated with a drift space.

Since the merger is also a chicane of four bending magnets, albeit with additional quadrupoles, the results of the derivations in Chapter 3.1 can be used as a starting point. The studies of the longitudinal dispersion in the ALICE chicane led to Eq. (3.14) of which the momentum dependent term was given by

$$R_{56} = -\frac{1}{\beta}\int \frac{1}{\gamma^2}\,\mathrm{d}s \xrightarrow{\Delta p/p} \frac{L}{\beta\gamma^2} \tag{4.3}$$

In practice, the absolute total energy is varied and the time difference between two signals is measured. For completeness the change in path length Eq. (4.3) should to be expressed as a function of energy.

$$\frac{\Delta p}{p} = \frac{\Delta(\beta\gamma)}{\beta\gamma} = \frac{1}{\sqrt{\gamma^2-1}}\cdot\frac{2\gamma\Delta\gamma}{2\sqrt{\gamma^2-1}} = \frac{\gamma\Delta\gamma}{\gamma^2-1} = \frac{\Delta\gamma}{\gamma}\frac{1}{\beta^2} \tag{4.4}$$

Using this relation the path length variation in terms of the energy $E = \gamma mc^2$, rather than the momentum p becomes

$$\begin{aligned} c\Delta t &= R_{56}\delta && (4.5)\\ &= \frac{L}{\beta\gamma^2}\frac{\Delta p}{p} && (4.6)\\ &= \frac{L}{\beta\gamma^2}\frac{\Delta\gamma}{\gamma}\frac{1}{\beta^2} && (4.7)\\ c\Delta t &= \frac{L}{\beta^2\gamma^2}\frac{\Delta E}{pc} && (4.8) \end{aligned}$$

and hence the final expression for the longitudinal dispersion using the canonical variables contains an extra $1/\beta$ term compared with Eq. (4.3)

$$R_{56,\text{vel}} = \frac{L}{\beta^2\gamma^2} \tag{4.9}$$

Table 4.3: R_{56} (cm) in the injector merger.

$R_{56_{\text{optic}}}$		$R_{56_{\text{vel}}}$		$R_{56_{\text{theory}}}$	$R_{56_{\text{expt}}}$
80	+	135	=	215	245 ± 30

The kinetic energy of the standard injector beam is 1.27 MeV therefore over an injection length of almost 15 m the velocity term $R_{56,\text{vel}} = 135$ cm is substantial. Table 4.3 shows that the total theoretical longitudinal dispersion lies within the measured value given the experimental error associated with the BPM resolution of 10 ps.

4.2 Optimization of Transversal Acceptance in the Linac

Lattice optimization is continually ongoing as the multi-turn ERL in Novosibirsk evolves. The relatively high emittance from the injector and additional energy spread from lasing require a high acceptance optic. The same beam lines are used for both acceleration and deceleration which complicates the adjustment of the magnetic system. Since all turns share a common main linac Fig. 4.3, it is paid particular attention to in this section. Nine quadrupole pairs are symmetrically distributed between the eight accelerating cavities to provide additional transversal focusing.

As previously described, the injector defines the Twiss-parameters to which the returning beam needs to be matched. The injector line lacks the magnetic optic for full matching and is heavily dominated by space charge effects.

The critical pass to optimize is the final deceleration 12 MeV $\rightarrow$ 2 MeV since there are ample quadrupoles in this recovery arc for matching the betatron functions to the linac beamline and the beam energy is at its lowest. Higher energy beams in the other remaining turns are less affected by transversal focusing in the linac. This study intends to minimize both the initial betatron functions β_{twiss} and the beam size σ_i throughout the linac using the nine quadrupole doublets. As highlighted in the previous section the low energy terms γ_i and β_i play a crucial role. By definition, the normalized beam emittance ε_{n} on deceleration remains constant.

Due to the physical configuration of the actual quadrupole power supplies, the quadrupole settings are constraint to mirror symmetry about the centre of the linac section and each quadrupole doublet acts as an equal but opposite pair, as shown in Fig. 4.3.

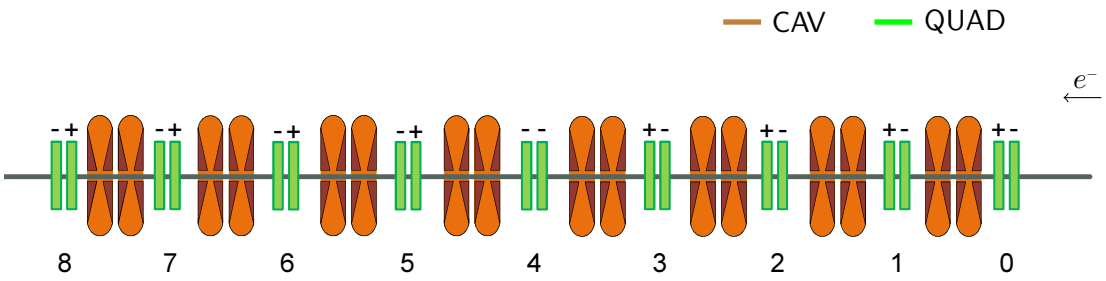

Figure 4.3: Schematic of the NovoFEL linac.

Table 4.4: Twiss-parameters at the entrance to linac beamline, $s = 0\,\text{m}$ in Fig. 4.4b.

β_x (m)	α_x	β_y (m)	α_y
10.02	2.07	8.54	1.43

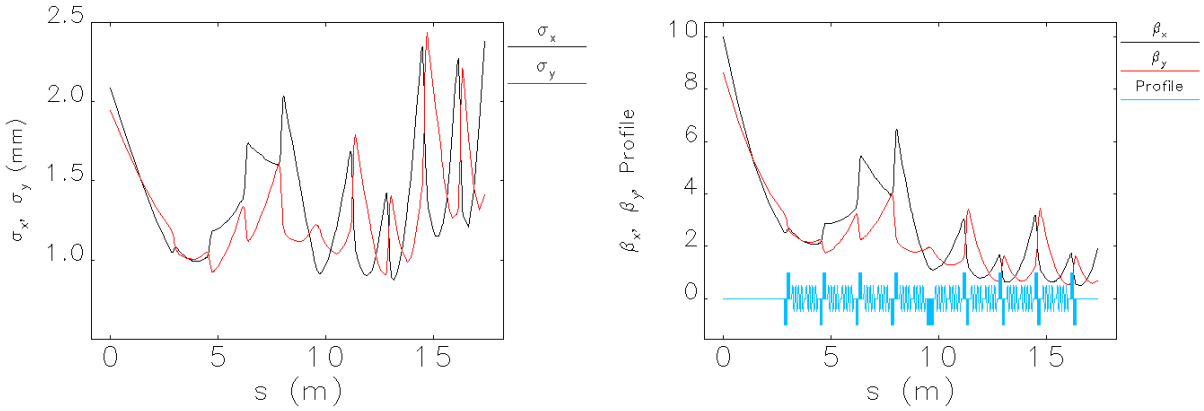

(a) Transversal beam size.

(b) Betatron functions.

Figure 4.4: Optimized beam parameters for largest transversal acceptance along the linac.

A total of 20 marker points, one at each cavity entrance and exit and at the far extremities of the beamline, were implemented into the tracking code Elegant [34] for optimization.

$$\sum_i \sigma_i^2 = \sum_{i=1} \frac{\varepsilon_\text{n}\,\beta_\text{twiss}}{\beta_i\,\gamma_i} \tag{4.10}$$

Eq. (4.10) was minimized at each marker point to produce the largest acceptance throughout the linac. This results in minimum $\sum \sigma_{x,y}^2$ as shown in Fig. 4.4a. Previous analytical attempts have been found to be cumbersome since in practice the energy varies due to machine development and a full start-to-end optic for the four turns with readily adjustable settings is seen as an essential tool. This short code has been successfully integrated into such a full simulation file. The optimization procedure takes just several minutes and delivers values for the betatron functions at the entrance and exit of the linac as shown in Fig. 4.4b. Quadrupole pair 0 shown in Fig. 4.3 can be seen in Fig. 4.4b at s = 3 m as the first symbol of the blue profile plot.

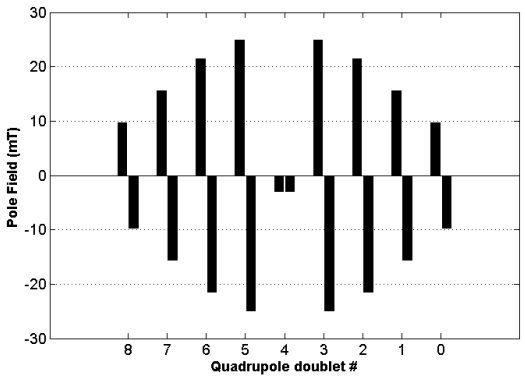

Figure 4.5: Magnetic field strength of the quadrupoles along the linac.

The initial Twiss-parameters given in Table 4.4 describe a reasonable size beam envelope to which the injector and final arc on deceleration can be matched to. More importantly the theoretical optimized quadrupole settings can be used as a starting point in the commissioning phase. Fig. 4.5 shows that a maximum magnetic field on the pole of 25 mT is required when using the optimized settings devised in this section.

This and the previous chapter have presented experimental insight into the longitudinal beam properties associated with ERL facilities. The longitudinal transport of the beam is dominated by low energy effects that in turn depict the beam dynamics throughout the machine. The next chapter continues on with this theme, introducing the suppression of beam degradation due to radiation effects. The techniques proposed are all suitable for the compact arcs used in the present ERL test facilities worldwide.

5. Transverse Emittance Degradation Reduction

This chapter investigates the techniques that can be implemented into the optic to suppress the transverse emittance growth due to radiation effects. Adopting the theory introduced in Chapter 2, CSR imposes an energy modulation on the beam. The tail interacts with the head causing a wake to be imprinted on the longitudinal bunch coordinates. The CSR wake not only limits the fundamental bunch length but causes transversal emittance degradation. Energy loss in a dispersive section due to CSR leads to a transversal displacement after the bend section which in turn increases the transverse emittance. The degradation can in certain circumstances be described analytically.

In the following sections the idea of using the phase advance of the betatron motion to nullify the impact of CSR-induced emittance growth is addressed. The theory is then developed for a simple generic compact arc that contains longitudinal dispersion for bunch compression. The relevant issues regarding 2$^{\text{nd}}$ order chromatic aberrations and their correction are derived from first principles to help produce an optic for a compact ERL.

5.1 Cell-to-Cell Phase Advance Manipulation

In the 1D CSR model [35], the wakes depend only on the longitudinal bunch profile and the geometrical properties of the bending system. The wakes do not depend on the transversal bunch parameters. In this regime all the particles in a slice experience the same shift in the bending plane coordinate δx and angle $\delta x'$.

For two consecutive identical isochronous bends, the longitudinal bunch shape does not change and the bunch dynamics are identical if the additional relative energy spread δ_{CSR} due to CSR produced in the first bend is small enough $\delta_{CSR} R_{56} \ll \sigma_z$. In the first bend, particles experience shifts δx and $\delta x'$ due to CSR. In the second bend, these deviations undergo betatron oscillations and exactly the same shifts δx and $\delta x'$ are simply added to them once more. Fig. 5.1 shows pictorially the 1D CSR evolution of the wake in the $(x, c\Delta t)$ plane for two identical isochronous bending cells.

The horizontal phase advance from A to C is π. The CSR wake created in the blue dipoles of the bending cell from A to B is manipulated using the green quadrupoles between B and C. The resulting phase space is mirrored about the $c\Delta t$ axis. The CSR action in the following cell from C to D is identical to the first cell and the total CSR wake is then a cancellation. Fig. 5.1 is pictorially accurate when $\Delta\mu_{\mathsf{A}\to\mathsf{B}} \ll \Delta\mu_{\mathsf{B}\to\mathsf{C}}$. The wakes in the consecutive bending cells are given by

$$\begin{aligned} \begin{pmatrix} \delta x \\ \delta x' \end{pmatrix}_2 &= \begin{pmatrix} \delta x \\ \delta x' \end{pmatrix}_0 + R_x \begin{pmatrix} \delta x \\ \delta x' \end{pmatrix}_0 \\ &= \Big(I(1+\cos\mu_x) + J\sin\mu_x \Big) \begin{pmatrix} \delta x \\ \delta x' \end{pmatrix}_0 \end{aligned} \tag{5.1}$$

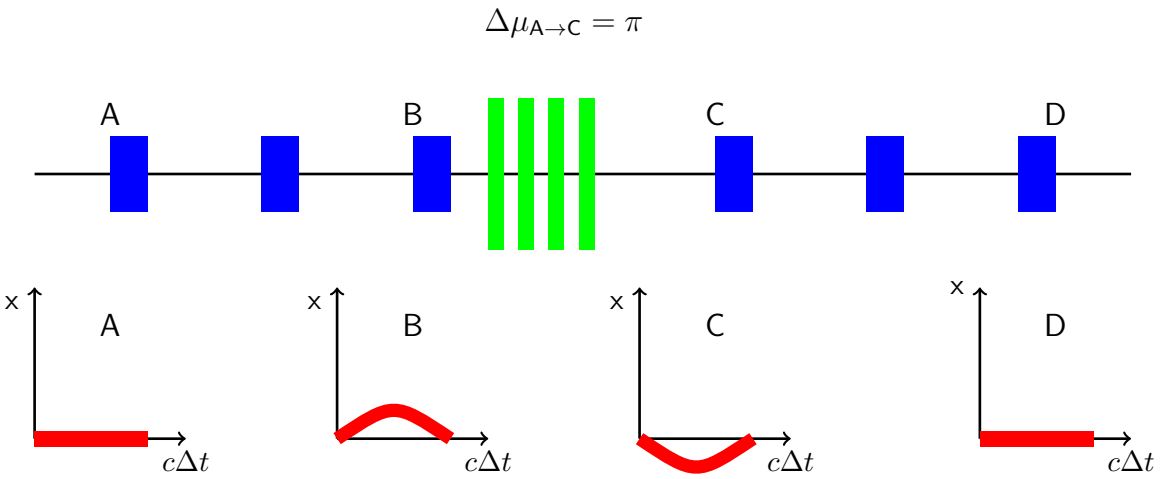

Figure 5.1: Cell-to-cell CSR wake in red for two identical isochronous bending cells, blue are dipoles and green are quadrupoles.

where $I = \begin{pmatrix} 1 & 0 \\ 0 & 1 \end{pmatrix}$ and $J = \begin{pmatrix} \alpha & \beta \\ -\gamma & -\alpha \end{pmatrix}$

If the betatron phase advance is $\mu_x = \pi$ as shown in Fig. 5.1, the impact of CSR on the transversal emittance is null [36]. The same effect can be achieved for a system of N identical isochronous cells. The CSR shift is then given by

$$\begin{aligned} \begin{pmatrix} \delta x \\ \delta x' \end{pmatrix}_N &= \sum_{n=0}^{N} R_x^n \begin{pmatrix} \delta x \\ \delta x' \end{pmatrix}_0 \\ &= \left(I \sum_{n=0}^{N} \cos n\mu_x + J \sum_{n=0}^{N} \sin n\mu_x \right) \begin{pmatrix} \delta x \\ \delta x' \end{pmatrix}_0 \end{aligned} \tag{5.2}$$

If $\mu_x = 2\pi \cdot k/N$, where k is an integer, the impact of CSR on the transversal emittance is again nullified.

An analytical method proposed by Hajima [37] describes a CSR wake dispersion function (ζ, ζ') in a bending plane as the displacement of bunch slices in phase space. Fig. 5.2 shows the principle for three identical cells each with a phase advance of $\Delta\mu_x(i) = (n/3)\,\pi$. Again using this notation, after the cells the three CSR kicks will cancel out.

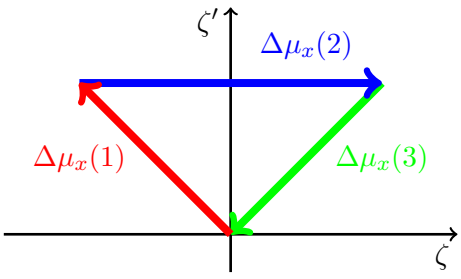

Figure 5.2: Cell-to-cell kick manipulation using the CSR wake dispersion function notation.

This linear analysis of the CSR effect on transversal beam dynamics assumes that all of the dipoles have the same bending radius, the longitudinal bunch profile remains unchanged and transient CSR effects are neglected. These later two assumptions simplify the theory developed in Chapter 2.3. Not only is the energy loss due to CSR constant but the variations due to the passage on entry, through and on exiting the magnet are neglected. Now the charge and bunch length are independent of the energy loss for a single electron. Eq. (2.23) in a bending cell of length l then simplifies to

$$\Delta E_{\mathsf{CSR}} \quad \propto \quad \frac{l}{\rho^{2/3}} \propto \rho^{1/3}\theta = \kappa\rho^{1/3}\theta \tag{5.3}$$

The CSR kick is linearized using a geometric wake function κ of units (m^{-1}). It is defined so that the coordinate deviations of the particle relative to the ideal path after passage through the bending cell are given by

$$\Delta x = \begin{pmatrix} \eta \\ \eta' \end{pmatrix} \delta + \begin{pmatrix} \zeta \\ \zeta' \end{pmatrix} \kappa \tag{5.4}$$

This chapter continues on with this notion, to validate this CSR wake theory for a isochronous TBA bend. Once shown, the chapter uses this theory as a baseline for a simple bend with non-zero longitudinal dispersion. This is contradictory to the above assumptions since the bunch length σ will vary throughout the bend, but is justified as a reasonable starting point for investigations where slight bunch compression occurs. The 5x5 Hajima H-matrices for a sector dipole magnet, where $c = \cos\theta$ and $s = \sin\theta$

$$\begin{pmatrix} \zeta \\ \zeta' \\ 0 \\ \rho\theta \\ 1 \end{pmatrix}_1 = \begin{pmatrix} c & \rho s & \rho(1-c) & \rho(1-c) & \rho^2(\theta - s) \\ -s/\rho & c & s & s & \rho(1-c) \\ 0 & 0 & 1 & 0 & 0 \\ 0 & 0 & 0 & 1 & \rho\theta \\ 0 & 0 & 0 & 0 & 1 \end{pmatrix} \begin{pmatrix} \zeta \\ \zeta' \\ 0 \\ \rho\theta \\ 1 \end{pmatrix}_0 \tag{5.5}$$

and likewise for a drift and quadrupole can be used to transport the CSR wake through a lattice using matrix multiplication in a similar manner to the Twiss-parameters. The form of the H-matrix is predictable in the sense that the top 3x3 section (dashed line) is the standard transport matrix for dispersion in the bending plane and the outer elements describe the CSR wake in terms of the longitudinal dispersion. For instance the H(1,5) element of a dipole is simply the integral of the dispersion.

$$\begin{aligned} \mathsf{H}(1,5) = \int_0^s \eta \, \mathrm{d}s = \int_0^s \rho(1-c) \, \mathrm{d}s &= \int_0^s \rho(1 - \cos(s/\rho)) \, \mathrm{d}s \\ &= \rho[s - \rho\sin(s/\rho)] \\ &= \rho^2(\theta - \sin\theta) \\ &= \rho R_{56} \end{aligned}$$

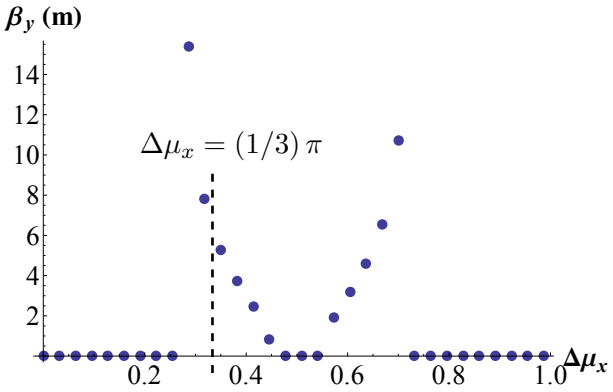

Figure 5.3: Value of the vertical betatron function for a given horizontal phase advance.

An isochronous TBA cell as presented in Chapter 2.2 was used to demonstrate this CSR wake and its impact on the emittance growth. The quadrupole strengths for a periodic solution of the TBA were found analytically as shown in Fig. 5.3, in order to choose a suitable phase advance that coincided with real physical values for the betatron functions in both planes. Points shown where the vertical betatron function is null are non-physical mathematical solutions of the transport matrix. In this example the horizontal plane is always stable. Taking a horizontal phase advance of $\Delta\mu_x(i) = (1/3)\,\pi$ results in a matched vertical betatron function of approximately 6 m.

The necessity of a periodic function is to create stable optic in both transversal planes with a low natural chromaticity so that the impact on the emittance growth due to aberrations is minimized allowing the CSR effect to dominate. Repeating this 60 ° cell three times results in a build up of the CSR wake function, see the blue curve in Fig. 5.4, in the first and second cell and finally as predicted a full correction of it in the third cell. The profile shown in Fig. 5.4 helps reference the positions of the magnets along the optic.

A test bunch with suitable beam properties was tracked without ISR effects through the three consecutive TBA optic to test the suppression of the emittance growth due to CSR and verify the cell-to-cell theory. Fig. 5.5 shows that the emittance has doubled after the first TBA bending cell at $s = 13$ m for both phase advance settings. After the second cell, the emittance varies according to

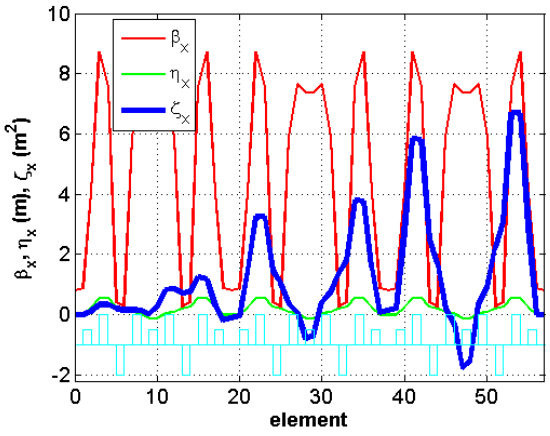

Figure 5.4: CSR wake dispersion function for three consecutive 60 ° TBA cells each of phase advance $\Delta\mu_x(i) = (1/3)\,\pi$.

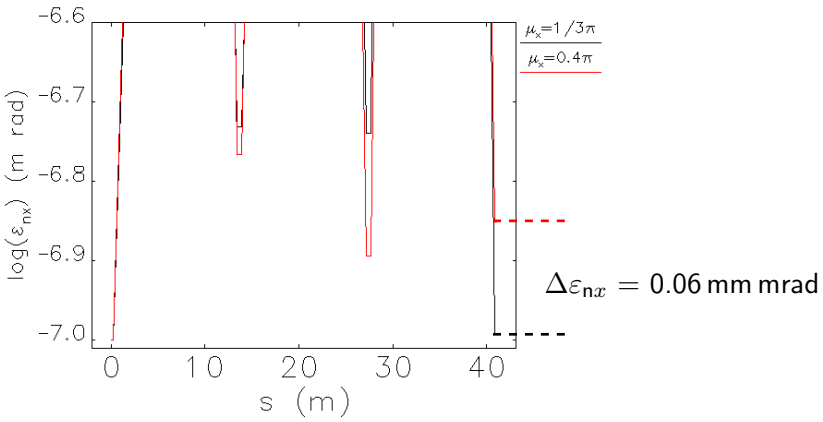

Figure 5.5: Tracking simulations showing the compensation scheme of the CSR-induced horizontal emittance growth.

the phase advance and only in the $\Delta\mu_x(i) = (1/3)\,\pi$ case is the emittance fully recovered after the third cell. These simulation results highlight the vulnerability of this method if the phase advance is not exact.

The notion of CSR-induced emittance growth compensation scheme using the phase advance over repetitive cells is used in the high energy arc optic of the FSF case study, see Chapter 6.3. The following section investigates the possibility of producing optic for a single compact cell that fulfills the CSR wake correction and allows bunch compression.

5.2 CSR Emittance Growth Suppression and Bunch Compression in a Compact Arc

The assumption that the Hajima CSR wake dispersion function Eq. (5.5) describes a constant 1D wake that is sub-sequential and predictable is developed further in this section. Combining this and the standard 6x6 transport matrix Eq. (3.1), one can theoretically gather together a set of equations by way of the Courant-Snyder parameters for a single TBA to be solved. The solution would then theoretically incorporate all the advantages of emittance compensation and allow the possibility of bunch compression in one single compact arc.

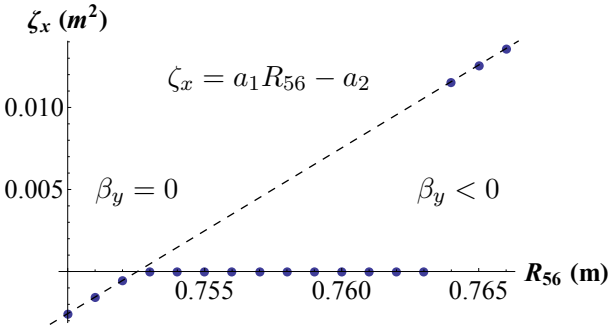

Figure 5.6: CSR wake dispersion function for a given R_{56} value.

Consider again a TBA, but in this section consisting of three identical 60 ° dipoles with two sets of symmetrical triplets. The bending radius $\rho = 1.3\,\mathrm{m}$ is chosen with a maximum field of 1 T in order to make the optic comparable with modern compact ERLs. Identifying R_{56} as a free parameter, one can solve the system numerically.

Plotting the CSR wake function against the free parameter of longitudinal dispersion generates a mathematical region of solutions for full compensation $\zeta_x = 0$ of the CSR wake. Fig. 5.6 also suggests there is a linear relationship either side of the zero wake region where a_1 and a_2 are constants.

The plotted points are mathematically feasible solutions but not necessarily physical or practical for magnetic optic. Multiple solutions for the quadrupole strength exist in the zero cross $\zeta_x \sim 0$ region. Through further investigations about this intersection one can find a stable periodic solution for the transversal betatron functions in both planes about the $R_{56} = 0.755\,\mathrm{m}$ mark. Further optimization allowed the construction of a 180 ° bend Fig. 5.7 with reasonable optic functions.

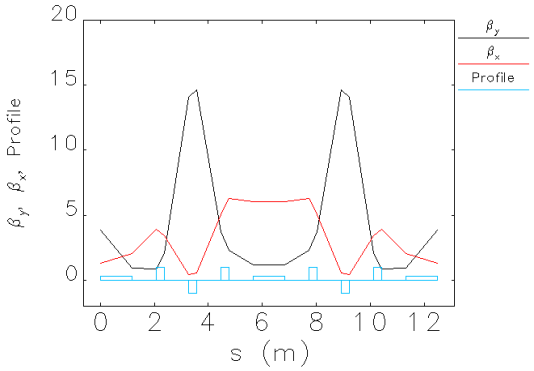

Figure 5.7: Stable periodic Twiss-parameters of the $R_{56} = 0.755\,\mathrm{m}$ solution.

For completeness, the trend of the CSR wake dispersion function over the proposed optic is shown in Fig. 5.8. Again as in the case of the three repeating TBA structures where the phase advance was a prerequisite, full compensation occurs. Notably here though these effects are suppressed and confined to one single TBA structure. The resulting optic from this analytical solution by combing the Hajima 5x5 and transport 6x6 matrices seems promising. The relatively large value of $R_{56} =$

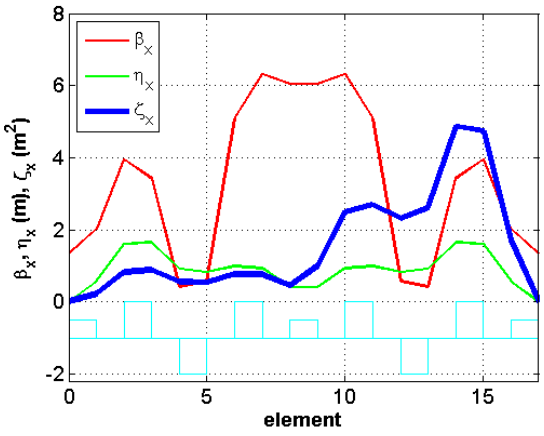

Figure 5.8: CSR wake dispersion function for a single TBA 180 ° bend.

0.755 cm is due to the initial restraints on the bend. The arc length could be reduced by a factor of two, which would again half the value of the longitudinal dispersion. One could also envisage an optic based on a smaller bending angle, which over many cells would compose of a slow varying R_{56} value with many phase advance matching sections [38]. This thesis resigns itself to a compact optic which is relevant to todays machines. Even with periodic optic, these compact arcs are susceptible to higher order aberrations. The following section examines the impact of certain key terms to compensate emittance growth.

5.3 Correction of Chromatic Aberrations

Horizontal phase advance manipulation has been used in the previous section to suppress the distortion of the transversal phase space due to CSR. The aberrations investigated here are caused by the variation of the focal length of a quadrupole with energy. For a bunch of zero charge but with a finite energy spread δ the impact of CSR is null. ISR effects have been shown in Chapter 2.2 to be heavily dependent on the beam energy. Therefore the tracking simulations were undertaken at the FSF injection energy of 240 MeV. In order to study the transport of a particle through a magnetic system with a higher precision, the matrix multiplication is truncated to higher orders using a Taylor expansion about the central trajectory. The general formula for the 2nd order matrix analysis is given by Eq. (5.6). This transfer map is a composition of both 1st (R) and 2nd (T) order terms. Given that C describes a transformation of $A \rightarrow B$, then the sequence of the matrix multiplication is the usual manner $C = BA$.

$$T^C_{ijk} = \sum_l^6 R^B_{il} T^A_{ljk} + \sum_l^6 \sum_m^6 T^B_{ilm} R^A_{lj} R^A_{mk} \tag{5.6}$$

Rather than using the standard technique implementing multipoles to manipulate 'all' the higher matrix terms in order to optimize the chromatic dependence of the tune, $\xi = Q/(\Delta p/p)$ a simpler novel approach has been undertaken to find the key 2nd order terms which stimulate transversal emittance growth. Consider the chromatic aberrations in the horizontal plane given by

$$\begin{aligned} x_1 &= T_{161}\delta_0 x_0 + T_{162}\delta_0 x'_0 + ... \\ x'_1 &= T_{261}\delta_0 x_0 + T_{262}\delta_0 x'_0 + ... \end{aligned} \tag{5.7}$$

The common T_{i66} terms that couple to the square of the energy spread δ_0^2 are purposely neglected at this stage with the notion that they will be accounted for in the longitudinal emittance compensation scheme proposed in Chapter 6.4.2 which is complementary to this approach. Without them the mathematics at this stage is simplified and useful relations of the remaining 2nd order terms can be found and studied. The horizontal emittance change can be approximated as

$$\begin{aligned} \varepsilon_1^2 &= \langle {x_1}^2 \rangle \langle {x'_1}^2 \rangle - \langle x_1 x'_1 \rangle^2 \\ &= \langle (T_{161}\delta x + T_{162}\delta x')^2 \rangle \langle (T_{261}\delta x + T_{262}\delta x')^2 \rangle \\ &- \langle (T_{161}\delta x + T_{162}\delta x')(T_{261}\delta x + T_{262}\delta x') \rangle^2 \end{aligned} \tag{5.8}$$

After a lengthly cross multiplication many similar terms cancel out leaving

$$\varepsilon_1^2 = (T_{161}T_{262} - T_{162}T_{261})^2 \left(\langle \delta_0^2 x_0^2 \rangle \langle \delta_0^2 {x'}_0^2 \rangle - \langle \delta_0^2 x_0 x'_0 \rangle^2 \right) \tag{5.9}$$

One can interpret Eq. (5.9) as a useful tool to suppress the transverse emittance growth. By implementing a family of sextupoles so that for the horizontal plane $T_{161}T_{262} = T_{162}T_{261}$ and likewise for the vertical plane $T_{363}T_{464} = T_{364}T_{463}$ the magnitude of the chromatic emittance growth is reduced.

The proposed technique is a new approach and suitable to the transport of beams of very low emittance with notable energy spread. This technique relaxes the restrictions on other essential 2nd order terms such as T_{566} that play an integral role in bunch compression. In the following section this approach is derived using the standard 2nd order tensors and then validated with tracking simulations. The principle notion here is to analytically verify that when

$$\Sigma_x = T_{161}T_{262} - T_{162}T_{261} = 0 \tag{5.10}$$

minimal chromatic emittance growth is found. Given $m = 6$ and $k = 6$, Eq. (5.6) is reduced to just a handful of energy dependent terms

$$T^C_{ij6} = \sum_l^6 R^B_{il} T^A_{lj6} + \sum_l^6 T^B_{il6} R^A_{lj} R^A_{66} \tag{5.11}$$

The 2nd order notation as defined in [39] was used for a simple transferline consisting of a bend, drift, quadrupole and sextupole. The bending magnet has a bending angle of $\theta = 60^\circ$ and length l. k_q and l_q represent the quadrupole strength and length respectively. The drift between the sbend dipole and quadrupole is 0.9 m long and the chromatic focus is corrected using a sextupole of length l_s as shown in Fig. 5.9. The relevant 2nd order notation needed for the elements in the beamline is listed overleaf. Note the quadratic dependence of the sextupole strength k_s will result in more than one solution.

One can estimate realistic limits for the energy independent quadrupole and sextupole strengths used in this beamline at 240 MeV. Using the Taylor expansion of the magnetic field, setting the maximum pole field to $B_{\max} = 1\,\mathrm{T}$ and assuming a vacuum chamber radius of $r_{\max} = 2\,\mathrm{cm}$ is sufficient, the quadrupole strength becomes

$$k_q = \frac{e}{pc}\frac{B_{\max}}{r}\bigg|_{r_{\max}} = \frac{300}{240}\cdot\frac{1}{0.02} \simeq 60\,\mathrm{m}^{-2} \tag{5.12}$$

Likewise for the sextupole one finds

$$k_s = \frac{e}{pc}\frac{2B_{\max}}{r^2}\bigg|_{r_{\max}} = \frac{300}{240}\cdot\frac{2}{0.02^2} = 6250\,\mathrm{m}^{-3} \tag{5.13}$$

The radial magnetic field of a sextupole is given by

$$B_r = B_{\max}\left(\frac{r}{r_{\max}}\right)^2 \tag{5.14}$$

Using Ampère's law over a closed path one finds

$$\oint B\cdot \mathrm{d}l = \frac{1}{3}B_{\max}\, r_{\max} = \mu_0\, I \tag{5.15}$$

where μ_0 is the vacuum permeability. This correspond to a sextupole current of $I = 5\,\mathrm{kA}$ which is technically feasible with say 100 turns of 50 A.

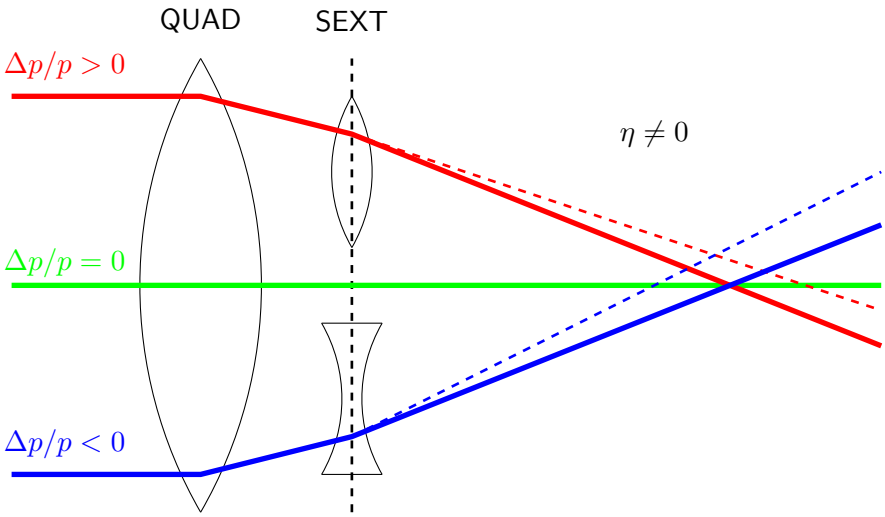

Figure 5.9: Chromatic correction using a sextupole [40].

The complete matrices and tensors for the bend, drift, quadrupole and sextupole transferline were symbolically multiplied together in a successive manner $C = BA, E = DC, F = ED...$ using the relevant definitions below until a general formula was found.

QUAD

$$T_{161} = \frac{1}{2}\sqrt{k_q}\, l_q \sin\left(\sqrt{k_q}\, l_q\right)$$

$$T_{162} = \left(\frac{1}{2\sqrt{k_q}}\right) \sin\left(\sqrt{k_q}\, l_q\right) - \left(\frac{l_q}{2}\right) \cos\left(\sqrt{k_q}\, l_q\right)$$

$$T_{261} = \frac{\sqrt{k_q}}{2}\Big(\sqrt{k_q}\, l_q \cos\left(\sqrt{k_q}\, l_q\right) + \sin\left(\sqrt{k_q}\, l_q\right)\Big)$$

$$T_{262} = \frac{1}{2}\sqrt{k_q}\, l_q \sin\left(\sqrt{k_q}\, l_q\right)$$

DRIFT

$$T_{1jk} = 0$$

$$T_{2jk} = 0$$

SBEND

$$T_{111} = -\frac{1}{2}\left(\frac{\theta}{l}\right) \sin^2\theta$$

$$T_{121} = \sin\theta\cos\theta$$

$$T_{122} = \frac{1}{2}\left(\frac{l}{\theta}\right) \cos\theta\Big(1 - \cos\theta\Big)$$

$$T_{144} = -\frac{1}{2}\left(\frac{l}{\theta}\right)\Big(1 - \cos\theta\Big)$$

$$T_{161} = \sin^2\theta$$

$$T_{222} = -\frac{1}{2}\sin\theta$$

$$T_{244} = -\frac{1}{2}\sin\theta$$

$$T_{261} = \left(\frac{\theta}{l}\right)\sin\theta$$

$$T_{266} = -\sin\theta$$

SEXT

$$T_{111} = -\frac{1}{4}k_s^2\, l_s^2$$

$$T_{121} = -\frac{1}{6}k_s^2\, l_s^3$$

$$T_{122} = -\frac{1}{24}k_s^2\, l_s^4$$

$$T_{126} = -\frac{l_s}{2}$$

$$T_{211} = -\frac{1}{2}k_s^2\, l_s$$

$$T_{221} = -\frac{1}{2}k_s^2\, l_s^2$$

$$T_{222} = -\frac{1}{6}k_s^2\, l_s^3$$

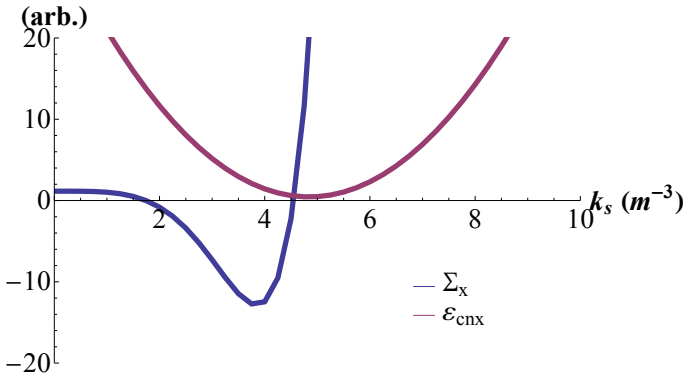

Figure 5.10: Tracking results of the horizontal emittance and associated Σ_x correction scheme value for various sextupole settings.

The symbolic output is very large but by implementing the optical parameters for the magnetic elements the formula simplifies to a fourth order parabola, the blue curve in Fig. 5.10. As expected, two roots of the parabola exist in the positive k_s domain due to the quadratic definition of the sextupole strength in the tensor notion. Particle tracking for various k_s was simulated in Elegant to find the minimal emittance ε_{cnx}. In this example the dispersion has been subtracted, red curve in Fig. 5.10. As anticipated, the minimum emittance occurs when $\Sigma_x \to 0$.

This concept is implemented into the 1 GeV recovery arc for the FSF as described in Chapter 6.4.3 to aid the safe passage of the beam to the dump. At this energy the sextupole strength is $|k_s| \sim 50\,\text{m}^{-3}$. This value is a magnitude less than the technical limits for sextupoles estimated using Eq. (5.13). This would relax the operational constraints of the sextupole magnets and the design of the vacuum chamber for such an arc.

In the following section, this positive result is implemented into the compact 180 ° arc derived in Chapter 5.2 and compared to the standard technique of chromaticity correction using particle tracking simulations.

5.4 The Compact Arc with Chromatic Correction

This section investigates the implication of setting the sextupoles in the compact arc so that $\Sigma_x = 0$. A reasonable test to validate its effectiveness for minimal emittance growth by 2nd order correction is to compare the theory with standard chromaticity correction where

$$\xi = -\frac{1}{4\pi}\oint \beta\big(k_q - k_s\eta\big)\mathrm{d}s \;\to\; 0 \tag{5.16}$$

In order to have maximum impact for minimal sextupole strength, the magnets are symmetrically positioned at largest $\beta\eta$. This point is on the inner side of the first and last quadrupole of each triplet. The natural chromaticity (when $k_s = 0$) of the optic is $\xi_{nat} = -1.46$.

Particle tracking simulations were undertaken for an input beam of zero charge with various correlated energy spreads. The initial bunch length was chosen as 5 ps to correspond with the measurements taken in Chapter 3.2 at the ALICE ERL facility. Full compression should then occur at $\Delta E/E \sim 2{\cdot}10^{-3}$ for the linear optic, devised in Chapter 5.2 when $R_{56} = 0.755\,\text{m}$. With these settings the CSR-induced emittance growth is suppressed and compression is possible. The sextupole strength was then scanned as shown in Fig. 5.11 to find the value of k_s for minimal emittance growth.

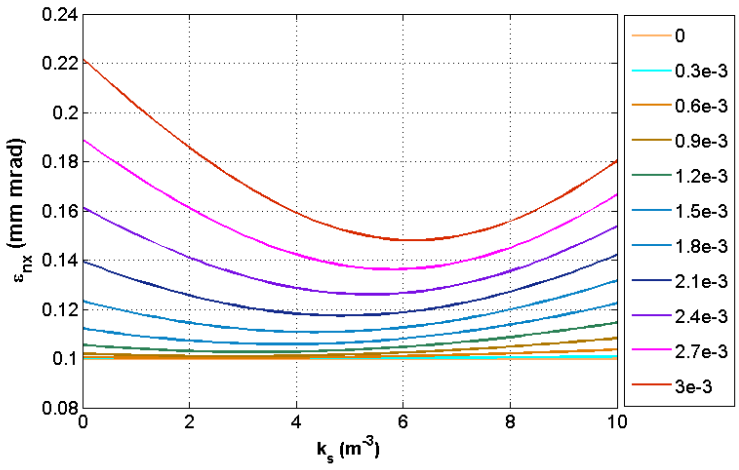

Figure 5.11: Locating the sextupole strength for minimum emittance growth as the correlated energy spread in the beam increases.

The values of Σ_x and ξ are plotted in Fig. 5.12 for each point of minimal emittance. The trend shows that as the energy spread is increased, the chromaticity setting moves away from the natural value of -1.46 towards -1. Therefore a full correction of $\xi \rightarrow 0$ would lead to excessive emittance growth. This result is not uncommon as many light sources operate with non-zero chromaticity settings in order to suppress other effects [41].

One needs however to make a clear distinction here between single pass and storage ring based light sources. The compact ERL arc is considered as a single pass transferline and sextupole optimization is focused either on the suppression of emittance growth, bunch compression or on both in parallel. Fig. 5.12 shows (red line) the value of Σ_x as the correlated energy spread increases. The value tends towards zero as predicted in the analytic derivation from the previous section, as the beam becomes more susceptible to chromatic aberrations.

The compact arc is envisaged to transport a charged beam with a correlated energy spread due to off-crest acceleration. Suppression of CSR induced emittance growth for bunch compression from $2 \rightarrow 0.1$ ps with and without sextupole correction is shown in Fig. 5.13. Full radiations effects are simulated here.

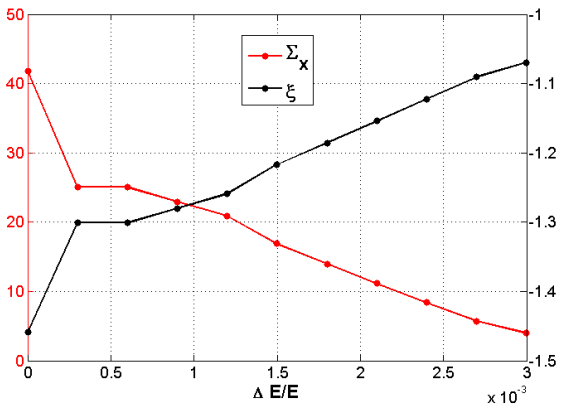

Figure 5.12: Comparison of Σ_x correction and chromaticity ξ values at minimum emittance as the correlated energy spread in the beam increases.

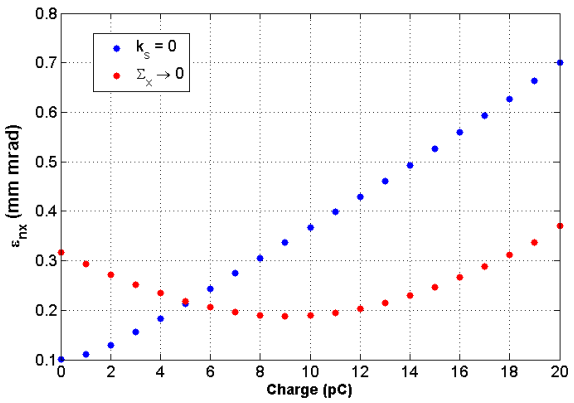

Figure 5.13: Simulation results for the compact arc for beams of various charge.

Fig. 5.13 reflects how the theory has developed over the chapter. The optimized solution with sextupoles (red dots), shows that the optic responds positively for bunch charges above 5 pC. Below this value the addition of sextupoles set so $\Sigma_x \rightarrow 0$ will only induce unnecessary aberrations. In the simulations the RF chirp was chosen so the bunch length after compression with and without sextupoles remains relatively constant for the different bunch charge settings. The minimum at 10 pC represents an equilibrium of three processes. Firstly, CSR increases the energy spread and causes transverse emittance growth. Secondly, the linear optic found using the Hajima technique suppresses the emittance growth. Then thirdly, the extent of the chromatic emittance growth using sextupoles to set $\Sigma_x = 0$ depends on the energy spread. A common balance is eventually found.

The case study in the following chapter presents the magnetic optic for a complex multi-turn ERL. Phase advance manipulation techniques like those developed in this chapter are used in the high energy arcs to suppress CSR induced emittance growth. Additional chromatic correction using sextupoles to help minimize the emittance growth is carried out throughout the facility to ensure the safe passage of the short pulse mode operation. In particular the $\Sigma_x \rightarrow 0$ technique is used on the beam recovery side of the light source as the energy spread begins to play a critical role at the beam dump. The 2$^{\text{nd}}$ order tensor analysis notion is again investigated in Chapter 6.4.2 to manipulate the normalized longitudinal emittance to help produce the shortest possible bunch lengths.

6. The Femto-Science Factory

Design studies for a future multi-turn ERL based light source are presently been investigated at Helmholtz-Zentrum Berlin. The group has been working on the various requirements of such a facility. Continuing on from the introduction in Chapter 1, the beam parameters need to be at least a magnitude better than the ones produced in existing 3rd generation light sources. This chapter introduces the philosophy behind the ERL based light source, outlines the main acceleration stages and presents the results of the start-to-end simulations for the main operation modes. In keeping with the theme of this thesis, particular attention is paid to the more relevant studies to produce an ultra-short bunch.

6.1 Machine Design and Philosophy

The philosophy behind the Femto-Science Factory (FSF) takes advantage of using a linac to produce minimal transverse emittance. For a linac based facility the transversal emittance ε_x is inversely proportional to the beam energy γ. For a given injection emittance ε_{x0}, the higher the beam energy the lower the possible beam emittance. At an energy of 6 GeV a normalized emittance of 0.1 mm mrad is necessary to produce diffraction limited radiation at Angstrom wavelengths.

$$\text{ERL} \quad \varepsilon_x \sim \varepsilon_{x0}/\gamma \qquad \text{RING} \quad \varepsilon_x \sim \gamma^2/N^3$$

For ring based facilities the equilibrium emittance increases quadratically with the circulating beam energy. A further optimization between energy and the number of bending magnets N is possible, as in the ultimate storage ring proposals [42] but the common steady state limitations still exist. The beam in an ERL based light source does not reach such an equilibrium state during the short time required for multiple turns allowing high temporal resolution. Short radiations pulses in the region of a few tens of femtoseconds are envisaged. The FSF is intended to be a multi-user facility and offer a variety of operation modes. Fig. 6.1 shows the layout of the light source. The scale of this

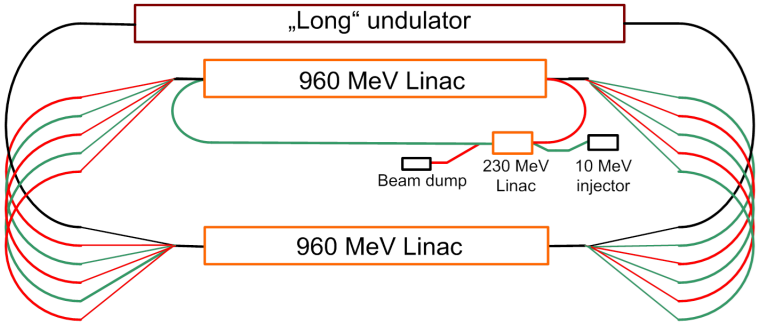

Figure 6.1: Schematic of the FSF Multi-Turn ERL.

Table 6.1: Main design parameters of the FSF.

Parameter	LEM	SPM
Injector + Linac (MeV)	240	
Main Linacs (MeV)	960	
Final Energy (MeV)	6000	
Rep. Rate (GHz)	1.3	
Charge (pC)	15	5
Emittance (mm mrad)	0.1	0.4
Bunch Length (fs)	2000	10
$\langle B \rangle$ (ph/s/mm^2/mrad^2/0.1 %)	10^{22}	10^{21}
B_p (ph/s/mm^2/mrad^2/0.1 %)	10^{26}	10^{26}

large facility is designed to be in the order of (400x400) m^2. Independent orbit acceleration (green) and deceleration (red) traverse about two long SRF linacs. For the Low Emittance Mode (LEM) a beam of higher charge is accelerated on-crest in all of the linacs and circulates round arcs that are both achromatic and isochronous. The LEM is the primary mode. The secondary Short Pusle Mode (SPM) must use the magnetic elements preliminarily designed for the LEM. No additional beamlines are foreseen and the two modes must complement each other. The main difference in the two modes with regards to the lattice design occurs in the lower energy sections of the machine. The SPM relies on achromatic arcs in these lower energy stages and off-crest acceleration for bunch compression. The modes share common high energy arcs where radiation effects play an important role in emittance growth.

The vertical spreaders geometry has been designed so that the total length of each structure is restricted to 25 m. Magnets are shared between energies when separation is no longer possible. The optic is achromatic and isochronous, contains sextupoles to correct the 2$^{\mathrm{nd}}$ order for high energy spread beams, and the betatron functions are minimized throughout. Due to these heavy demands, the 4 and 6 GeV spreaders bend in both transversal planes and solenoids are implemented to correct the rotation of the coupled betatron oscillation.

The main design parameters of the FSF are listed in Table 6.1. A SRF injector based originally on the design parameters of bERLinPro [43] injects the 10 MeV electron beam into a 230 MeV accelerator. The beam is then transported onwards to two equally long linacs. After three passes in each 960 MeV linac a final beam energy of 6 GeV is reached. Each arc contains straight sections for undulators and the final energy arc permits a long straight section for 3000 period long undulators. Values for the brilliance are given at full current. The electron beam quality delivered to the long undulators and hence the photon brilliance attainable depends on the machine operating mode.

The remaining sections in this chapter present the main aspects of the FSF. Firstly, the staged injection scheme is introduced then the expectations of the LEM as the primary mode are presented. The topic then turns to the SPM which is the theme throughout this thesis. A design based on linear uncoupled optic helps address a proof-of-principle for the SPM bunch compression scheme. Emittance preservation in all planes during beam transport and acceleration is investigated and rigorously tested using particle tracking simulations. The reimbursement strategy for the energy loss due to radiation and an alternative recovery mode are implemented into the start-to-end simulations. The chapter ends by taking a closer look into the photon beam properties attainable in the long undulator section and investigates the possibility of ultra-high brilliance from coherent amplified light.

6.2 Two Stage Injection

A staged injection was incorporated into the FSF. The benefits of including an intermediate linac and staging the injection is comprehensively discussed in [44]. Simulations show that a higher injection energy increases the Transversal Beam Break-Up (TBBU) threshold in the first split linac. Here a compromise between the injection and main linac energy was found for a two staged scheme.

The additional linac and arc are also useful for bunch compression. The combination of off-crest acceleration in the linac and the R_{56} in the arc compress the beam from 2 to 1 ps in both operation modes. Investigations described in Chapter 6.4.3 show the extent of the compression at this stage is critical for the optimum beam parameters at high energy. Next generation light sources require CW linac operation to achieve high average currents. This sole desire has supported the development of SRF based injectors. Although higher peak field gradients are attainable using normal conducting technology the duty cycle remains low. Also, the lowest emittance in CW mode operation is achievable only with SRF based photo-injectors.

Fig. 6.2 shows a schematic of the FSF injector. A booster module of three cavities is implemented directly after the SRF gun to combat the space charge forces acting on the bunch at low energy which are seen as the main limitations on the transversal emittance. The merger section shares a final bending magnet in the transferline chicane of the 2nd stage of the injection loop on route to the main 230 MeV injector linac. The first few cavities, not shown, of this linac are also used in the emittance optimization as space charge forces are still significant up to a beam energy of 50 MeV. Hence the injection energy is referred here as 50 MeV rather than 10 MeV as quoted in the introduction to this chapter.

Table 6.2 shows the beam parameters of the subtle transformation through the space charge dominated injection process to produce a low emittance beam in both transverse planes. On the contrary, producing a femtosecond, low energy spread pulse requires compression whenever feasibly possible. The longitudinal electron beam properties given in Table 6.3 for the SPM, are fundamentally re-

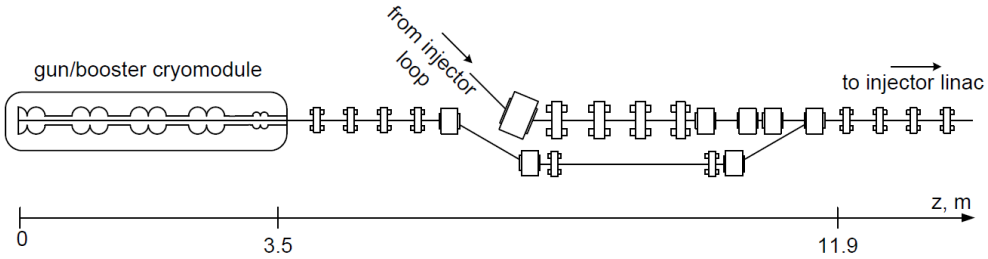

Figure 6.2: Schematic of the injector elements, merger and arc optic on route to the linac.

Table 6.2: Injector parameters from ASTRA [45] simulations of the 15 pC LEM.

Pos.	ε_{nx} (mm mrad)	ε_{ny} (mm mrad)	σ_z (mm)	Energy (MeV)
Gun	0.27	0.27	2.50	1.91
Booster	0.22	0.22	2.38	9.45
Merger	0.19	0.16	0.95	9.45
Injection Linac	0.13	0.09	0.93	53.41

Table 6.3: Injector parameters from ASTRA simulations of the 5 pC SPM

Pos.	ε_z (keV mm)	σ_z (mm)	Energy (MeV)
Gun	11.05	2.37	1.90
Booster	0.84	2.23	9.47
Merger	1.11	0.63	9.47
Injection Linac	2.36	0.60	53.41

stricted by the physical nature of the laser pulse length and spot size on the cathode. The bunch length σ_z is also compressed to help achieve peak brilliance in the later stages of the FSF.

At the slight expense of the beam energy, a 3rd harmonic cavity positioned at z = 3.1 m in Fig. 6.2 is used to decelerate the beam as shown in Fig. 6.3a. This action linearizes the longitudinal phase space [46] and consequently lowers the longitudinal emittance as shown in Fig. 6.3b. The harmonic cavity decelerates the beam on-crest to linearize the RF curvature imprint on the phase space produced in the earlier cavities. Taking E_{01} as the sum of the amplitudes in the gun and booster cavities and E_{03} for the harmonic cavity, one finds

$$E_1 = E_{01}\cos\omega t \quad , \quad \frac{\mathrm{d}^2E_1}{\mathrm{d}t^2} = -\omega^2 E_{01}\cos\omega t$$

$$E_3 = E_{03}\cos 3\omega t \quad , \quad \frac{\mathrm{d}^2E_3}{\mathrm{d}t^2} = -9\omega^2 E_{03}\cos 3\omega t$$

The aim of the harmonic cavity is to nullify the 2nd time derivative of the energy gain

$$\left.\frac{\mathrm{d}^2(E_1+E_3)}{\mathrm{d}t^2}\right|_{t=0} = 0 \quad \rightarrow \quad E_{03} = -\frac{E_{01}}{9} \tag{6.1}$$

Fig. 6.3a shows the energy reduction to be not exactly a 9th of the total energy as estimated in Eq. (6.1). This is because the acceleration is not on-crest in the simulations and there are also time transit factors associated with low energy acceleration and finite bunch lengths in the gun.

The start-to-end simulations leave ASTRA at this stage in the facility. The ASTRA beam distributions at 50 MeV for both modes are converted, matched and tracked onwards using Elegant. The space

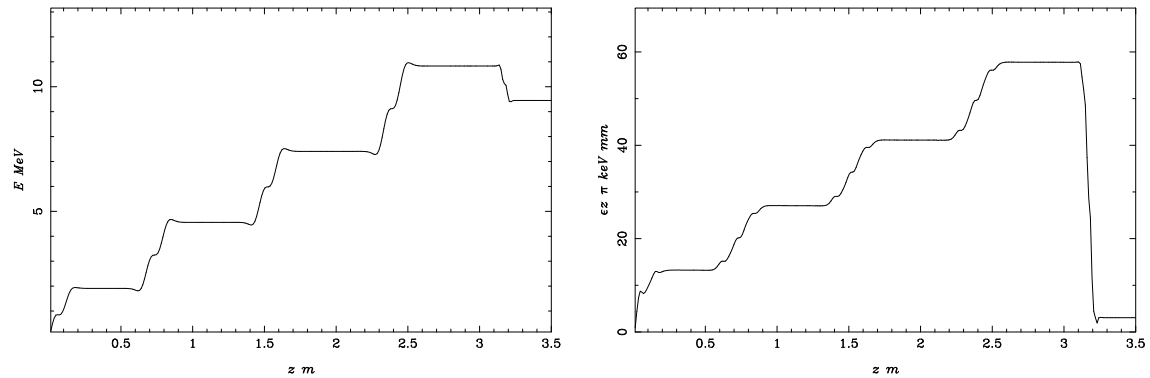

(a) Beam energy. (b) Longitudinal emittance.

Figure 6.3: Linearization of longitudinal phase space to recover the longitudinal emittance of the cathode using a 3rd harmonic cavity at $z = 3.1$ m.

charge effects above 50 MeV are negligible so the remaining 8 km long optic of the FSF was simulated using Elegant to save on computational expense. A possible scenario to make good use of the 100 m long transferline between the 230 MeV injector and arc is to envisage optic that may be used at a future date to aid the non-linear beam dynamics. For example, on the acceleration side, green in Fig. 6.1, a series of laser heater undulators could be implemented and used to suppress the micro-bunching instability at the expense of the longitudinal emittance. Such a scheme could be based on [47], where a TiSa laser is used to overlap and interact with the electron beam. At this relatively low energy stage with $\gamma = 480$, one could consider a laser of wavelength $\lambda = 800\,\text{nm}$ and routine undulator parameters to develop this interaction.

The following section describes the beam parameters of the LEM. The relevance to this thesis is that both LEM and SPM operation share the same magnetic elements. The two modes should be compatible and share the same optic where possible.

6.3 Low Emittance Mode

Elegant was used for the start-to-end tracking simulations. Elegant is capable of tracking particles through large complex lattice structures that incorporate all the relevant elements needed for acceleration and beam transport. For the simulations, all radiations effects are present [48] and 100 000 particles are tracked unless otherwise stated.

The schematic of the FSF presented in the machine design and philosophy section earlier in this chapter is depicted again in Fig. 6.4a as a blueprint for the simulations. The arcs are aligned so that they would fit in a single tunnel, and the independent energy orbits are stepwise stacked above each other.

The Fig. 6.4b blueprint depicts the dashed region in Fig. 6.4a. The figure highlights the injection stage, first 1 GeV split linac and the multiple orbits. The bunch is injected at the (0,0) origin and dumped approximately at coordinate (45,1). The philosophy of the optic design is to share magnets between the different energy beamlines where possible and hold planar symmetry. The first dipole of the low energy recovery arc at (5,-7) is used as part of the chicane merger to the split linac section.

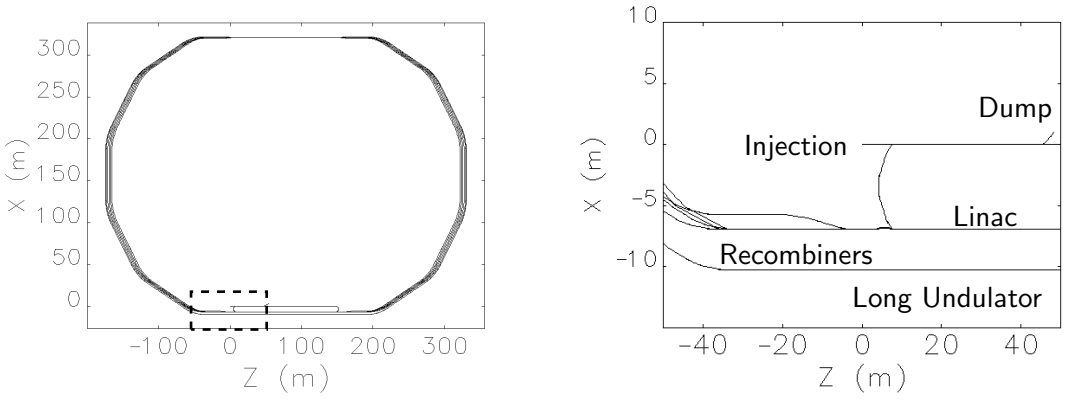

(a) Blueprint of the FSF.

(b) Blueprint of the dashed injection region.

Figure 6.4: The FSF as depicted by the simulation program.

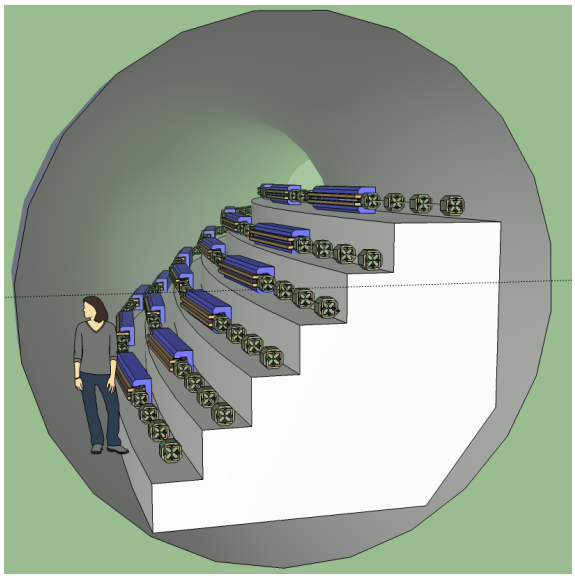

Figure 6.5: Stepwise magnetic arrangement in the tunnel.

The spreaders and recombiners are used to stack the arcs into the tunnel depending on the orbit energy. The long undulator is slightly offset from the first split linac. Fig. 6.5 shows the low energy 1 GeV orbit at the top of the stairwell and both accelerating and decelerating beams are present. The energy of the bunch as shown in Fig. 6.6 is symmetrically increased from 50 MeV in the injector to a final beam energy of 6 GeV and then recovered to 10 MeV in the dump. After twelve passes, the total linac length traversed is approximately a 5^{th} of the facility length.

Sections of four quadrupoles and suitably long drifts are used to match the transverse betatron functions between the different stages throughout the machine. The length of the matching sections are adjusted to set the path lengths to $N\lambda_{\text{RF}}/2$ for recovery. The maximum betatron function value in the linacs is approximately given by the length of the linac, $\beta_{x,y} \sim L_{\text{LINAC}} \sim 100\,\text{m}$. This value is then at least doubled in the first few quadrupoles of the spreaders to produce peaks over 400 m as seen in Fig. 6.7. The heavy demands on the optic in the spreaders were discussed in Chapter 6.1. The optic in the linac is designed to suppress the TBBU instability. Triplets are positioned between the cryomodules to minimize the betatron functions and increase the TBBU thresholds [44].

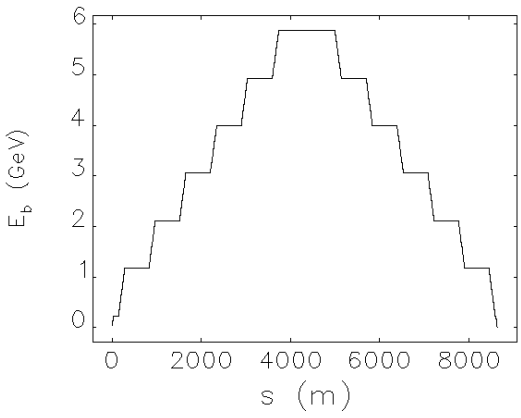

Figure 6.6: Energy of the bunch throughout the FSF.

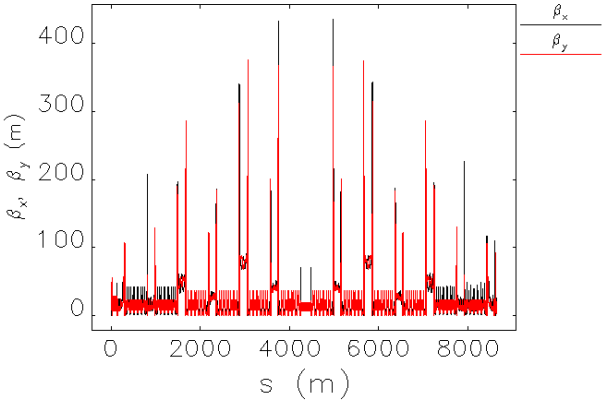

Figure 6.7: Transverse betatron functions along the FSF.

The high energy arcs in Fig. 6.7 between 2 km $<$ s $<$ 7 km, are designed to manipulate the horizontal phase advance to nullify CSR induced emittance growth using the theory described in Chapter 5. The 8 km long optic is mostly periodic and repeats throughout each arc. Fig. 6.8a shows the Twiss-functions for two 30° cells of the high energy arc each with a horizontal phase advance $\Delta\mu_x = 2\pi \cdot 3/4$. There are additional quadrupoles at the beginning and end of each cell to match the Twiss-parameters to those needed for the undulator sections between the bending cells. The dispersion shown in light blue is closed in all the cells and they are also isochronous prohibiting first order compression $R_{56} = 0$. Triplets are used in the undulator section to focus the beam in both planes to $\beta_{xy} \sim 10$ m.

Shown in Fig. 6.8b is a 7.5° cell of a 30° bend. Here dipoles of bending angle 4.05° shown in blue are separated by quadrupoles in green and a short -0.6° bend anti-magnet dipole also blue. The anti-magnet allows one to keep the overall quadrupole strength low as there is no need to actively change the sign of the dispersion to ensure $R_{56} = 0$.

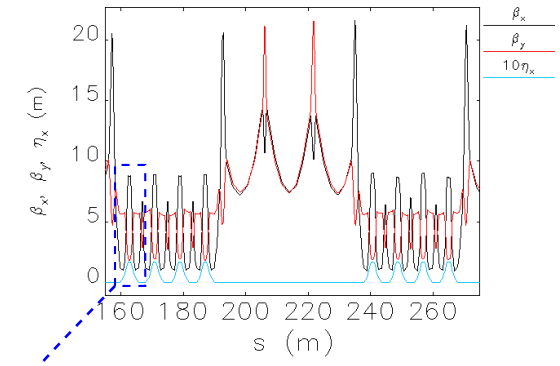

(a) Twiss-functions.

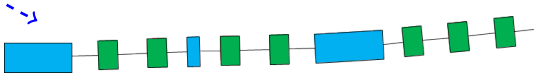

(b) Schematic of a 7.5° cell with anti-magnet.

Figure 6.8: Bend-undulator-bend section of high energy arc and periodic bending cell.

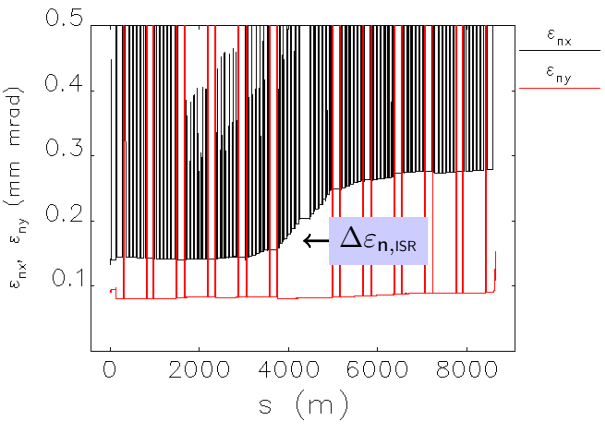

Figure 6.9: Transverse emittance plot along the FSF.

For the LEM, with all the suppression techniques described in place, the transversal emittance mainly grows due to ISR effects. This effect can be analytically estimated for a given arc using the radiation integral

$$I_5 = \int \frac{\mathcal{H}}{|\rho|^3}\,\mathrm{d}s \sim \frac{\theta^3}{\rho} \simeq 2 \cdot 10^{-5}\,[\mathrm{m}^{-1}] \tag{6.2}$$

where $\mathcal{H}(s)$ is the Courant-Snyder invariant for dispersion. The most effective option is to minimize the bend angle θ and maximize the radius ρ hence keeping the I_5 value as small as possible throughout the arc. The emittance growth due to ISR [49] in the 6 GeV arc is estimated as

$$\Delta\varepsilon_{\mathrm{n,ISR}} \sim 4 \cdot 10^{-8}\, E_{\mathrm{b}}^6[\mathrm{GeV}]\, I_5[\mathrm{m}^{-1}] = 0.04\,\mathrm{mm\,mrad} \tag{6.3}$$

which corresponds well with the value at $s \sim 4\,\mathrm{km}$ plotted in Fig. 6.9. The transverse emittance growth is kept to a minimum throughout the whole facility to utilize the undulator radiation in all acceleration and deceleration stages in order to maximize user potential. Plotted is both the horizontal and vertical normalized emittance including the dispersive contribution. It is this dispersion that produces the numerous black peaks in the horizontal arcs, and red only in the vertical spreaders.

The horizontal beam size σ_x as shown in Fig. 6.10 is a few tens of μm at the entrance to the long undulator. The emittance at this point in the facility is $\varepsilon_{\mathrm{n}x} = 0.2\,\mathrm{mm\,mrad}$. The projections of the phase space plots shown in Fig. 6.10a and Fig. 6.10c both portray Gaussian like particle distributions.

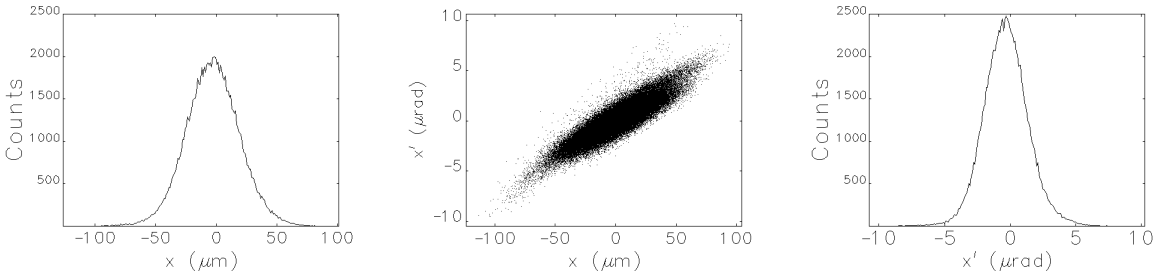

(a) x projection. (b) x , x' phase space. (c) x' projection

Figure 6.10: Horizontal beam distribution at the entrance to the long undulator.

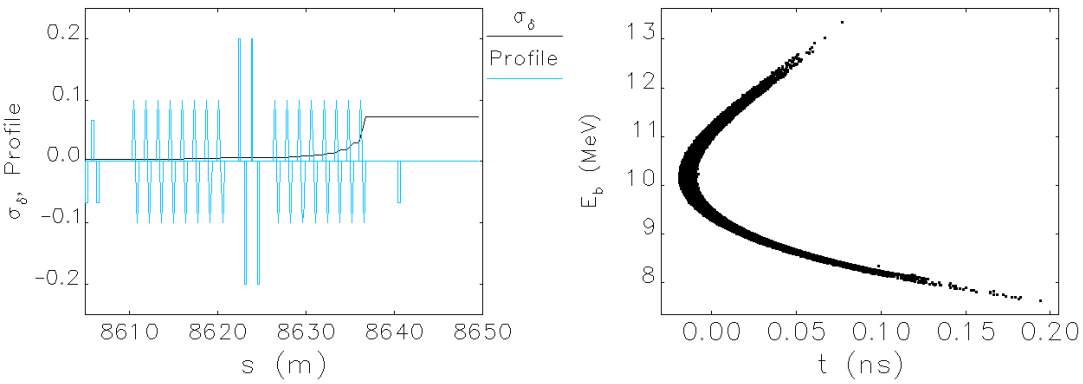

(a) Energy spread in the low energy recovery stage. (b) Longitudinal phase space plot at the 10 MeV dump.

Figure 6.11: Energy spread characteristics on recovery.

Table 6.4 summarizes the main beam dynamic parameters from the LEM start-to-end simulations at various stages in the facility. The input emittance, optimized in the injector Chapter 6.2, is close to the 0.1 mm mrad project goal value. The radiation effects double this emittance budget at 6 GeV.

Table 6.4 shows that the beam is still of very high quality even after the final recovery stage at 1 GeV. The normalized emittance is comparable with any present day 3$^{\text{rd}}$ generation light source. During the final deceleration stage the relative energy spread of the beam shown in Fig. 6.11a increases by a factor $E_{240\,\text{MeV}}/E_{10\,\text{MeV}} = 24$ to over 7 %. Fig. 6.11a also shows the trend of the energy spread in the low energy deceleration stage to the dump. The profile shows from left to right, firstly the three bending magnets of the low energy chicane, then the two linac sections separated by four matching quadrupoles and finally the bend at $s = 8640$ m is used to deliver the beam to the dump. Fig. 6.11b shows the longitudinal phase space plot of the bunch in the dump. The bunch length has increased from 3.6 ps to 19 ps due to the R_{56} in the bend used to transport the low energy bunch out of the recovery optic. An energy spread $\sigma_E < 10\,\%$ is seen as unproblematic for the dumpline. Additional quadrupoles in the dumpline after the final bending magnet are foreseen to correct the dispersion and produce a transversal beam size of 1 mm in both planes at the dump.

The optic for the LEM described in this section is fixed. The LEM is the primary mode in the FSF and the following sections on the SPM operation must use this magnetic lattice. However the implementation of sextupoles will be shown to be a necessity.

Table 6.4: Start-to-end beam parameters for the 15 pC LEM.

Pos	ε_{nx} (mm mrad)	ε_{ny} (mm mrad)	σ_t (ps)	σ_E (10^{-3})	Energy (MeV)
Input	0.13	0.09	3.09	2.93	50
1$^{\text{st}}$ user station	0.14	0.08	2.13	0.21	1000
Undulator	0.20	0.08	2.13	0.18	6000
Final user station	0.28	0.09	2.13	0.66	1000
Dumpline	1.24	0.11	3.60	7.26 %	10

6.4 Short Pulse Mode

The thesis so far has highlighted the motivation for the generation of short bunches and the limitations expected. The relevant longitudinal beam parameters have been experimentally determined in the low energy stages of existing ERL facilities. Compensation schemes for the reduction of transverse emittance growth have been presented and higher order optic designed to correct chromatic aberrations. This section expands these findings and integrates them into the FSF to theoretically produce a 10 fs bunch. The FSF philosophy introduced the facility layout and reiterated the primary operational mode is to achieve low emittance. The optic for the high energy arcs is fixed and common to both modes, so now attention is paid to the lower achromatic arcs to induce beam compression. A telescopic compression scheme is truncated to the 2nd order to incorporate the non-linear aspects of acceleration and compression. The model is then validated using particle tracking simulations and integrated into the start-to-end optic. The section ends with a brief summary of the beam energy loss due to radiation and describes an alternative recuperation method.

6.4.1 Telescopic Compression

The shortest pulse achievable from a multi-turn facility is with full compression in the final arc, shown in blue in Fig. 6.12. This method is however at the expense of a correlated energy spread. In order to remove the correlated energy spread and still produce a short pulse, consider an alternative solution based on a telescopic lattice, red in Fig. 6.12.

As only the lower energy arcs are available for compression, a scheme based on telescopic compression is implemented in the FSF [50]. In this regime the combination of the linac chirps and the R_{56} in the arcs are described as a simple focusing (F) and defocussing (f) lens system given by

$$\begin{pmatrix} c\Delta t \\ \delta \end{pmatrix}_1 \equiv \begin{pmatrix} f/F & F-f \\ 0 & F/f \end{pmatrix} \begin{pmatrix} c\Delta t \\ \delta \end{pmatrix}_0 \tag{6.4}$$

Taking the first two arcs as achromats and accelerating either side of on-crest in each linac, the two 'lenses' can share the same focal plane, just like in a telescope, to maximize the 'magnification' which is equivalent to the extent of the bunch compression. Furthermore the correlated energy spread due to the off-crest acceleration, the slope in each line, will be removed.

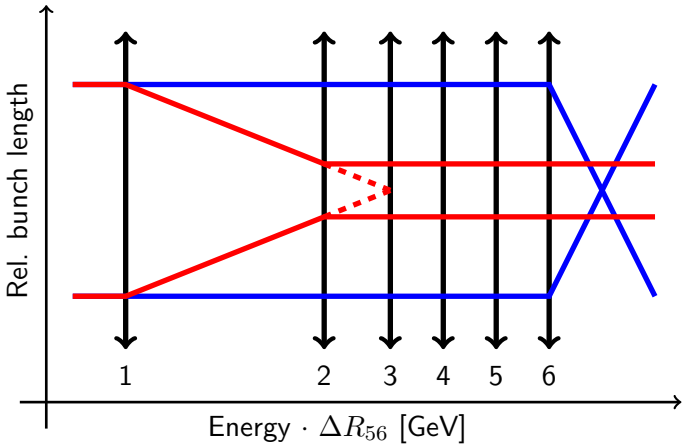

Figure 6.12: Pictorial representation of two bunch compression concepts; standard technique at full energy in Blue, telescopic scheme using the low energy arcs in Red.

The telescopic scheme is achievable using simple periodic optic such as double (DBA) or triple (TBA) bend achromats without excessive demands being placed on the strong focusing quadrupoles. Suitable values for the magnification were numerically investigated. A compromise between minimum bunch length and energy spread for the given linac phase and R_{56} values was found. The initial beam parameters are determined in the injector. Assuming $\sigma_t \sim \varepsilon_{0z}/\sigma_E$ and implementing an input beam of 2 ps, calculations show that the minimum bunch length is approximately 10 fs.

The parameters from the numerical calculations are seen as the starting point for the optimization of the start-to-end particle tracking simulations. The general compression scheme for the SPM is listed below. Each off-crest acceleration followed by achromatic arc constitute to a 'lens' in the telescopic compression scheme in the lower energy acceleration sections. The first two arcs up to a beam energy of 2 GeV have positive R_{56} values. On recovery the phase is shifted in both linacs $\phi_{\mathsf{d}} \rightarrow \phi_{\mathsf{a}} + 180\,^\circ$ (ERL process) and the recovery arcs have the corresponding negative R_{56} values.

The symmetry is required to help remove the correlated energy spread during deceleration and produce optimal beam conditions at the entrance to the beam dump. The following section develops the telescopic compression scheme to recover the longitudinal emittance from the injector using higher order magnetic optic.

General compression scheme for the FSF SPM

Off-crest acceleration $\phi_{1\mathsf{a}} = 100\,^\circ$, $\phi_{2\mathsf{a}} = 70\,^\circ$

Telescopic compression

Arc1 TBA $R_{56_1} = 20$ cm

Arc2 TBA $R_{56_2} = 5$ cm

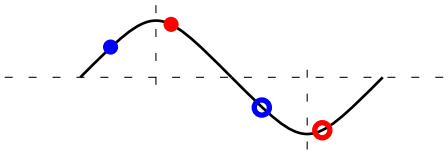

High energy arcs

3 GeV $\rightarrow$ 6 GeV DBA with anti-magnet, see Fig. 6.8

Off-crest deceleration $\phi_{1\mathsf{d}} = 280\,^\circ$, $\phi_{2\mathsf{d}} = 250\,^\circ$

High energy arcs

6 GeV $\rightarrow$ 3 GeV DBA with anti-magnet

Telescopic decompression

Arc2 TBA $R_{56_2} = -5$ cm

Arc1 TBA $R_{56_1} = -20$ cm

6.4.2 Non-linear Dynamics and Emittance Recovery

The longitudinal emittance is described in Chapter 1 as an ellipse occupying a density of particles in $(c\Delta t, \delta)$ phase space. The non-linear properties of the RF curvature due to acceleration can alter the phase distributions varying the normalized emittance. The longitudinal emittance compensation scheme uses the higher order magnetic terms created in the arc in combination with the off-crest acceleration to recover the longitudinal emittance of the injector. A full derivation up to 2$^{\text{nd}}$ order is given in the following.

$$\begin{aligned} \text{LINAC:} \qquad c\Delta t_1 &= c\Delta t_0 \\ \delta_1 &= \delta_0 + R_{65} c\Delta t_0 + T_{655}(c\Delta t_0)^2 \end{aligned} \tag{6.5}$$

$$\begin{aligned} \text{ARC:} \qquad c\Delta t_2 &= c\Delta t_1 + R_{56}\delta_1 + T_{566}\delta_1^2 \\ \delta_2 &= \delta_1 \end{aligned} \tag{6.6}$$

Using both the relative energy in the linac given by Eq. (6.5) and the bunch length variations in the arc from Eq. (6.6), one can calculate the emittance variation across the two stages

$$\begin{aligned} c\Delta t_2 &= c\Delta t_0 + R_{56}(\delta_0 + R_{65}c\Delta t_0 + T_{655}(c\Delta t_0)^2) + T_{566}(\delta_0 + R_{65}c\Delta t_0 + T_{655}(c\Delta t_0)^2)^2 \\ &\simeq c\Delta t_0 + R_{56}\delta_0 + R_{56}R_{65}c\Delta t_0 + R_{56}T_{655}(c\Delta t_0)^2 + T_{566}\delta_0^2 \\ &\quad +2T_{566}R_{65}\delta_0 c\Delta t_0 + T_{566}R_{65}^2(c\Delta t_0)^2 + ... \\ c\Delta t_2 &= c\Delta t_0(1 + R_{56}R_{65}) + R_{56}\delta_0 + T_{566}\delta_0^2 \\ &\quad +2T_{566}R_{65}\delta_0 c\Delta t_0 + (R_{56}T_{655} + T_{566}R_{65}^2)(c\Delta t_0)^2 \end{aligned}$$

For convenience let $\nu = 1 + R_{56}R_{65}$, $\psi = R_{56}T_{655} + T_{566}R_{65}^2$ and set $\delta_0 = 0$ to find the relative emittance change

$$\begin{aligned} \varepsilon_2^2 &= \langle (c\Delta t_2)^2\rangle\langle\delta_2^2\rangle - \langle c\Delta t_2\delta_2\rangle^2 \\ &= \langle(\nu c\Delta t_0 + \psi(c\Delta t_0)^2)^2\rangle\langle(R_{65}c\Delta t_0 + T_{655}(c\Delta t_0)^2)^2)\rangle \\ &\quad -\langle(\nu c\Delta t_0 + \psi(c\Delta t_0)^2)(R_{65}c\Delta t_0 + T_{655}(c\Delta t_0)^2)\rangle^2 \\ \varepsilon_2^2 &= \Big(\nu^2\langle(c\Delta t_0)^2\rangle + 2\nu\psi\langle(c\Delta t_0)^3\rangle + \psi^2\langle(c\Delta t_0)^4\rangle\Big)\cdot \\ &\quad \Big(R_{65}^2\langle(c\Delta t_0)^2\rangle + 2R_{65}T_{655}\langle(c\Delta t_0)^3\rangle + T_{655}^2\langle(c\Delta t_0)^4\rangle\Big) \\ &\quad -\langle\Big(\nu R_{65}(c\Delta t_0)^2 + (\nu T_{655} + \psi R_{65})(c\Delta t_0)^3 + T_{655}\psi(c\Delta t_0)^4\Big)\rangle^2 \end{aligned} \tag{6.7}$$

Finally through symmetry $\langle(c\Delta t_0)^3\rangle = 0$, gathering only 2$^{\text{nd}}$ order terms, and substituting in Eq. (6.5) and Eq. (6.6) the emittance can be approximated as

$$
\begin{aligned}
\varepsilon_2^2 &= \nu^2 R_{65}^2 \langle (c\Delta t_0)^2 \rangle^2 + \psi^2 R_{65}^2 \langle (c\Delta t_0)^4 \rangle \langle (c\Delta t_0)^2 \rangle \\
&\quad + \nu^2 T_{655}^2 \langle (c\Delta t_0)^2 \rangle \langle (c\Delta t_0)^4 \rangle + \psi^2 T_{655}^2 \langle (c\Delta t_0)^4 \rangle^2 \\
&\quad - \Big(\nu^2 R_{65}^2 \langle (c\Delta t_0)^2 \rangle^2 + 2\nu R_{65} T_{655} \psi \langle (c\Delta t_0)^2 \rangle \langle (c\Delta t_0)^4 \rangle + T_{655}^2 \psi^2 \langle (c\Delta t_0)^4 \rangle^2 \Big) \\
&= \langle (c\Delta t_0)^4 \rangle \langle (c\Delta t_0)^2 \rangle \big(\psi^2 R_{65}^2 + \nu^2 T_{655}^2 - 2\psi R_{65} T_{655} \nu \big) \\
&= \langle (c\Delta t_0)^4 \rangle \langle (c\Delta t_0)^2 \rangle \big(\psi R_{65} - \nu T_{655} \big)^2 \\
\varepsilon_2^2 &= < (c\Delta t_0)^4 >< (c\Delta t_0)^2 > \big(R_{65}(R_{56} T_{655} + T_{566} R_{65}^2) - (1 + R_{56} R_{65}) T_{655} \big)^2
\end{aligned}
$$

therefore

$$\varepsilon_2^2 = \langle (c\Delta t_0)^4 \rangle \langle (c\Delta t_0)^2 \rangle \big(T_{566} R_{65}^3 - T_{655} \big)^2 \tag{6.8}$$

One can interpret Eq. (6.8) as a useful tool to control the normalized emittance. The accelerating phase determines both the R_{65} and T_{655} terms and sextupole terms in the bend can manipulate T_{566} to compensate longitudinal emittance growth.

Fig. 6.13 demonstrates this concept, showing anticlockwise the variation of the beam phase space from an uncorrelated low emittance flat beam in red through a non-linear RF chirp in blue. Then the introduction of 1st and 2nd order magnetic correction, translating and deforming the phase space from green, magenta to black. Finally a second linac is used to approximately recover the original distribution given in cyan.

The proof-of-principle shown in Fig. 6.13 was implemented on the FSF optic. Finding the optimum settings to control the longitudinal emittance in the extensive FSF optic is an iterative process. To save on computational time, the next few figures shown in this subsection were produced with only a sample fraction of the original injector particle distribution and the radiation effects were partially restricted. Fig. 6.14 shows the longitudinal emittance recovery scheme adapted for the two stage telescopic bunch compression, the vertical axis is logarithmic, (where $\log 10^{-14}$ s $\rightarrow$ 10 fs). Using Eq. (6.7), the normalized longitudinal emittance

$$\varepsilon_{nz} = \gamma \, \varepsilon_z \tag{6.9}$$

shown as a black line, initially increases due to the RF curvature in the injector linac and then once again in the first split linac. The phase in each linac is tuned so that after the first arc, at

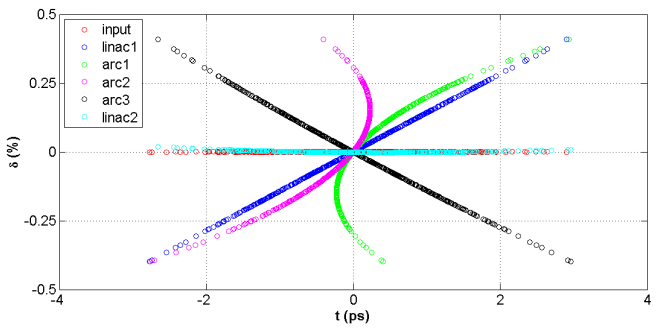

Figure 6.13: Proof-of-principle correction of the 2nd order aberrations.

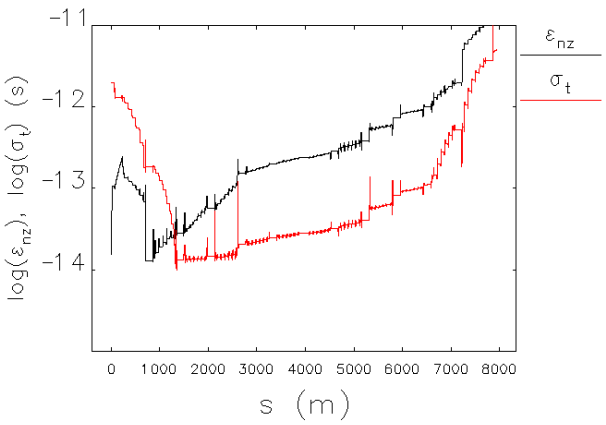

Figure 6.14: Longitudinal bunch properties along the FSF.

approximately $s = 700\,\text{m}$, the longitudinal emittance of the injected beam is fully recovered. This allows the full potential for further 2nd order compression in the following arc. The combination of the various T_{566} values in all the low energy arcs and their respective spreaders, are optimized for a given linac phase. The process is then reversed and iterative until both phase setting and arc optic are optimal to produce a final bunch length in red slightly less than 10 fs at 2 GeV. The arcs were continually adjusted so that their intrinsic higher order terms were compatible with the recovery scheme without using additional sextupoles. The normalized longitudinal emittance then increases without recovery ($s > 700\,\text{m}$) due to the coherent radiation effects associated with short bunches, producing the unwanted energy spread. The 10 fs bunch length at 2 GeV also increases to approximately 25 fs at the entrance to the long undulator section which is the half way point along the machine. The bunch is then actively decompressed in the lower energy stages on deceleration to help prepare the bunch for the beam dump.

After this 2nd order optimization process, the deviation in the parameters from the numerical estimations in previous subsection is only slight. The SPM parameters to produce the plot in Fig. 6.14 are $\phi_{1a} = 100.45^\circ$ and $\phi_{2a} = 69.00^\circ$ with $R_{56_1} = 20\,\text{cm}$ and $R_{56_2} = 8\,\text{cm}$. Only the longitudinal dispersion in the second arc was significantly changed in order to retain the telescopic compression qualities.

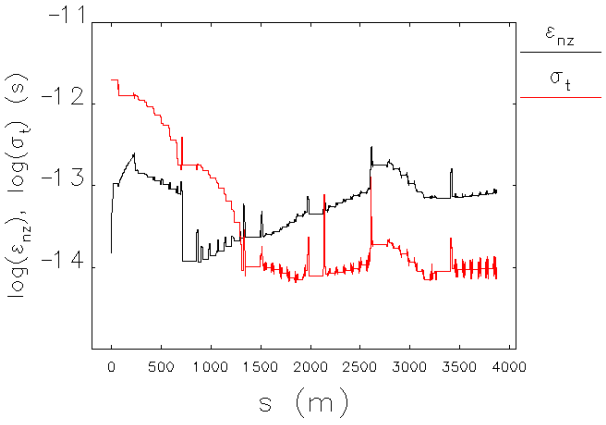

Figure 6.15: Additional 2nd order bunch compression in the high energy arcs using sextupoles.

One can also apply additional longitudinal gymnastics in the high energy arcs as shown in Fig. 6.15 to obtain 10 fs at 6 GeV. Additional sextupoles are implemented so that the increase in bunch length in the 4 GeV spreader (step at $s = 2500$ m) is re-compressed using 2$^{\text{nd}}$ order terms to replenish the 10 fs project goal at 6 GeV. However, the inclusion of such higher order magnets has a negative impact on the transversal emittance and realistic recovery is not possible at a bunch charge of 5 pC using the present spreader optic. A compromise is necessary as the spreader optic is common to both operation modes.

6.4.3 Start-to-end SPM Simulations

The results of the SPM start-to-end simulations shown in this section were undertaken as in the case of the LEM, with 100 000 particles and all relevant radiation effects accounted for. As previously discussed in Chapter 2, and more comprehensively investigated in Chapter 6.6, although a slight over approximation, the 1D CSR wake model in Elegant will suffice. Bunches of 1, 3 and 5 pC charge were successfully tracked through the full optic. The figures in this section are all taken for the 3 pC case, unless otherwise stated.

Fig. 6.16a shows in the blue dashed boxes, the asymmetric betatron functions in the low energy stages of acceleration and recovery. The Twiss-parameters in the arcs differ according to their longitudinal dispersion value. Bunch compression and decompression is achieved with positive and negative R_{56} values respectively. The maximum betatron value in both planes in all the arcs is less than 50 m. Again, as was the case for the LEM, the peaks are due to the spreaders and recombiners. The remaining linear optic in the high energy arcs is identical to the LEM.

Sextupoles are implemented into all spreaders and recombiners up to 3 GeV. This is necessary to suppress the dramatic growth in the vertical emittance when passing through these short but complex structures. The vertical beam size due to the T_{366} term became comparable with the geometric beam size as a relatively high energy spread is present in the SPM.

$$\sigma_{y,\text{geo}} \sim \sqrt{\varepsilon\beta} \sim 25\,\mu\text{m} \tag{6.10}$$

$$\sigma_{y,2^{\text{nd}}} \sim T_{366}\delta^2 \sim 14\,\mu\text{m} \tag{6.11}$$

The sextupoles were used to correct $T_{366} \to 0$ to allow for a safe passage through the spreaders. Additional care was taken not to significantly change the other 2$^{\text{nd}}$ order terms relevant for the longitudinal emittance recovery scheme such as T_{566}.

The additional energy spread due to the CSR wake dictates the trend of the transversal emittance plots shown in Fig. 6.16b. The non-linear energy correlation depending on the longitudinal bunch properties dominate this operational mode. This imprint is not seen in the LEM as it operates outside of this regime. For the SPM, the bunch length is less than 50 fs for the majority of the facility as shown in Fig. 6.17b.

Sextupoles are required in the final recovery arc to suppress the horizontal emittance growth due to chromatic aberrations. Without correction, the horizontal beam size becomes so large it spoils the other beam dimensions and causes substantial beam loss even before the dumpline when one assumes a vacuum chamber diameter of 40 mm. The technique derived analytically in Chapter 5.3 was implemented to ensure reasonable beam properties through the final deceleration stages. This tensor based method where $\Sigma_x \to 0$ is bunch charge independent and therefore optimization of large structures takes just seconds as particle tracking is not necessary. This method was benchmarked with the tracking alternative by setting the goal function of the optimizer to achieve minimal transverse

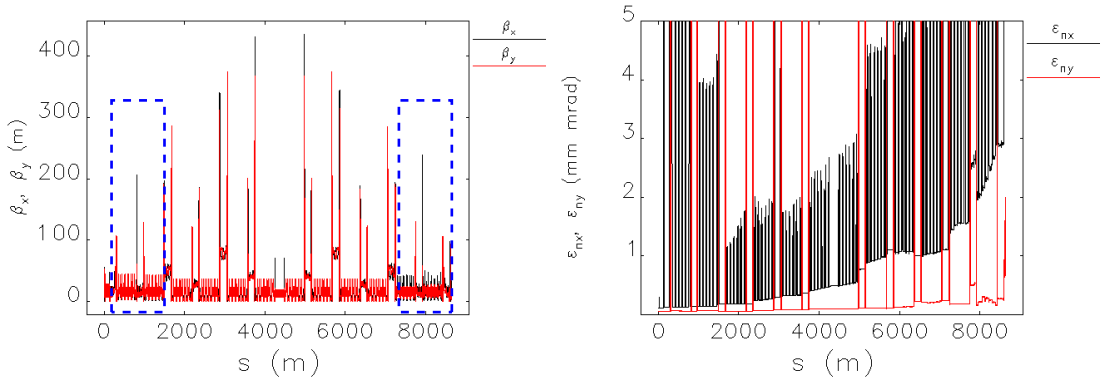

(a) Betatron functions along the FSF. (b) Transverse emittance growth along the FSF.

Figure 6.16: Transversal beam properties of the SPM.

emittance, $\varepsilon_{nx} \cdot \varepsilon_{nx} \rightarrow$ min. The later method relies heavily on the number of particles being tracked and the complexity of the optic. Even with staggered and iterative optimization the process is computationally expense. More importantly the Σ_x option produces equivalent results. Again the sextupole strengths were compared with Eq. (5.13) and found to be comfortably within the technical limits for the 1 GeV recovery arc.

The energy spread of the bunch for both the LEM and SPM are compared in Fig. 6.17a. The main difference occurs in the low energy ($s < 2$ km) stages of the facility where off-crest acceleration is required for the bunch compression in the SPM. At 6 GeV ($s \sim 4$ km), the energy spread of the LEM is at least a factor 5 lower than that of the SPM. At the dump, the values are both in the region of 10 % due to the fact that the LEM is tracked with considerably more bunch charge than the SPM.

The longitudinal bunch properties in Fig. 6.17b show the emittance recovery technique, comprehensively described in the previous section, used to good effect. As intended the longitudinal emittance ε_{nz} of the injected bunch is recovered during the bunch compression stages. With all relevant radiation effects simulated, the bunch length at 3 GeV is less than 10 fs and steadily increases to 25 fs at full energy. As already mentioned, other than the sextupoles in the spreaders and recombiners, no additional higher order magnets are required to produce compression in this elegant manner.

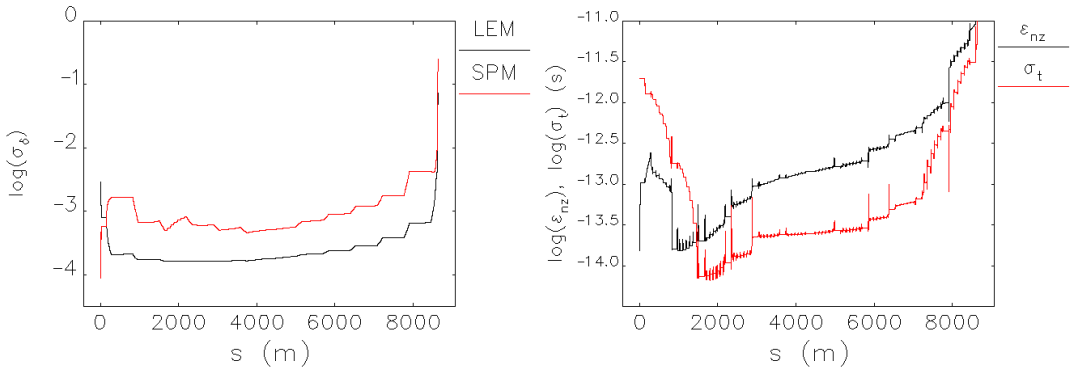

(a) Energy spread comparison for the two modes. (b) Longitudinal emittance and bunch compression.

Figure 6.17: Longitudinal beam properties of the FSF.

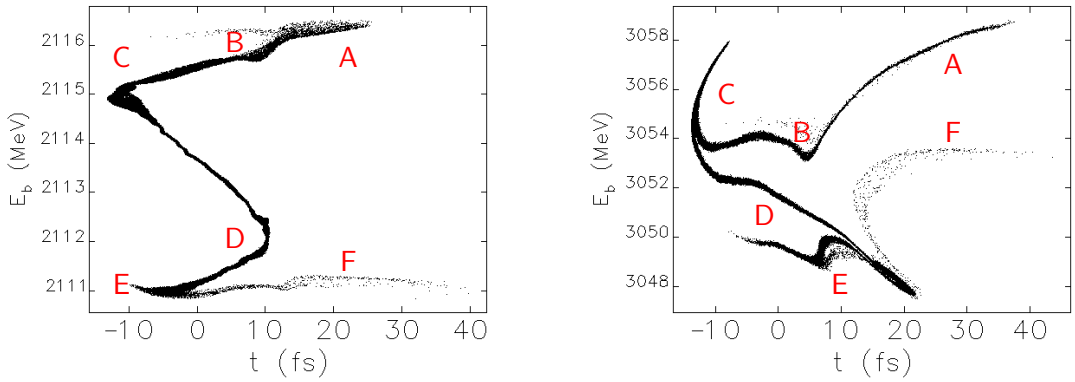

(a) 7 fs bunch length at 2 GeV.

(b) 10 fs bunch length at 3 GeV.

Figure 6.18: Longitudinal phase space evolution at the shortest bunch length watch points.

The evolution of the longitudinal phase space when the bunch length is in the order of 10 fs is shown in Fig. 6.18a and Fig. 6.18b from 2 to 3 GeV respectively. The progression of the watch points A to F show the effect of the bunch passing through the 3 GeV arc. The effect of the linac on the longitudinal particle coordinates is minimal since on acceleration $R_{56} \sim 1/(\beta\gamma)^2 \sim 0$. The CSR induced non-linear dynamics in the bending elements of the arc cause a folding of the bunch interior B $\rightarrow$ E and an extrusion to the outer extremities A and F. The elaborate nature of the particle evolution of the bunch is only feasibly possible to observe using particle tracking simulations.

The extruded extremities are shown in Fig. 6.19a to produce a 1 ps long tail from the 50 fs bunch interior. It is these outer, slightly higher energy particles that need particular attention during recovery. The extremities alter the bunch centroid which is used as a reference during the passage through a cavity. The extent of the bunch deceleration is sensitive to this centroid and the reference is internally chosen by the simulation program.

Fig. 6.19b shows that the relative number of particles in the tail is low at 3 GeV on recovery. As the energy of the bunch decreases through the low energy stages the absolute energy spread increases due to the RF curvature.

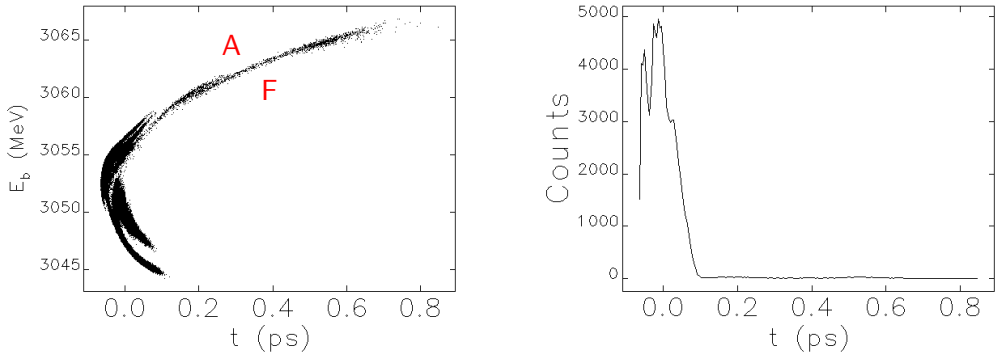

(a) Extrusion of bunch extremities.

(b) t projection of the particle distribution.

Figure 6.19: Longitudinal phase space on recovery.

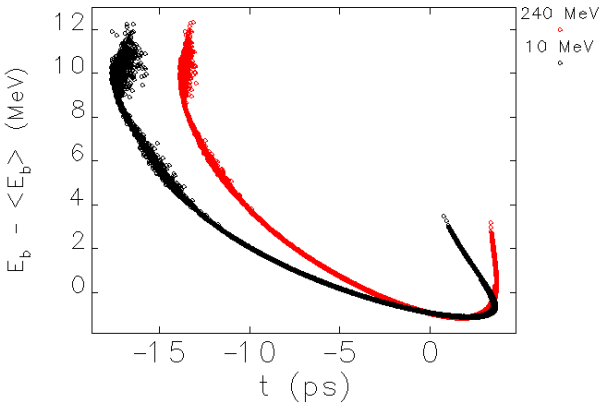

Figure 6.20: Comparison of the longitudinal phase space plots at the final stages of recovery.

Fig. 6.20 compares the longitudinal properties of the SPM bunch at 240 MeV and 10 MeV. The average beam energy is subtracted in both cases so that the plots overlap. The relative energy increases by the fraction of the deceleration to approximately 14 %. Without careful consideration, the fraction of particles with energies above the ±5 MeV acceptance may be lost in the dumpline.

Table 6.5 presents the results of the most relevant beam properties of the SPM start-to-end simulations. The input from the injector studies is successfully tracked through the 8 km optic to the dump. Even in this SPM, the electron beam properties up till the point of low energy on recovery remain admirable. Normalized emittances of 1 mm mrad combined with 50 fs bunch lengths is again beyond the capabilities of present 3rd generation facilities. The bunch length in the final stage of recovery compared to injection has doubled. This is instigated as a compromise to relax the transversal plane parameters in these critical sections of the machine.

Since the beam degradation due to the CSR wake is heavily dependent on the bunch charge, one can envisage lowering the charge of a given injector input until 10 fs at 6 GeV is reached without sextupoles in the higher energy arcs. Lowering the bunch charge addresses the impact of CSR but the damaging chromatic effects of the intricate spreaders due to the beams high energy spread in

Table 6.5: Start-to-end beam parameters for the 3 pC SPM.

Pos	ε_{nx} (mm mrad)	ε_{ny} (mm mrad)	σ_t (fs)	σ_E (10^{-3})	Energy (MeV)
Input	0.11	0.06	1990.09	0.46	50
Two stage injection	0.12	0.06	1281.99	0.57	240
Low energy arcs	0.18	0.06	7.39	0.71	2000
High energy arcs	0.30	0.08	22.59	0.62	4000
Undulator	0.49	0.10	24.73	0.52	6000
High energy arcs	1.00	0.23	48.70	0.92	4000
Low energy arcs	2.52	0.49	452.22	1.77	2000
Two stage recovery	8.47	0.93	3924.42	6.34	240
Dumpline	32.88	0.64	4430.29	14.66 %	10

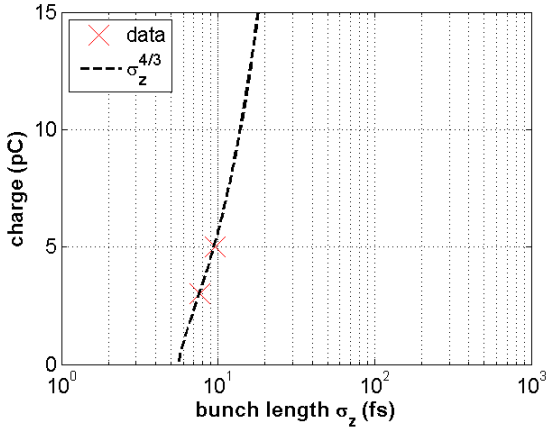

Figure 6.21: Boundary of minimum bunch length due to CSR effects for the FSF.

this operation mode still exist. One cannot freely optimize the spreaders higher order terms to cancel out this effect and achieve full compression. The beam clearly needs to be short but not at the cost of beam loss in another plane.

The expression for energy loss due to CSR derived in Chapter 2 for the rectangular bunch model can be reduced to the single particle equivalent as

$$\Delta E_{\text{CSR}} \sim q/\left(\sigma_t^2 - \sigma_0^2\right)^{2/3} \sim \text{const} \tag{6.12}$$

where σ_0 is the zero-charge bunch length. Particle tracking simulation results with both the 3 and 5 pC bunches show the SPM to be dominated by CSR effects. Intricate 2$^{\text{nd}}$ order optic is used on recovery to ensure that the energy spread of these two bunch charges at the dump are similar. If one assumes that these settings represent the 'limit' for any given bunch charge, then the zero-charge bunch length at 2 GeV is

$$\begin{aligned} 5\,[\text{pC}] &= C_1(9.6\,[\text{fs}]^2 - \sigma_0^2)^{2/3} \\ 3\,[\text{pC}] &= C_1(7.6\,[\text{fs}]^2 - \sigma_0^2)^{2/3} \end{aligned}$$

$$\sigma_0 = 5.6\,\text{fs}$$

The results can be extrapolated to form a boundary of the minimum bunch length for a given charge as shown in Fig. 6.21. Bunch charges and lengths to the left of the boundary are not feasible, the distortion due to CSR will be too large to recover the beam at 10 MeV. To the right of the boundary all settings are possible. The upper charge boundary of 15 pC is the limit from the injector studies and the 1 ps long bunch extremity on the far right hand of the figure is due to the RF curvature in the linac. Notably the LEM would exist in the top right hand corner of Fig. 6.21, suggesting that the operation mode is well above the CSR limit and bunch compression is possible if it is beneficial for the light source. More analysis of these mode settings with regards to their spectral properties is investigated in Chapter 6.5. The energy loss due to radiation is not to be underestimated and the following section reports on the extent of the recuperation that is required in order to safely dump at 10 MeV.

6.4.4 Energy Loss due to Radiation

It is envisaged that the energy loss due to radiation in the arcs alone will exceed the original 10 MeV injection energy of the FSF. This section describes an energy loss budget for the different sources of radiation induced energy loss. Common to both modes, the energy loss due to ISR [19] in the 6 GeV turn

$$E_{\mathrm{TURN}}\,[\mathrm{MeV}] = 0.0886 \cdot E_{\mathrm{b}}^{4}\,[\mathrm{GeV}] \,/\, \rho\,[\mathrm{m}] \tag{6.13}$$

is in the order of 8 MeV. In a similar manner, the energy loss due to the abundance of undulators can be calculated using

$$E_{\mathrm{u}}\,[\mathrm{keV}] = 0.633 \cdot E_{\mathrm{b}}^{2}\,[\mathrm{GeV}]\, B^{2}[\mathrm{T}]\, L_{\mathrm{u}}[\mathrm{m}] \tag{6.14}$$

where L_{u} is the total undulator length per arc. Given that there are five sections each 40 m long between the 30 ° periodic bends and using the undulator parameters from Chapter 6.5 (Table 6.7), this amounts to an energy loss of 4 MeV in the 6 GeV turn.

The CSR contribution in the LEM is negligible compared to that of the SPM. The amount of energy loss due to CSR taken from the results of the particle tracking simulations is shown in Fig. 6.22 for a 5 pC bunch charge in the SPM. The large contribution from CSR at 3 GeV is in keeping with the shorter bunch lengths, seen as the light blue line. The shortest bunch is created after the 2 GeV arc and hence the CSR effect is most dominant in the following 3 GeV arc. The bunch length in the final two high energy arcs is relatively stable and accordingly shows similar CSR proportions. Again Eq. (2.30) for a rectangular bunch model can be used to verify the total CSR contribution. For the 5 pC bunch the total energy loss would be approximately 20 MeV which is in good agreement with the particle tracking results.

Booster modules were implemented in the simulations to compensate for this energy loss due to radiation. These modules operate without energy recovery and require approximately 300 kW and 200 kW of total power for the LEM and SPM respectively. The location and peak voltage of these modules were studied in order to optimize their effectiveness. For the SPM one would require a minimum of eight modules, shared between acceleration and deceleration, located after each (3 $\rightarrow$ 6 GeV and 6 $\rightarrow$ 3 GeV) high energy arc in the beamline before their respective spreaders. The boosters were optimized to keep the mean energy of the bunch to $\pm$ 100 keV of the reference particle defined by Elegant. The nature of the recovery optic in the next section will not significantly change the amount of energy to be recuperated due to radiation loss but could lower the relative energy spread of the bunch and help for a safer passage to the dump.

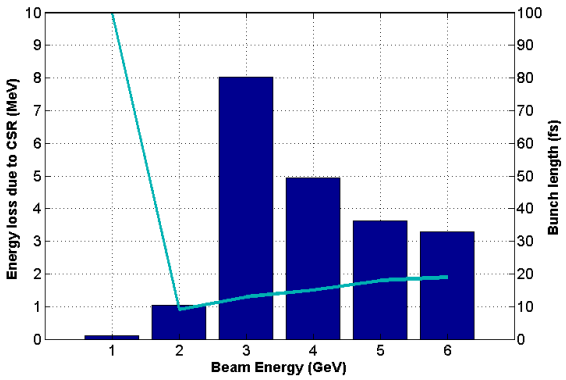

Figure 6.22: Energy loss due to CSR for the 5 pC SPM on acceleration.

6.4.5 Recovery Modes

The standard recovery mode described in Chapter 6.4.1 depicts a symmetric acceleration and deceleration. The deceleration phase ϕ_{d} is chosen half a period later than the acceleration phase ϕ_{a} and the return arcs have negative longitudinal dispersion values. Theoretically possible is another option whereby the phase is chosen on the opposite side of the RF cycle at the same absolute amplitude and the arc R_{56} value remains positive as given in Table 6.6.

Fig. 6.23 shows the tracking simulations without radiation effects for the two options given in Table 6.6. The average momentum is subtracted in both cases. Fig. 6.23a shows the standard telescopic compression during acceleration (red, light blue, green) in the first two arcs up to a beam energy of 2 GeV using off-crest acceleration $\phi_{1\mathrm{a}} = +100\,^\circ$, $\phi_{2\mathrm{a}} = 70\,^\circ$ and positive R_{56} values in both arcs. Also shown is the symmetric deceleration (orange, dark blue, black) from 2 GeV back to the injector by setting $\phi_{1\mathrm{d}} = \phi_{1\mathrm{a}} + 180\,^\circ$ so that $\phi_{1\mathrm{d}} = 280\,^\circ$, $\phi_{2\mathrm{d}} = 230\,^\circ$ and creating optic with negative R_{56} values.

Whereas Fig. 6.23b shows the alternative option $\phi_{\mathrm{d}} = 360\,^\circ - \phi_{\mathrm{a}}$ so that $\phi_{1\mathrm{d}} = 260\,^\circ$, $\phi_{2\mathrm{d}} = 290\,^\circ$ and using the same positive R_{56} optic as for acceleration. The colour code is the same as described in the standard option. In this alternative mode the translation of the phase space differs so that a full 180 ° turn is produced since all arcs have positive R_{56}. The correlated energy spread due to RF curvature is almost fully removed by the asymmetric deceleration. As previously described sextupoles are used in the SPM to induce bunch compression, reduce chromatic aberrations and suppress transversal emittance growth. The iterative inclusion of sextupoles to aid beam transport in various stages has unfortunately not actively corrected for the imprint of the RF curvature in the standard recovery option. One can envisage either a revised investigation of the present sextupole settings, or implementing additional magnets or applying the alternative recovery approach.

Table 6.6: Linac and arc properties for the FSF recovery options.

	Standard	Alternative
Phase	$\phi_{\mathrm{d}} = \phi_{\mathrm{a}} + 180\,^\circ$	$\phi_{\mathrm{d}} = 360\,^\circ - \phi_{\mathrm{a}}$
Arc	$R_{56_{\mathrm{d}}} = -R_{56_{\mathrm{a}}}$	$R_{56_{\mathrm{d}}} = R_{56_{\mathrm{a}}}$

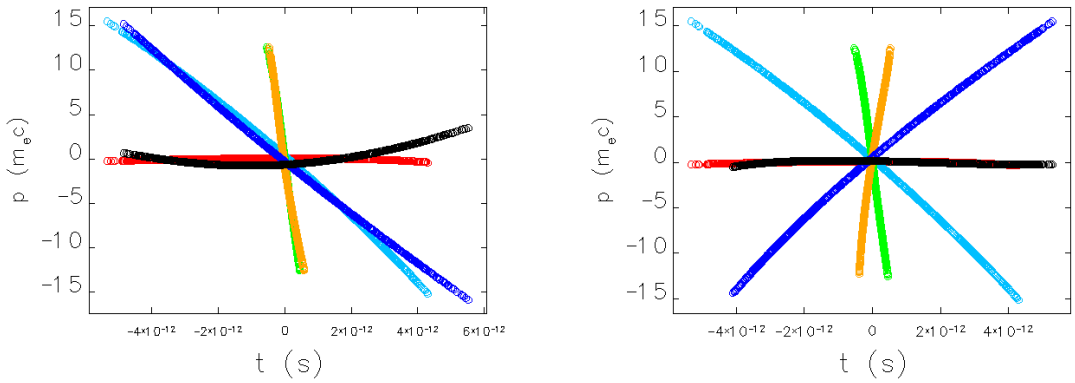

(a) $\phi_{\mathrm{d}} = \phi_{\mathrm{a}} + 180\,^\circ$

(b) $\phi_{\mathrm{d}} = 360\,^\circ - \phi_{\mathrm{a}}$

Figure 6.23: Longitudinal phase space plots for the SPM recovery options.

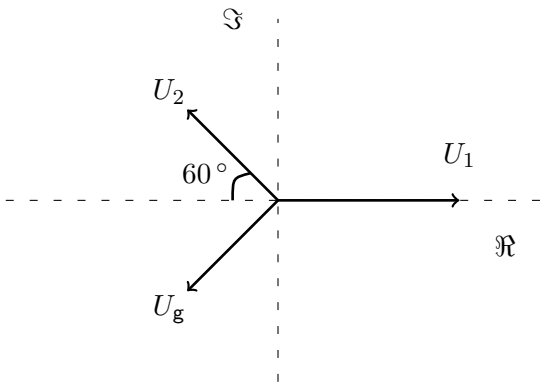

Figure 6.24: Complex phasor diagram for the alternative recovery mode.

Simulation results without radiation effects show the potential reduction of energy spread using the alternative recovery option to be in the order of a factor 15. However, when both the radiation effects and full start-to-end optic for FSF are simulated the potential lowers to a factor 4. As studied in Chapter 5, the distinct energy correlation due to radiation effects can not be so readily removed.

A factor 4 however, may still be a sufficient incentive to include such an option in the FSF but the additional workload due to the phase shift needs to be accounted for. In the standard option the recovery beam is offset by $180\,^\circ$. This means that the fields induced by the accelerating bunch U_1 are fully compensated for by the decelerating bunch U_2 and the generator U_g has no extra work. The phase shift used in Fig. 6.23b between the two recovery modes is $\Delta\phi_{2\mathrm{d}} = 230\,^\circ \rightarrow 290\,^\circ = 60\,^\circ$. This shift causes a load on the generator as shown in Fig. 6.24. Cavities are designed so that there is no resonance of modes which are a multiple of the driving frequency. However the fields caused by the imbalance $U_\mathrm{g} = U_2 \cos(60)$ need to be outcoupled and compensated for by the generator.

Presently couplers associated with SRF technology are limited to 100 kW power through the RF window. Taking the FSF SPM beam parameters, the supplementary workload for the generator at 1.3 GHz would be $P_\mathrm{g} = 5\,\mathrm{mA} \cdot 15\,\mathrm{MeV} = 75\,\mathrm{kW}$. Although the coupler would in this case be adequate, often the typical SRF 7-cell ERL cryomodule is limited to a mere 10 kW therefore a more powerful and expensive generator would be necessary. A compromise between available power and beam dynamics is required. The alternative option is intended to be used in the fourth turn of the NovoFEL described in Chapter 4. The normal conducting RF linac operates at a lower frequency of 180 MHz and the cavity and coupler window are accordingly larger. Even with the foreseen upgrades to 100 mA beam current the additional load will be manageable since the generator is capable of 1 MW power.

With this subsection the dedicated study of the SPM comes to a close. It has introduced the general facility layout and the magnetic constraints incorporated from the LEM. A compression scheme using the low energy sections of the FSF optic was presented. The dominance of the CSR effect is clear. An energy loss budget is given and a recuperation scheme using booster cavities is proposed. The alternative recovery mode has a great potential to aid beam dynamics but has been found to lie on the limit of technically feasible for SRF based light sources. The following sections present the expectations of the spectral properties of the light source, first with respect to generating incoherent radiation then the greater potential of coherent light from the FSF.

6.5 Spectral Properties of the FSF Light Source

Permanent magnetic undulators are considered throughout the FSF as the source of high brilliance photon radiation. The electron beam energy γ, undulator parameter K and undulator period length λ_u are used to define the radiation wavelength λ_{ph} of the emitted photons as

$$\lambda_{ph} = \frac{\lambda_u}{2\gamma^2}\left(1 + \frac{K^2}{2}\right) \tag{6.15}$$

Simulations using many undulators over an 8 km long optic can become computationally expensive and time consuming. Initially the undulators were approximated as drift elements as the vertical focusing $k_y = 1/(2\rho^2) \sim 1/\gamma^2$ can be neglected at high energies.

The brilliance (often referred to in literature as the spectral brightness) is a measure of the photon density in 6D space created by the electron beam. The brilliance is reduced from the mono-energetic diffraction limit since betatron motion in the undulators exists and the photon beam has an apparent source size $\sigma \cdot \sigma'$ and energy spread $d\omega/\omega$ due the electron beam properties. Therefore full coherence is never achieved. For m harmonics one can equate the average brilliance as

$$\langle B \rangle = \frac{\dot{N}_{ph}}{4\pi^2 \sigma_x \sigma'_x \sigma_y \sigma'_y (d\omega/\omega)} \left[\frac{1}{1 + (4\sqrt{2}\, m N_u \sigma_E)^2}\right]^{1/2} \tag{6.16}$$

where the term in the square brackets is the increased spectral width of the radiation due to energy spread. The $4\sqrt{2}$ term is taken from the WAVE [51] simulation program for insertion device performance calculations. Table 6.7 gives the common parameters for the undulators in the arcs which are $N_u = 1000$ periods long. Plotted in Fig. 6.25 is the expected average brilliance of the synchrotron radiation from the LEM for the first few m harmonics at a beam current of 20 mA.

The LEM goal parameter of $\varepsilon_n \sim 0.1$ mm mrad produces a magnitude larger average brilliance than the present world leading light source SPring-8 in Japan [52]. When one considers only the average

Table 6.7: Typical undulator parameters.

λ_u (cm)	K	B_{max} (T)	$\langle B \rangle$ at 6 GeV (N_{ph}/s/mrad^2/mm^2/0.1 %BW)
4	0 - 2.5	0.67	$4{\cdot}10^{22}$

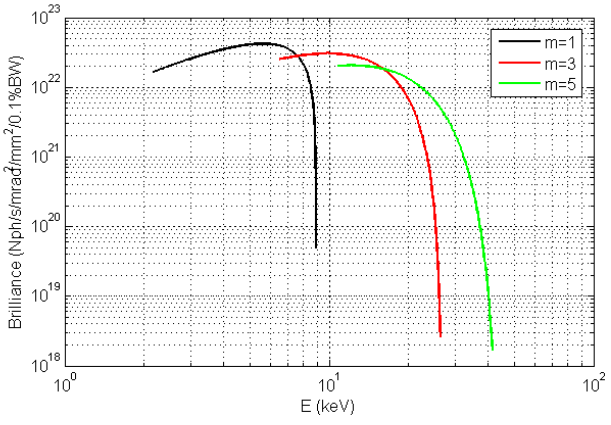

Figure 6.25: Average brilliance curves from the undulators in the 6 GeV arc in the LEM.

brilliance, that is the amount of photons per second not bunch, then the bunch length of the LEM is in some respects irrelevant. However in order for the FSF to offer what 3rd generation light sources can not, a bunch length of 2 ps is chosen. This value is far beyond the CSR limit described previously in Fig. 6.21 and at this bunch length RF curvature will not significantly increase the longitudinal emittance. One can estimate this bunch length upper limit using $\sigma_t \sim \lambda_{\mathsf{RF}} / (c\sqrt{N_{\mathsf{u}}})$ to be in the order of tens of ps.

In the SPM, the strict transversal properties are then sacrificed to achieve fs bunch lengths and maximum peak brilliance B_{p}. The largest value of brilliance is a correct balance between low transversal emittance and relatively short bunch lengths.

For the peak brilliance one needs to consider the 6D phase space of the emitted photons. The bunch length is then extremely relevant in this case and the radiation associated with Eq. (6.16) needs to be considered per bunch rather than second. The power density of the emitted photons becomes equivalent to the brilliance of the electron beam

$$B_{\mathsf{p}} = \frac{N_{\mathsf{ph}}}{(2\pi)^2 \varepsilon_x \varepsilon_y \varepsilon_z} \equiv \frac{q\, C_\gamma}{(2\pi)^2 \varepsilon_x \varepsilon_y \varepsilon_z} \tag{6.17}$$

where C_γ is the number of photons emitted per electron and q is the bunch charge. Eq. (6.14) describing the power of the emitted photons (the energy loss of the bunch) and the radiation wavelength defined by Eq. (6.15) can be used to approximate C_γ as 50 photons emitted per electron in the long undulator section at 6 GeV. Fig. 6.26 highlights the necessity of optimizing for the minimum emittance in all planes. The SPM compression scheme uses only the low energy arcs and full compression is achieved at 2 GeV. The 5 pC bunch is the highest of the first peaks at $s \sim 1$ km as the bunch lengths of all three charges are approximately 10 fs. The trend that follows is due to the extent of the CSR induced transversal beam degradation and bunch lengthening. The next peaks at 3 GeV show both the 3 and 5 pC bunches emitting similar peak brilliance. Then as the transversal emittance growth establishes itself in the high energy arcs, the brilliance of the higher charged beams falls away. At 6 GeV, (largest peak at $s \sim 4$ km) the light source produces most brilliance for lower charges. Also at 6 GeV one sees a similar fall in peak brilliance for all charges over the final high energy turn due to the ISR induced emittance growth Eq. (6.3) that is heavily dependent on beam energy $\Delta\varepsilon_{\mathsf{n,ISR}} \sim E_{\mathsf{b}}^6$.

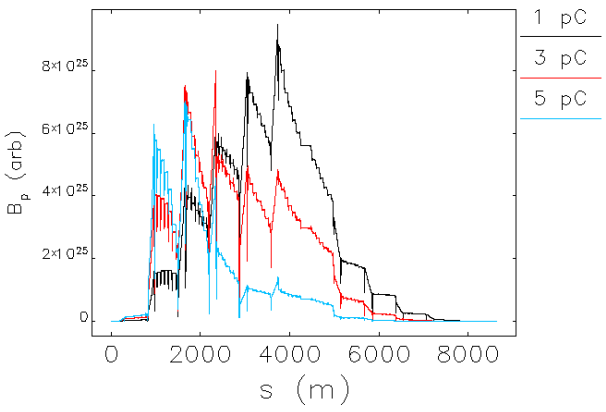

Figure 6.26: Peak brilliance curves throughout the FSF for various bunch charges of the SPM.

If bunch compression was possible in all arcs, the highest peak for a given charge could be engineered to suit the user using a staggered compression scheme. Unfortunately the SPM is not the primary mode of the light source and restrictions on the optic exist.

Assuming a Gaussian photon source [53] in the transverse plane then the coherent fraction P_c is given by

$$P_{\mathrm{c}} = \frac{\lambda_{\mathrm{ph}}^{2}}{(4\pi)^2 \varepsilon_x \varepsilon_y} \tag{6.18}$$

which amounts to $P_{\mathrm{c}} = 0.5$ at 12.3 keV for the FSF beam parameters given in Table 6.4. Other distributions of the radiation source are considered in [54]. The apparent size of the radiation source σ_x is a combination of the photon beam σ_γ, the geometric emittance and dispersive contribution of the electron beam plus other higher orders.

$$\sigma_x = \sqrt{\frac{\sigma_\gamma^2}{2} + \varepsilon\beta + \left(\eta\delta\right)^2 + \ldots} \tag{6.19}$$

For a constant source size $\Delta\sigma_x = 0$ and neglecting the photon dimension the geometric and dispersive components of the electron beam may at worst become comparable. This implies the dispersion

$$\eta \ll \frac{\sqrt{\varepsilon\beta}}{\sigma_{_E}} \sim 10^{-3}\,\mathrm{m} \tag{6.20}$$

needs to be sub mm in the insertion device regions or it will play an unwanted role in the apparent source size of the radiation. An estimation of the emittance growth due to ISR in an undulator with non-zero dispersion using Eq. (6.2) gives a similar result. Hence the brightest light available depends strongly on the closed dispersion.

Fig. 6.27 shows the slow extrusion of the vertical dispersion over the 8 km machine when the dispersion is not actively closed. The dispersion in the arcs are theoretically closed in the simulations to below 10^{-8} m but the complexity in the spreaders and recombiners show that the dispersion starts to peculate and evolve. A similar evolution is present in the horizontal trajectory but both transversal planes stay below the critical sub mm value needed for high brilliance radiation in the undulator sections. Experimental procedures like those described in Chapter 4.1.2 where BPMs were used to find the difference in beam position as the quadrupole settings were scanned will be needed at each stage in the FSF to help close the unwanted dispersion leak.

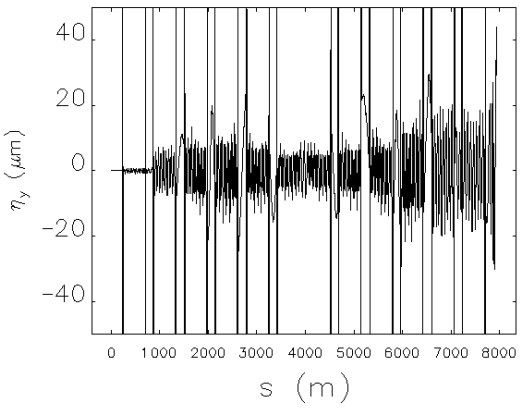

Figure 6.27: Evolution of the vertical dispersion growth across the FSF.

6.6 FSF Free Electron Laser Studies

This section investigates if a Free Electron Laser (FEL) is theoretically possible using the beam parameters from the FSF short pulse mode. During the FEL process, the interaction between the electron beam and the radiation field inside an undulator leads to an energy modulation along the bunch. This energy modulation is coherent for electrons whose energy is near the FEL resonance energy given by the undulator parameters. The energy modulation produces a density modulation (micro-bunching) which in turn causes coherent emission and amplification of the energy modulation. This collective lasing interaction can produce GW X-ray radiation power. Such high gain, single pass FELs require large peak currents to initiate the Self Amplified Spontaneous Emission (SASE) of radiation without the need of external seeding. The present FLASH FEL [55] parameters of a sub ps long, nC bunch generates more than a kA of peak current.

Lasing however induces a slice dependent energy loss and a measurable energy spread footprint on the electron beams longitudinal phase space [56]. These losses will play a critical role in the efficiency of the ERL process in the deceleration turns.

Table 6.8 gives the beam parameters at various stages during the acceleration for the SPM. The horizontal geometric emittance values indicate that emittance reduction due to adiabatic damping is almost equivalent to the growth caused by radiation effects for the SPM. Also given in the final column is the condition for the diffraction limited emittance with undulator parameters $K = 1$ and $\lambda_{\mathsf{u}} = 4\,\mathsf{cm}$ using

$$\varepsilon_{\mathsf{limit}} < \frac{\lambda_{\mathsf{ph}}}{4\pi} \tag{6.21}$$

The vertical emittance remains below the diffraction limit value in the FSF but as the energy increases the horizontal emittance becomes first comparable then high beyond the limit. The bunch charge was set to 5 pC and the highlighted result in green would suggest a peak current of $\sim 5\,\mathsf{pC}\,/\,10\,\mathsf{fs} = 500\,\mathsf{A}$. This is the best suited result with the shortest bunch length and technically the most convenient arc. At this position in the light source, one could simply modify the optic in the 2 GeV vertical spreader and transport the beam straight into the long undulator section rather than continuing to accelerate to higher energies. Once the FEL process is completed in the long undulators the bunch would then be symmetrically decelerated and recovered. This third operation mode (FELM) is complementary to the existing LEM and SPM as only minor modifications to the 2 GeV turn are required.

Table 6.8: FSF beam parameters for the 5 pC SPM on acceleration.

Energy (GeV)	$\varepsilon_x \cdot 10^{-11}$ (m rad)	$\varepsilon_y \cdot 10^{-11}$ (m rad)	σ_t (fs)	σ_E (10^{-3})	$\varepsilon_{\mathsf{limit}} \cdot 10^{-11}$ (m rad)
1	4.65	2.73	185.0	1.68	59.7
2	3.70	1.65	11.45	0.68	14.9
3	3.70	1.16	25.03	1.00	6.63
4	4.18	0.92	31.27	0.71	3.73
5	4.12	0.76	32.05	0.66	2.39
6	4.26	0.97	31.71	0.65	1.66

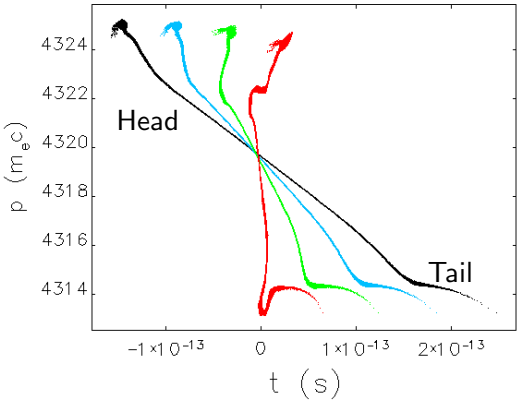

Figure 6.28: Phase space plots in the final bend of the 2 GeV arc.

Fig. 6.28 shows the evolution of the longitudinal phase space in the final few TBA cells in the 2 GeV arc where the bunch length is reduced from 100 $\rightarrow$ 10 fs, black to red dots respectively. As expected from the CSR theory of a bunch passing through a bend in Chapter 2, emission from the tail interacts with the head producing an energy modulation along the bunch. This non-linear wake is clearly visible in the distributions and becomes more apparent as the bunch is fully compressed. Also as expected the head loses energy as the CSR wake evolves. As a result, the horizontal emittance (not shown) increases by a factor of two during this final stage as particles receive a CSR kick along the bending path, see Chapter 5. The 1D CSR model used in the simulations is an approximation since the 3D distribution is projected on a single axis. The characteristic transverse distance L_t from the two electron CSR model geometry depicted in Fig. 2.8 can be used to validate this model.

$$L_t = 2(9\sigma_z^2\rho)^{1/3}$$

Considering the 2 GeV bunch parameters with a bending radius $\rho = 6.667$ m the transverse distance is $L_t = 1.6$ mm. Comparing this value with the geometrical beam size $\sigma_x^2 = \varepsilon\beta$ and the vacuum chamber diameter D one finds $\sigma_x \ll L_t < D$ hence a 1D model without shielding should suffice.

The SASE FEL condition is commonly described by the Pierce parameter as

$$\rho_{\mathsf{p}} = \left(\frac{1}{16}\,\frac{I_{\mathsf{peak}}}{I_{\mathsf{A}}}\,\frac{K^2}{\sigma_x^2}\,\frac{\lambda_{\mathsf{u}}^2}{(2\pi)^2}\,\frac{[JJ]^2}{\gamma^3}\right)^{1/3} \tag{6.22}$$

In general, the energy spread of the beam prior to SASE should be smaller than the Pierce parameter in order to induce lasing. Here the Bessel function factor is given by $[JJ] = J_0(K^2/(4+2K^2) - J_1(K^2/(4+2K^2)$ and I_{A} is the Alfvén current. The Pierce parameter is typically $\sim 0.1\,\%$. In order to find a suitable value for I_{peak} at 2 GeV the red dotted particle distribution was binned using

$$I = \frac{q}{N_e}\left(\frac{\mathsf{Counts}\cdot c}{\mathsf{Bin}}\right) \tag{6.23}$$

and plotted as a histogram in Fig. 6.29. Taking the value of the apparent peak, one could conclude that $I_{\mathsf{peak}} = 700$ A. At this stage in the study, this estimation for the peak current is questionable and one should note that the slippage length $\sim N_{\mathsf{u}}\,/\,\lambda_{\mathsf{ph}} \sim 24\,\mu$m is large compared to the peaks in current. To make a more reasonable valuation the beam parameters from the particle tracking

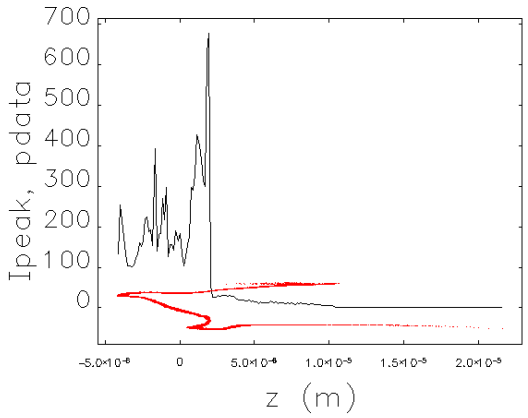

Figure 6.29: Current density profile and longitudinal phase space plot of the SPM at 2 GeV.

simulations were implemented into an analytical approximation based on [57]. Here, a fitting formula is used to predict the power gain length of the fundamental mode L_{G0} and a degradation factor Λ given by

$$L_G = L_{G0}\Big(1 + \Lambda\Big) \tag{6.24}$$

and estimate the saturation power as

$$P_{sat}[\text{GW}] = 1.6\ \rho_p\ P_b[\text{GW}]\Big/(1+\Lambda)^2 \tag{6.25}$$

Table 6.9 summarizes the results from the fitting parameter. GW saturation power is associated with $I_{peak} = 700$ A whereas many MW of power is possible with lower peak current values. The saturation length of the FEL process is in the order of 20 m when $I_{peak} \sim 700$ A.

The analytical formula taken so far on the SPM beam parameters at 2 GeV all suggest the FEL process is plausible. The saturation length predicted is low enough to induce the FEL process in the short undulator sections within the arc. These undulator structures are plentiful and highlights the danger associated with longitudinal beam degradation due to increased energy spread from an unwanted FEL process. The bending cells within the arcs will smother out the micro-bunching on a nm scale due to the non-isochronous nature of the higher order optic but the process may re-establish itself in the following undulator section.

In order to help resolve this issue of which I_{peak} is valid, the beam distribution was taken from Elegant and imported into Genesis [58]. The time-dependent FEL code tracks macro-particles that represent the beam in 3D. Fig. 6.30 shows the SASE radiation power of a slice of the beam from the head of the bunch as it traverses the FSF long undulator section. The figure also shows a saturation length

Table 6.9: Expectations of the FELM at 2 GeV.

I_{peak} (A)	ρ_p 10^{-3}	L_{G0} (m)	Λ	P_{sat} (GW)	L_G (m)	L_{sat} $20L_G$ (m)
100	1.40	1.30	2.75	0.03	4.89	100
400	2.23	0.82	0.86	0.83	1.53	30
700	2.70	0.68	0.62	2.29	1.11	20

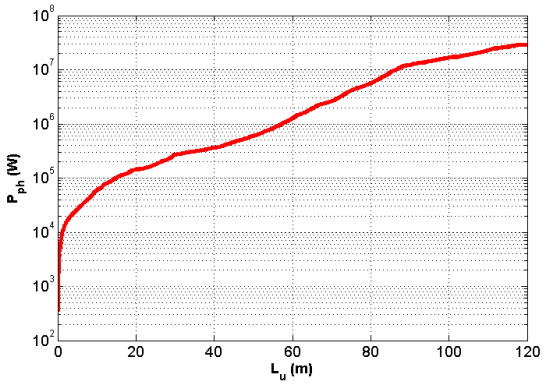

Figure 6.30: FEL radiation power of a single bunch slice along the long undulator section.

of over 100 m suggesting from Table 6.9 that $I_{\text{peak}} \sim 100$ A. In this case the FEL process would not come to saturation; the point at which the beams energy spread grows exponentially, within the short undulator sections in the arcs. However, the FEL process would materialize in the long undulator section to produce 20 MW of sliced radiation power.

The energy spread of each beam slice before and after the undulator section are plotted in Fig. 6.31a. A migration of the energy correctly exists causing an energy modulation of the head (slices > 300). Fig. 6.31b shows the power spectrum about the resonant wavelength. In the diffraction limit the apparent size of the photon beam can be approximated as $\sigma_\gamma^2 \sim \lambda_{\text{ph}} L$. If L is taken as the worst case scenario, as total the length of the undulator section L_{u} then $\sigma_\gamma \sim 1$ mm.

Working with the large output particle distribution from GENESIS is cumbersome and a third party program is required. Making the three assumptions: that the longitudinal position of the electrons will not have changed, only their energy variation and that the radiation wavelength is much shorter than the bunch length, one could use a GENESIS output file to construct an input file for Elegant for one particle per slice and continue tracking on the deceleration side of the FSF optic. However, for the example shown in Fig. 6.31a it is only the bunch head that is energy modulated to any great extent. The bunching factor in the slices of the head reach 33 % on saturation and in the tail are practically none existent. Even though 20 MW of sliced bunched power is generated the rms bunch energy spread remains relatively constant in this one particle per slice approximation. Generating such a file for Elegant from the slice properties shows that the new quasi-bunch could be safely

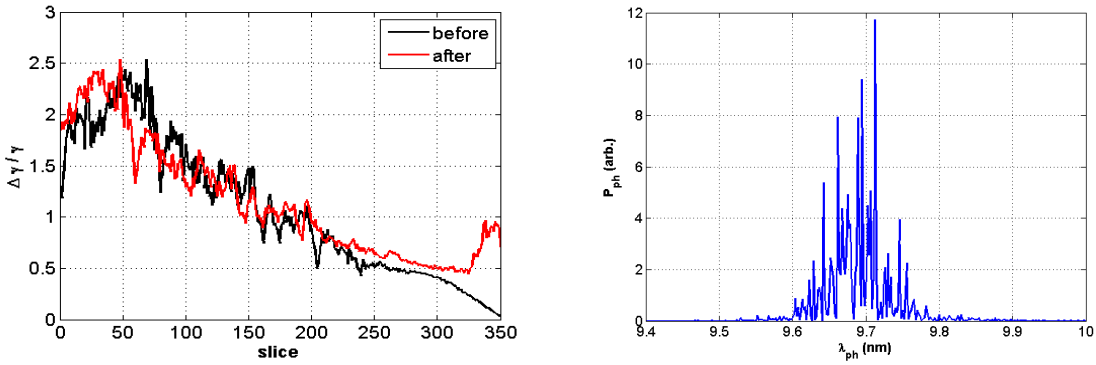

(a) FEL energy modulation from the tail to head.

(b) Radiation spectrum at the exit of the FEL section.

Figure 6.31: Energy transfer and spectral properties associated with the FEL process.

transported back the dump line with an energy spread of $\sigma_E = 2.4 \cdot 10^{-3}$.

Dedicated investigations outside the scope of this thesis are required to establish an automated procedure to run ASTRA, Elegant and GENESIS simulations in a batch for optimization. The results of the injector space charge dominated studies such as those given in Chapter 6.2 would be input into the 4 km multi-turn optic in Elegant and tracked to the FEL section. The output is then exported into GENESIS and used to simulate the FEL process. The full particle distributions need to then be imported again into Elegant and tracked through the 4 km of recovery optic to the dump. The scale of such a study is non-trivial and other less elaborate schemes may suffice. This batched suggestion unfortunately incorporates three very different programs all of which are computational expensive when 100 000 particles and all relevant effects are simulated. The necessity of such a large scale study still remains in order to produce bunch slices that generate coherent light with a power $P_{\text{sat}} > 20\,\text{MW}$.

In order to continue, the resilience of the start-to-end simulations to a FEL like process is investigated. The undulators were replaced with laser heater (LH) elements as introduced in Chapter 6.2, to induce a FEL like energy modulation along the whole bunch. The value of the theoretical laser power was increased until the rms energy spread of the bunch approximately doubled as shown in Fig. 6.32b at $s \sim 1250\,\text{m}$. This distorted bunch was then successfully tracked back to the dump. A final energy spread of $\sigma_E = 1.2\,\%$ at 50 MeV in the dumpline is given in Table 6.10. This value is comparable to both the LEM and SPM where the beam is tracked further and dumped at 10 MeV.

Table 6.10: Start-to-end beam parameters for the 5 pC FELM.

Pos	ε_{nx} (mm mrad)	ε_{ny} (mm mrad)	σ_t (fs)	σ_E (10^{-3})	Energy (MeV)
Injection	0.11	0.06	1990	0.48	50
before LH	0.13	0.07	7.87	0.70	2000
after LH	0.13	0.07	8.10	1.25	2000
Dumpline	0.31	0.19	2775	12.40	50

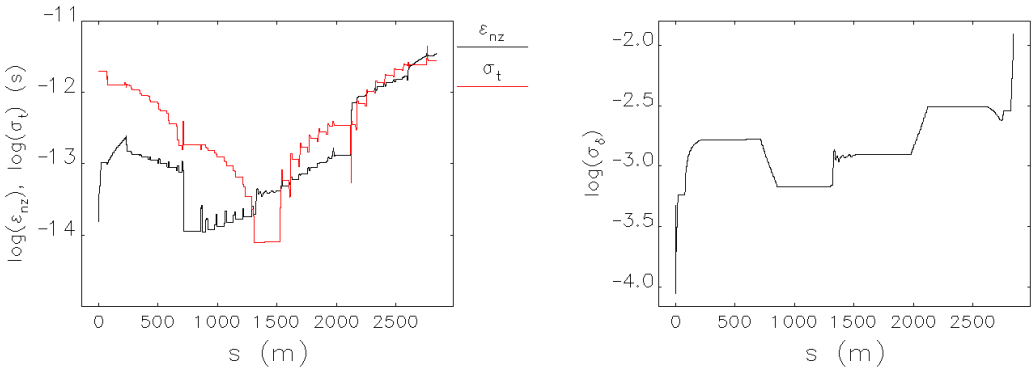

(a) Start-to-end longitudinal bunch properties of the 5 pC FELM.

(b) Energy modulation using a laser heater at $s \sim 1250\,\text{m}$.

Figure 6.32: Laser heater element used in the long undulators at $s > 1250\,\text{m}$ to simulate an FEL like energy modulation along the bunch.

The FSF is intended to operate at a repetition rate of 1.3 GHz. If such an FELM as presented in Fig. 6.30 is plausible then the average power of the light source would be

$$P_{\mathsf{av}} \;=\; 20\,\mathsf{MW}\cdot 10\,\mathsf{fs}\cdot 1.3\,\mathsf{GHz} \;=\; 260\,\mathsf{W} \tag{6.26}$$

This value compares well with the expectations of the XFEL facility presently under construction. The XFEL intends to produce between 300 - 800 W average power from its long pulse train [59]. If the beam degradation turns out to be underestimated in these preliminary simulations then the FEL could be operated well below the saturation. This is in keeping with the FEL upgrade proposals for storage rings namely [60].

This chapter has shown FSF as a candidate for a 4^{th} generation light source. The multi-turn ERL proposal uses SRF linacs to accelerate beams of exceptional brilliance. The LEM attempts to preserve a normalized emittance in the order of 0.1 mm mrad throughout the facility. The independent orbit acceleration allows adjustable optic design in the arcs for each beam energy to suppress emittance growth. The second mode SPM, presents higher order optic that uses longitudinal gymnastics to produce a 10 fs bunch. A compromise between the shortest bunch, largest bunch charge and transversal emittance growth was investigated. The third and final mode FELM opens up a new frontier for the FSF. Preliminary simulations of this mode using the optimal SPM parameters show great promise. The young investigators group at HZB are preparing a conceptual design report based on these and many other investigations regarding the FSF [68].

The final chapter introduces the concept of longitudinal instability of ERLs due to the beam-cavity interaction. The SPM depends on off-crest acceleration and longitudinal dispersion in the arcs, both of which make it susceptible to this type of instability.

7. Longitudinal Stability of ERLs

This chapter introduces the concept of longitudinal stability. The study begins with an investigation into the phase sensitivity setting of each linac in the FSF. The tolerance of the phase setting to slight adjustments is relatively low. The precision of the RF phase setting required for SPM operation is estimated using an analytic model and compared to the results of dedicated tracking simulations.

Focus is then turned to the concept of longitudinal instability due to the beam-cavity interaction. The acceleration of a charged bunch through the cavity is theoretically described as an equivalent RLC circuit. The passage of the beam induces a capacitive voltage which is discharged as a wake. This induced wake oscillates within the cavity and interacts with the returning bunch as it is decelerated. The interaction is in good analogy with the transverse case which is often referred to as Beam Break-Up [61] since both processes induce a perturbation which can limit the maximum current of an ERL based facility. Complex analysis of the inhomogeneous equations of the RLC circuit resonance is performed to obtain a stability matrix that describes the cavity-beam interaction. Eigenvalues of this matrix, describing either the exponential decay (stable) or growth (unstable) of the induced wake are dependent on the linac settings and the surrounding longitudinal magnetic optic.

The matrix stability criteria is used to benchmark equivalent numerical wakefield simulations for a simple 'one linac one turn' ERL model. This wakefield model is then further developed to analyze the more elaborate multi-turn, split linac acceleration scheme used in design of the FSF to deduce a theoretical threshold current.

7.1 Linac Phase Sensitivity

The longitudinal emittance recovery relation $T_{566}R_{65}^3 - T_{655} = 0$ described in Chapter 6.4.2 is used in the low energy FSF arcs when operating in the SPM. The relation can be used to introduce the concept of phase sensitivity. The energy considerations associated with acceleration are used to derive the relevant longitudinal matrix terms as follows

$$\begin{aligned} E_1 &= E_0 + U\cos\left(\omega\Delta t + \phi\right) \\ &= E_0 + U(\cos\left(\omega\Delta t\right)\cos\phi - \sin\left(\omega\Delta t\right)\sin\phi) \\ E_1 &= E_0 + U\left(\cos\phi\left(1 - \frac{(\omega\Delta t)^2}{2}\right) - \omega\Delta t\sin\phi\right) + ... \end{aligned}$$

from which

$$R_{65} = \frac{U\omega}{cE_1}\sin\phi \quad , \quad T_{655} = \frac{U\omega^2}{2c^2E_1}\cos\phi \tag{7.1}$$

Substituting these relations in to Eq. (6.8) one finds

$$T_{566} = \frac{T_{655}}{R_{65}^3} = \frac{c}{2\omega}\left(\frac{E_1}{U}\right)^2\frac{1}{\phi^3} \sim \frac{\lambda_{\mathsf{RF}}}{4\phi^3} \tag{7.2}$$

This optimum T_{566} setting for recovery is extremely sensitive to the linac phase setting. Technically feasible values for T_{566} are only obtained for relatively large off-crest acceleration phases, hence the main linacs in the SPM are $\Delta\phi_2 = 10\,^\circ$ and $\Delta\phi_3 = $ -20 $^\circ$ respectively.

Compression in the SPM is achieved in three stages. Firstly, the injection linac and arc are used to reduce the bunch length to 1 ps. Then the 1 and 2 GeV turns in the split linac section compress the bunch to 10 fs. The three linacs in the compression scheme all have different phase sensitivities due to the longitudinal dispersion in the surrounding arcs. The extent of the phase sensitivity found using tracking simulations $\mathrm{d}\phi_{\mathrm{sim}}$ given in Table 7.1 can be verified analytically by finding the root of the product of the longitudinal transfer matrix.

$$\begin{pmatrix} c\Delta t \\ \delta \end{pmatrix}_{\mathrm{end}} - \prod_{i=1}^{3} R_{\phi_i}\, R_{\mathrm{ARC}_i} \begin{pmatrix} c\Delta t \\ \delta \end{pmatrix}_{\mathrm{start}} = 0 \tag{7.3}$$

where

$$R_{\phi_i} = \begin{pmatrix} 1 & 0 \\ -\frac{U\omega}{cE_1}\sin\left(\phi_i + \mathrm{d}\phi_{\mathrm{root}}\right) & \frac{E_0}{E_1} \end{pmatrix}, \quad R_{\mathrm{ARC}_i} = \begin{pmatrix} 1 & R_{56_i} \\ 0 & 1 \end{pmatrix}$$

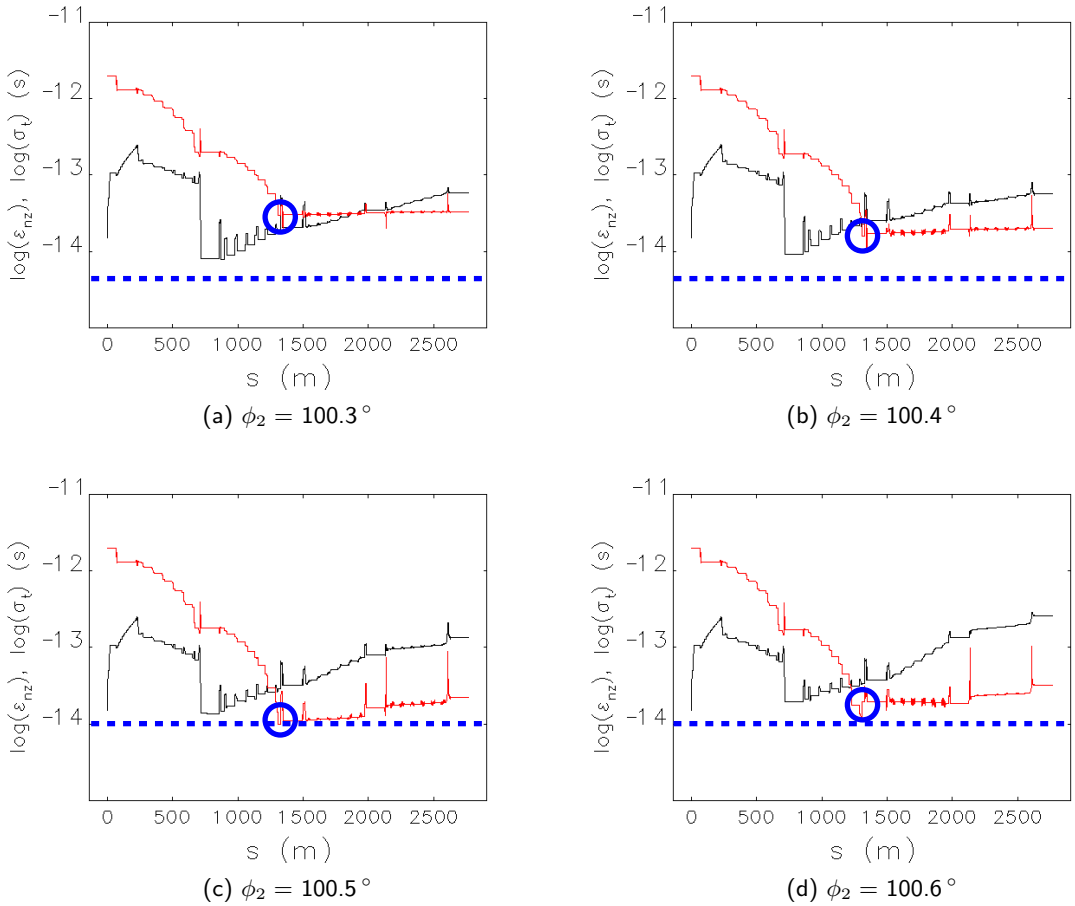

(a) $\phi_2 = 100.3\,^\circ$ (b) $\phi_2 = 100.4\,^\circ$

(c) $\phi_2 = 100.5\,^\circ$ (d) $\phi_2 = 100.6\,^\circ$

Figure 7.1: Phase sensitivity of the first split linac.

The figure of merit of the sensitivity is the phase shift $\mathrm{d}\phi_{\mathrm{root}}$ in a given linac required to double the final bunch length at 2 GeV, see $s = 1250$ m in Fig. 7.1. Blue circles help depict compression at

Table 7.1: Phase sensitivity of the SPM three stage compression scheme.

Pos.	i	ϕ_i (°)	dϕ_{sim} (°)	dϕ_{root} (°)	R_{56} (m)
Injection	1	92.90	0.15	0.16	0.38
Linac 1	2	100.45	0.10	0.07	0.20
Linac 2	3	69.00	3.50	3.28	0.08

2 GeV and the blue dashed line shows the 10 fs goal. Here only the sensitivity of the phase setting for the first split linac is shown.

Fig. 7.1 shows that the phase ϕ_2 only needs to vary by a 10^{th} of a degree from the minimum bunch length setting before the bunch length doubles. ϕ_1 and ϕ_2 are more prominent to phase sensitivity compared with ϕ_3 as they have higher longitudinal dispersion in their respective arcs.

The FSF is intended to operate in a CW mode at 1.3 GHz. Assuming the timing jitter of the bunch centroids after the compression do not exceed the length of a single bunch $\sigma_t \sim 10$ fs, the required bunch to bunch energy stability will be $\sigma_{_E} = c\sigma_t / R_{56}\sqrt{N_{\text{c}}} \sim 4$ keV per cell [62]. With $N_{\text{c}} > 500$ cells of $U = 13$ MV peak field the phase stability requirements for off-crest acceleration can be approximated as

$$\delta\phi_3 = \frac{\sigma_{_E}}{eU \sin\phi_3} \sim 0.05\,^\circ$$

This value for the bunch to bunch energy stability is comparable with the worst case phase sensitivity value given in Table 7.1. Recent studies have shown stable phase control of $0.01\,^\circ$ (microphonics controlled at 8 Hz) suggesting the single bunch phase sensitivity values are manageable [63].

To complement these phase sensitivity findings, the remaining sections of this chapter investigate the beam current threshold limit due to the beam-cavity interaction where both linac phase and longitudinal dispersion in the arc play a vital role. First a general relation for the R_{56} dependence on the threshold current is derived. Then RLC circuit theory is used to produce a matrix model that can be numerically verified using the wakefield analogy.

7.2 Longitudinal Beam Break-Up

In a similar manner to the more commonly described TBBU where the interaction of the beam with higher order modes causes instability, a general principle for Longitudinal Beam Break-Up (LBBU) due to the fundamental mode is given here.

In a single cavity model [64], the fundamental mode is used to accelerate a bunch. On passing through the cavity the electron bunch induces some voltage variation ΔU in the cavity that is seen by the recirculating bunch.

$$U = (U_0 + \Delta U)\cos(\omega t + \phi) \tag{7.4}$$

This accounts to an electron energy variation ΔE for a given phase ϕ of

$$\Delta E_1 = e\Delta U \cos\phi \tag{7.5}$$

which is described by the longitudinal matrix element of the turn to be

$$c\Delta t = \frac{\Delta E_1}{E} R_{56} = \frac{e\Delta U}{E} R_{56}\cos\phi \tag{7.6}$$

where $E = pc$. After deceleration the resulting energy variation is given by

$$\Delta E_2 = e(U_0 + \Delta U)\cos(\omega t + \phi) - e(U_0 + \Delta U)\cos(\omega(t + \Delta t) + \phi) \tag{7.7}$$

For a bunch of charge q and a recirculation time T_0 the energy variation equates to

$$\Delta E_2 = q(U_0 + \Delta U)\sin(\omega T_0 + \phi)\omega\Delta t \tag{7.8}$$

Considering only the additional change in energy and substituting Eq. (7.6) into the above equation gives

$$\Delta E_2 = qU_0 \sin(\omega T_0 + \phi)\frac{e\omega\Delta U}{cE} R_{56}\cos\phi \tag{7.9}$$

If the net energy transfer from the beam to the fundamental mode ΔE_2 is larger than the power dissipated in the cavity walls (Ohmic losses) then the system becomes unstable. For a bunch with a repetition rate f_{rep} the threshold relation approximates to

$$\Delta E_2 \cdot f_{\text{rep}} \;=\; \Delta E_2 \frac{I_{\text{th}}}{q} \;<\; \frac{(U_0 + \Delta U)^2 - U_0^2}{\rho Q} \;\simeq\; \frac{2\Delta U U_0}{\rho Q} \tag{7.10}$$

where $\rho = R/Q$. The threshold current is given by

$$I_{\text{th}} \;=\; \frac{2pc^2}{\rho Q e\omega R_{56}\sin(\omega T_0 + \phi)\cos\phi} \tag{7.11}$$

The general understanding of the threshold current given in Eq. (7.11) is that the LBBU is inversely proportional to the R_{56} value. If the longitudinal dispersion in the ERL turn is closed $R_{56} \to 0$ then there is no instability. This notion is revisited in Eq. (7.45) to find the precision of a closed longitudinal dispersion for a compact ERL. Other attributes to note is that the threshold current depends on the beam energy, cavity structure and linac phase setting. The most problematic cavities are therefore those that operate at lower energies, have a high quality factor and operate off-crest. In large scale facilities the recirculation time will help to damp this instability. Unlike the TBBU case, rather than considering a spectrum of higher order modes which may overlap or be damped by careful cavity design, LBBU is caused by the fundamental accelerating mode. The accelerating mode is engineered to be as large as possible and this instability is therefore always present to some extent.

There is also a clear analogy to the DC Robinson instability [65]. Here tuning the cavity reduces the induced beam loading voltage. The matrix theory derived in the next section reiterates the role R_{56} plays in the threshold current and delivers stability criteria for the beam-cavity interaction.

7.3 Stability Matrix of RLC Circuits

The stability matrix method used to find the threshold current of a simple ERL system is derived from the resonant nature of an RLC circuit. The sign of the eigenvalues of this matrix describe the stability [66]. Consider the beam-cavity as an RLC circuit as shown in Fig. 7.2.

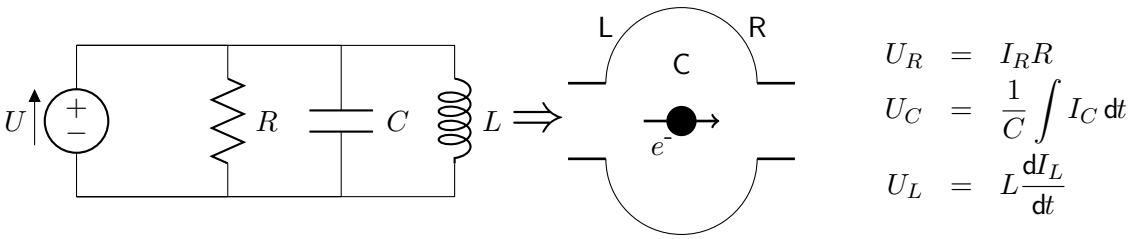

Figure 7.2: RLC circuit analogy for a single RF cavity.

Using the Kirchhoff current law for a parallel circuit, one can equate the sum of the currents I with the potential difference U across each element. From this the general inhomogeneous equation for a parallel RLC circuit is given by

$$\ddot{U} + \frac{1}{RC}\dot{U} + \frac{1}{LC}U = \frac{1}{C}(\dot{I}_\mathrm{b} + \dot{I}_\mathrm{g}) \tag{7.12}$$

where the driving force is given by the change in current due to both the beam $\dot{I}_\mathrm{b}$ and the generator $\dot{I}_\mathrm{g}$. A linac consists of parallel RLC circuits linked in series as shown in Fig. 7.3. Assuming all of the RLC cavities are identical $R_1 = R_2, C_1 = C_2$ and $L_1 = L_2$, the impedance Z of N_c linac circuits in series is given by

$$\frac{1}{N_\mathrm{c}Z} = \frac{1}{N_\mathrm{c}R} + \frac{j\omega C}{N_\mathrm{c}} + \frac{1}{N_\mathrm{c}j\omega L} \tag{7.13}$$

where j is a complex number and ω is the frequency. The effective voltage (real parts) across a linac $U = U_0\cos(\omega t + \phi)$ can be represented in terms of the phase angle of the complex impedance as

$$U = \Re\big(U_\alpha e^{-j\omega t}\big) \quad \text{where} \quad U_\alpha = U_0 e^{-j\phi} \tag{7.14}$$

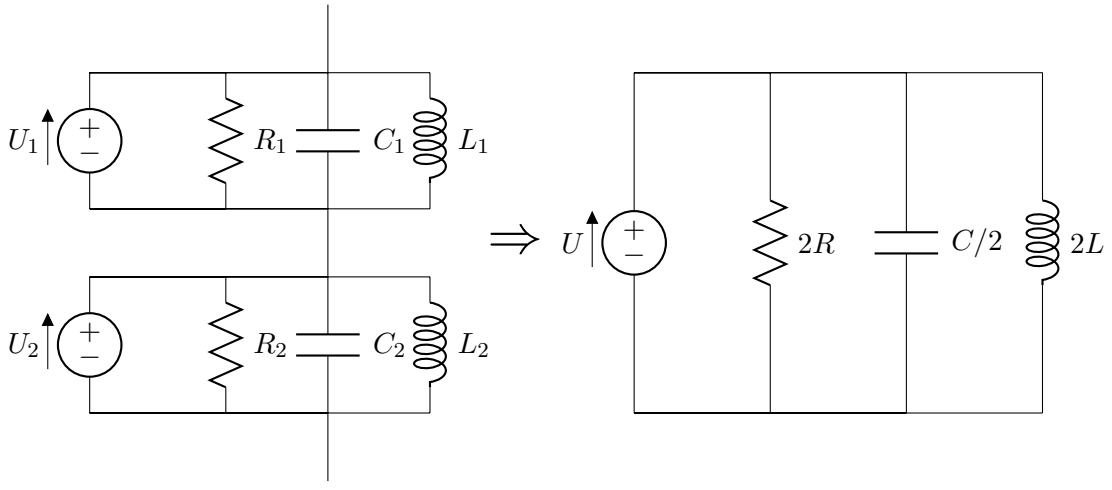

Figure 7.3: Parallel RLC circuits in series represented as an equivalent linac circuit.

where α is the bunch index and the phase $\phi \to \phi(t)$ depends on time. Likewise for the driving currents I_{b} and I_{g} one finds

$$I_{\mathsf{b}} = \Re\big(I_{\mathsf{b},\alpha}\, e^{-j\omega t}\big) \quad \text{and} \quad I_{\mathsf{g}} = \Re\big(I_{\mathsf{g},\alpha}\, e^{-j\omega t}\big) \tag{7.15}$$

and the derivatives of the voltage are such that

$$\dot{U} = \big(\dot{U}_\alpha - j\omega U_\alpha\big)e^{-j\omega t} \tag{7.16}$$
$$\ddot{U} = \big(\ddot{U}_\alpha - 2j\omega\dot{U}_\alpha - \omega^2 U_\alpha\big)e^{-j\omega t} \tag{7.17}$$

This notation can then be substituted into Eq. (7.12) to give

$$\ddot{U}_\alpha - 2j\omega\dot{U}_\alpha - \omega^2 U_\alpha + \frac{1}{RC}\big(\dot{U}_\alpha - j\omega U_\alpha\big) + \frac{1}{LC}U_\alpha = \frac{1}{C}\big(\dot{I}_{\mathsf{b},\alpha} + \dot{I}_{\mathsf{g},\alpha}\big) - \frac{j\omega}{C}\big(I_{\mathsf{b},\alpha} + I_{\mathsf{g},\alpha}\big) \tag{7.18}$$

Using the approximation that U_α is a slow changing function, that is $\ddot{U}_\alpha \ll \omega^2 U_\alpha$ for 1.3 GHz then $\ddot{U}_\alpha \to 0$ and Eq. (7.18) becomes

$$\dot{U}_\alpha\left(\frac{2}{\omega} + \frac{j}{\omega^2 RC}\right) - U_\alpha\left(j\left(1 - \frac{\omega_0^2}{\omega^2}\right) - \frac{1}{\omega RC}\right) = \frac{j}{\omega^2 C}\big(\dot{I}_{\mathsf{b},\alpha} + \dot{I}_{\mathsf{g},\alpha}\big) + \frac{1}{\omega C}\big(I_{\mathsf{b},\alpha} + I_{\mathsf{g},\alpha}\big) \tag{7.19}$$

where $\omega_0^2 = 1/LC$ is the resonant frequency. The normalized shunt impedance ρ is defined by the cavity geometry using the circuit definition

$$\rho = \frac{R}{Q_0} = \sqrt{\frac{L}{C}} = \frac{1}{\omega_0 C} \tag{7.20}$$

The characteristic impedance is given by

$$z(\omega) = \frac{R}{1 + j\omega\xi} \tag{7.21}$$

where $\xi = Q_0\big(\frac{\omega}{\omega_0} - \frac{\omega_0}{\omega}\big)$ is the detuning factor. Using these last few definitions Eq. (7.19) is reduced to a more manageable inhomogeneous equation

$$\dot{U}_\alpha\left(\frac{2}{\omega_0} + \frac{j}{\omega_0 Q}\right) + U_\alpha\left(\frac{1 - j\xi}{Q_0}\right) = \frac{j\rho}{\omega}\big(\dot{I}_{\mathsf{b},\alpha} + \dot{I}_{\mathsf{g},\alpha}\big) + \rho\big(I_{\mathsf{b},\alpha} + I_{\mathsf{g},\alpha}\big) \tag{7.22}$$

The stationary solution of this inhomogeneous equation is

$$U_{\alpha_0} = \frac{\rho(I_{\mathsf{b},\alpha} + I_{\mathsf{g},\alpha})Q_0}{1 - j\xi} \tag{7.23}$$

and a non-stationary solution would take the form $U_\alpha = U_{\alpha_0} + \Delta U$. A Taylor expansion of the current, then becomes

$$I_{\mathsf{b},\alpha} = I_{\mathsf{b},\alpha}\big(U_{\mathsf{b},\alpha_0} + \Delta U\big) \tag{7.24}$$
$$= I_{\mathsf{b},\alpha}\big(U_{\mathsf{b},\alpha_0}\big) + \left[\frac{\partial I_{\mathsf{b},\alpha}}{\partial \Re U}\Big|_{U_{\alpha_0}} \Re\Delta U + \frac{\partial I_{\mathsf{b},\alpha}}{\partial \Im U}\Big|_{U_{\alpha_0}} \Im\Delta U\right] + \ldots \tag{7.25}$$

For simplicity let $\dot{I} = \dot{I}_{\mathrm{b},\alpha} + \dot{I}_{\mathrm{g},\alpha}$ and likewise $I = I_{\mathrm{b},\alpha} + I_{\mathrm{g},\alpha}$ reducing Eq. (7.22) to

$$\Delta\dot{U}\left(\frac{2}{\omega_0} + \frac{j}{\omega_0 Q}\right) = \Delta U\left(\frac{j\xi - 1}{Q_0}\right) + \rho\left[\frac{\partial I}{\partial \Re U_{\alpha_0}}\Re\Delta U + \frac{\partial I}{\partial \Im U_{\alpha_0}}\Im\Delta U\right] + \frac{j\rho}{\omega}\dot{I} \tag{7.26}$$

Neglecting the time dependence of the current $\dot{I} = 0$, Eq. (7.26) becomes a homogeneous equation

$$\Delta\dot{U}\left(\frac{2}{\omega_0} + \frac{j}{\omega_0 Q}\right) = \Delta U\left(\frac{j\xi - 1}{Q_0}\right) + \rho\left[\frac{\partial I}{\partial \Re U_{\alpha_0}}\Re\Delta U + \frac{\partial I}{\partial \Im U_{\alpha_0}}\Im\Delta U\right] \tag{7.27}$$

and has the form $A\dot{X} = MX$ from which non-trivial solutions can be deduced in accordance with eigenvalues λ

$$|A^{-1}(A\lambda E - M)| = |A^{-1}||A\lambda E - M| \tag{7.28}$$

where $E = \begin{pmatrix} 1 & 0 \\ 0 & 1 \end{pmatrix}$ is the unit matrix and

$$A = \begin{pmatrix} \frac{2}{\omega_0} & -\frac{1}{Q_0\omega} \\ \frac{1}{Q_0\omega} & \frac{2}{\omega_0} \end{pmatrix} \quad , \quad \boxed{M = \begin{pmatrix} -\frac{1}{Q_0} + \rho\frac{\partial \Re I}{\partial \Re U} & \rho\frac{\partial \Re I}{\partial \Im U} - \frac{\xi}{Q_0} \\ \frac{\xi}{Q_0} + \rho\frac{\partial \Im I}{\partial \Re U} & -\frac{1}{Q_0} + \rho\frac{\partial \Im I}{\partial \Im U} \end{pmatrix}}$$

For simplicity, the bunch index α is removed from the matrix notation as the instability is charge dependent and is therefore valid for both single and multi-bunch investigations. The determinant given in Eq. (7.28) takes the lengthly form

$$\begin{aligned} |A\lambda - M| &= 0 \\ &= \lambda^2\left(\frac{4}{\omega_0} + \frac{1}{Q_0^2\omega^2}\right) \\ &+ \lambda\left(\frac{4}{\omega_0 Q_0} - \frac{2\rho}{\omega_0}\frac{\partial \Re I}{\partial \Re U} - \frac{2\rho}{\omega_0}\frac{\partial \Im I}{\partial \Im U} - \frac{2\xi}{\omega Q_0^2} - \frac{\rho}{\omega Q_0}\frac{\partial \Im I}{\partial \Re U} + \frac{\rho}{\omega Q_0}\frac{\partial \Re I}{\partial \Im U}\right) \\ &+ \left(\rho^2\frac{\partial \Re I}{\partial \Re U}\frac{\partial \Im I}{\partial \Im U} - \rho^2\frac{\partial \Re I}{\partial \Im U}\frac{\partial \Im I}{\partial \Re U} + \frac{1}{Q_0^2} - \frac{\rho}{Q_0}\frac{\partial \Re I}{\partial \Re U} - \frac{\rho}{Q_0}\frac{\partial \Im I}{\partial \Im U}\right. \\ &- \left.\frac{\rho\xi}{Q_0}\frac{\partial \Re I}{\partial \Im U} + \frac{\xi^2}{Q_0} + \frac{\rho\xi}{Q_0}\frac{\partial \Im I}{\partial \Re U}\right) \end{aligned}$$

Matrix A differs from the unit matrix E only by Q_0

$$A = \frac{2}{\omega_0}\begin{pmatrix} 1 & -\frac{1}{2Q_0} \\ \frac{1}{2Q_0} & 1 \end{pmatrix} \tag{7.29}$$

If Q_0 is large and the perturbation occurs on resonance $\omega \to \omega_0$, then the detuning factor $\xi \to 0$ and the solution of the eigenvalues λ from the lengthly determinant takes a simpler quadratic form

$$\lambda^2 - \mathrm{Tr}(M)\lambda + |M| = 0 \tag{7.30}$$

Solutions of the homogeneous equation Eq. (7.27) are in the form $e^{\lambda t}$ and the sign of the eigenvalue defines the stability:
for $\Re(\lambda) > 0$ the solution is unstable, resulting in exponential growth or
if $\Re(\lambda) < 0$ the solution is stable leading to damped oscillations.

The solutions $\lambda_{1,2}$ of the quadratic equation are found using

$$\lambda_{1,2} = \frac{\mathsf{Tr}(M) \pm \sqrt{\mathsf{Tr}(M)^2 - 4|M|}}{2}$$

Multiple solutions exist. The elements of the matrix M are real therefore the $\mathsf{Tr}(M)$ is real too. The discriminant is then either:

real	$\mathsf{Tr}(M)^2 - 4\|M\| < \mathsf{Tr}(M)^2$	then	$4\|M\| > 0$
or imaginary	$\mathsf{Tr}(M)^2 - 4\|M\| < 0$	then	$\mathsf{Tr}(M)^2 < 4\|M\|$

Both cases are true when $\mathsf{Tr}(M) < 0$, meaning all real eigenvalues $\Re(\lambda) < 0$ and the system is stable [67].

The coefficient b_λ of the linear λ term from the lengthly determinant $|A\lambda - M|$ can be used to estimate the importance of the detuning factor ξ about the resonance. Given the partial derivatives obey simply Ohms law $\partial\Re I \,/\, \partial\Re U \sim 1 \,/\, R$ then

$$b_\lambda \;\simeq\; \frac{4}{\omega_0 Q_0} - \frac{2R}{\omega_0 Q_0}\left(\frac{1}{R} + \frac{1}{R}\right) - \frac{2\xi}{\omega Q_0^2} + \frac{R}{\omega Q_0^2}\left(\frac{1}{R} - \frac{1}{R}\right) = -\frac{2\xi}{\omega Q_0^2}$$

This indicates that the stability criteria $b_\lambda > 0$ can be solely controlled by the detuning factor. This is the principle of present day machines where the resonant frequency must be slightly detuned from the drive frequency in order to achieve the minimum reflected power for a beam loaded cavity [65].

7.4 Wakefield Formalism

The previous section has shown that linear solutions to the voltage dependent inhomogeneous equation Eq. (7.12) are valid for high quality factor values. The time dependence of the drive currents $\dot{I}_b$ and $\dot{I}_g$ were neglected which reduces the system to a homogeneous form

$$\ddot{U} + \frac{1}{RC}\dot{U} + \frac{1}{LC}U = 0 \tag{7.31}$$

Given these approximations, an alternative numerical method is investigated to compare with the matrix solution and solve more elaborate systems. The numerical solution of this homogeneous equation takes the general form

$$U(t) = e^{-\frac{\omega_0 t}{2Q_0}}\Big(A\cos(\omega t) + B\sin(\omega t)\Big) \tag{7.32}$$

In the short bunch approximation $I(t) = q\delta t$, the bunch excites a capacity voltage in the cavity U whose stored energy is equal to that lost by the bunch E.

$$U = \frac{q\omega_0 R}{Q_0} \quad \rightarrow \quad E = \frac{qU}{2} \tag{7.33}$$

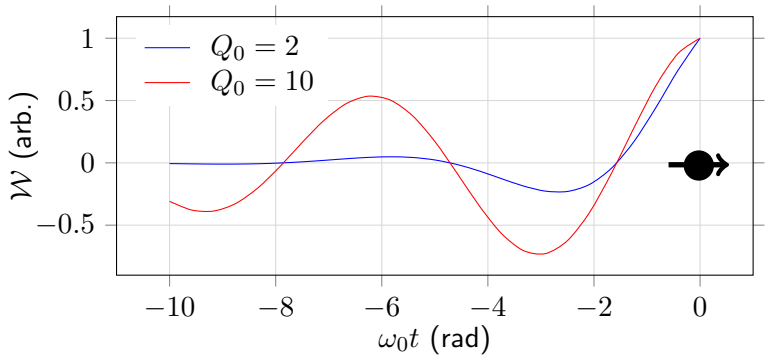

Figure 7.4: Under-damped oscillations of a wake function.

The capacitor then discharges through the resistor producing a voltage gradient

$$\dot{U} = \frac{q\omega_0^2 R}{Q_0^2} \tag{7.34}$$

These last few equations for an instantaneous (t=0) voltage and gradient due to the capacity discharge $\omega_0/2Q_0 \rightarrow -\omega_0/2Q_0$ are used to find the constants $A = q\omega_0 R/Q_0$ and $B = A/\sqrt{4Q_0^2 - 1}$. The general solution for the damped harmonic system of a cavity becomes

$$U(t) = q\frac{\omega_0 R}{Q_0} e^{-\frac{\omega_0 t}{2Q_0}} \left(\cos\left(\omega_0 \sqrt{1 - 1/4Q_0^2}\, t\right) + \frac{1}{\sqrt{1 - 4Q_0^2}} \sin\left(\omega_0 \sqrt{1 - 1/4Q_0^2}\, t\right) \right) \tag{7.35}$$

The time dependent solution for the voltage induced in the cavity by the passing of a charge is commonly referred to as the wake $\mathcal{W}$. For large Q_0 values, the geometric wake function $\mathcal{W}$ takes the form

$$\mathcal{W}(t) \simeq e^{-\frac{\omega_0 t}{2Q_0}} \cos(\omega_0 t) \tag{7.36}$$

The trailing wake originates from the bunch and develops behind it as shown in Fig. 7.4. The wake itself is a unit-less function that is commonly multiplied by the charge, loaded shunt and frequency in order to have the more useful units of a Volt.

7.5 Stability Considerations for a Single Turn ERL

The wakefield formalism and matrix analogy introduced in the previous two sections are compared here for a simple 'one linac one turn' theoretical ERL machine. The intent of this section is to benchmark the two complementary models. Once verified, more complex multi-turn linac and arc structures like those present in the FSF can be investigated using extensions to the numerical simulations.

The recurrent system starts with an initial injection. The bunch described as short, of charge q is accelerated to an energy eU_1 in a single cavity model and induces a wake $\mathcal{W}_1$ at time t_0 given by

$$\mathcal{W}_1 = q\frac{\omega R}{Q} e^{-\frac{\omega t_0}{2Q}} e^{-i(\omega t_0 + \delta\phi_1)} \tag{7.37}$$

where $\delta\phi_1$ is the initial phase deviation. The bunch and wake both oscillate on resonance. The complex impedance is restricted to the amplitude of the loaded shunt $\rho = R/Q$, this value given in Table 7.2 is a factor 2 more than that of the circuit definition in Eq. (7.20). An accelerating bunch

experiences a summation of all the previous wakes in time depending on the complex angle. The accelerated bunch exits the linac with a relative energy deviation δE_1 given by

$$\delta E_1 = \delta E_0 \frac{E_\mathsf{i}}{E_\mathsf{f}} + \frac{e}{E_\mathsf{f}} \Big(\mathcal{W}_1 + U_1 \big(e^{-i(\phi_1 + \delta\phi_1)} - e^{-i\phi_1} \big) \Big) \tag{7.38}$$

where δE_0 is the initial energy deviation, E_i and E_f are the energies on entrance and exit of the linac respectively. The accelerated bunch then traverses a magnet optic in the turn. The longitudinal dispersion R_{56} setting in the turn can influence the phase advance $\delta\phi$ of the bunch before re-entering the linac for deceleration.

$$\delta\phi_2 = \delta\phi_1 + \frac{\omega}{c} \delta E_1 R_{56} \tag{7.39}$$

On recovery the time of flight of the bunch is $t_\mathsf{r} = T_0 + \delta\phi_2/\omega$ where T_0 is the reference recirculation time. Decelerating the bunch with phase $\phi_2 = \phi_1 + 180\,^\circ$ during the energy recovery process induces a second wake $\mathcal{W}_2$ which is to be summed with the previous wake in a recursive manner. The resulting wake $\mathcal{W}_\mathsf{T} = \mathcal{W}_1 + \mathcal{W}_2$ then oscillates accordingly, damped oscillations are stable and exponential growth is unstable. The relative energy deviation δE_2 is a measure of the beam losses in the cavity on recovery

$$\delta E_2 = \delta E_1 \frac{E_\mathsf{f}}{E_\mathsf{i}} + \frac{e}{E_\mathsf{i}} \Big(\mathcal{W}_2 + U_2 \big(e^{-i(\phi_2 + \delta\phi_2)} - e^{-i\phi_2} \big) \Big) \tag{7.40}$$

Once decelerated, the bunch is dumped. A fresh bunch is then injected at time t_b with zero initial phase and energy deviation and the superposition of wakes is found at a time $t = t_\mathsf{b} - t_\mathsf{r}$. The recursive process then starts again from Eq. (7.37) and takes all the previous wakes and decay times into account.

The mechanics behind this model is pictorially described in Fig. 7.5 using a phasor diagram. Making the assumption that the voltage discrepancy $U_\mathsf{loss} = U_1 - U_2$ is real, this Ohmic loss needs to be readily corrected by the generator U_g input. The voltage tilt represents the fact that the impedance may contain complex parts and the diagram is valid for one frequency. The excited wake due to the beam-cavity interaction is a temporal mechanism and depending on the wake parameters can lead to an instability.

The generator is required to be detuned by ψ to compensate the extra beam loading due to the induced wake imbalance $\mathcal{W}_1 > \mathcal{W}_2$ as shown in Fig. 7.5 by

$$\tan\psi = -2\xi \tag{7.41}$$

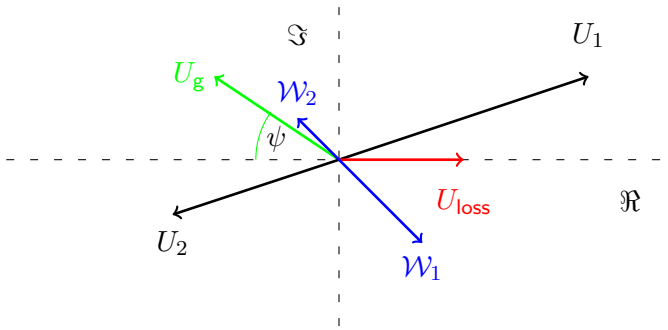

Figure 7.5: Instantaneous complex phasor diagram with a wake imbalance.

Table 7.2: Wake simulation parameters.

R_{56}	f	R/Q	Q	E_i	E_f	turn	t_b	ϕ_1
0.5 m	1.3 GHz	777 Ω	$5{\cdot}10^7$	0.1 GeV	1 GeV	2000.5 λ	$2{\cdot}T_0$	98 °

However, the generators response given by

$$\tau_\mathrm{g} \sim Q/f \tag{7.42}$$

is in the order of $\tau_\mathrm{g} \sim 40\,\mathrm{ms}$ when using the parameters in Table 7.2. This response is inherently slow in comparison with time before a fresh bunch is injected $t_\mathrm{b} \sim 3\,\mu\mathrm{s}$. The instability would occur independent of the generators response.

The parameters of the following simulations were chosen with the FSF in mind. Modular 7-cell SRF cavities operating at 1.3 GHz are used to produce a final beam energy of 1 GeV. Acceleration is off-crest and the longitudinal dispersion is not closed $R_{56} \neq 0$ resulting in bunch compression. A code was written to numerically simulate the beam-cavity interaction in a 'one linac one turn' scenario. Each wake is summed using the theory of superposition using Eq. (7.37) to Eq. (7.40) as the bunch passes twice through the linac before the next fresh bunch is injected.

Fig. 7.6 shows a schematic of the simple model at the point t_2 before the bunch re-enters the linac for deceleration. The extent to which the wake produced on deceleration will cancel the wake produced on acceleration $\mathcal{W}_1$ is determined by the time of flight in the turn.

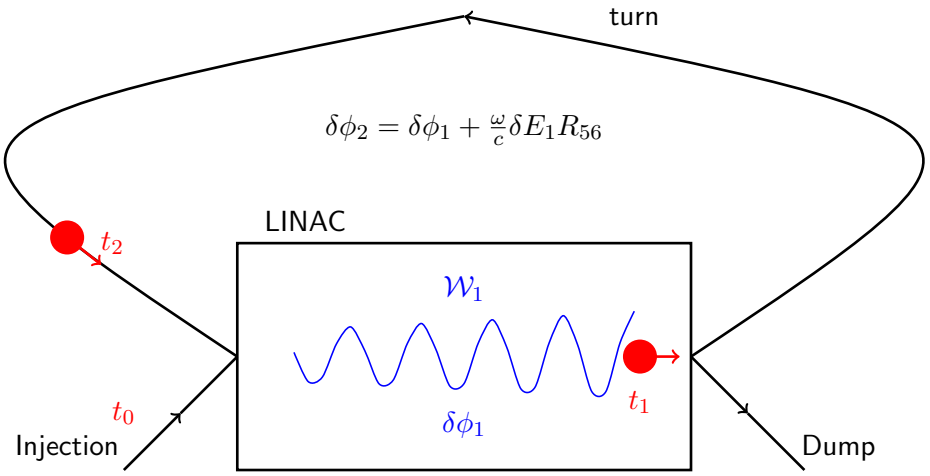

Figure 7.6: Wake model mechanism depicted just before bunch re-entry.

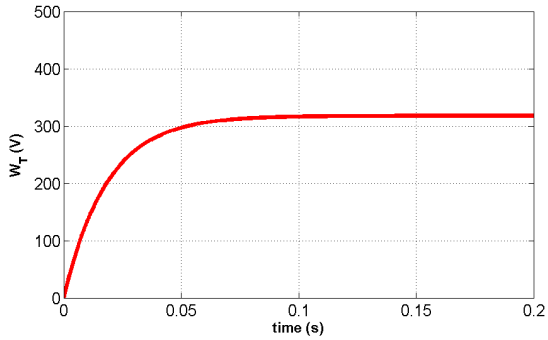

Figure 7.7: Low current steady state stable solution.

Fig. 7.7 shows the stable low current 32 μA wake $\mathcal{W}_\mathsf{T}$ due to the bunch passing twice through the linac, given the ERL properties in Table 7.2. Even though the longitudinal dispersion is non-zero the charge of the single bunch is low enough to establish damped motion and portray a steady state system. Each point on the curve is the total wake when each bunch is dumped. Therefore intermediate wake oscillations are not shown. The final value for the wake $\mathcal{W}_\mathsf{T} \sim 300\,\mathsf{V}$ can be readily compensated for by a generator.

Increasing the charge of the single bunch used in the simulations will obviously lead to an unstable system. The general instability criteria is given by the partial derivative in the M matrix. The threshold current is found through closer inspection of this derivative

$$\begin{aligned} I &= I_0\, e^{\,j\phi} \\ \frac{\partial I}{\partial U} &= \frac{\partial I_0}{\partial U}\, e^{\,j\phi} + I_0\, j\, \frac{\partial \phi}{\partial U}\, e^{\,j\phi} \end{aligned} \tag{7.43}$$

The instability is investigated for one particular bunch charge at a instantaneous time therefore $\partial I_0 \,/\, \partial U = 0$, leaving

$$\frac{\partial I}{\partial U} = I_0\, j\, \frac{\partial \phi}{\partial U}\, e^{\,j\phi} \tag{7.44}$$

By substituting $\phi = U R_{56} \,/\, \lambda_\mathsf{RF} E_\mathsf{f}$ in to the above definition one can approximate the precision by which the longitudinal dispersion in an ERL turn needs to be closed as follows

$$\frac{\partial I}{\partial U} = j\, \frac{I_0 R_{56}}{\lambda_\mathsf{RF} E_\mathsf{f}}\, e^{\,j\frac{U R_{56}}{\lambda_\mathsf{RF} E_\mathsf{f}}} \tag{7.45}$$

$$\frac{\partial \Re I}{\partial \Re U} = \frac{I_0 R_{56}}{\lambda_\mathsf{RF} E_\mathsf{f}}\, \sin\!\left(\frac{U R_{56}}{\lambda_\mathsf{RF} E_\mathsf{f}}\right)\Bigg|_{\mathsf{max}} \quad \Rightarrow \quad \frac{I_0 R_{56}}{\lambda_\mathsf{RF} E_\mathsf{f}} \simeq \frac{1}{R} \tag{7.46}$$

The bERLinPro compact ERL envisages 100 mA average current at 50 MeV using three 7-cell SRF cavities, therefore the precision by which the longitudinal dispersion needs to be closed is

$$\begin{aligned} \frac{I_0 R_{56}}{\lambda_\mathsf{RF} E_\mathsf{f}} &\simeq \frac{1}{\rho Q} \\ R_{56_\mathsf{closed}} &= \frac{\lambda_\mathsf{RF} E_\mathsf{f}}{I_0 \rho Q} \\ &= \frac{0.23\,[\mathsf{m}] \cdot (50 \cdot 10^6\,[\mathsf{V}])}{2 \cdot 0.1\,[\mathsf{A}] \cdot 3(777/2\,[\Omega] \cdot 5 \cdot 10^7)} \\ R_{56_\mathsf{closed}} &\simeq 1\,\mathsf{mm} \end{aligned} \tag{7.47}$$

To be consistent, a Gaussian short bunch using [65] was assumed so that $I_0 \rightarrow 2I_0$ and the linac value for ρ was halved to be the circuit value. Eq. (7.45) shows that the derivative $\partial I/\partial U$ is directly proportional to the longitudinal dispersion R_{56}. This means that an optic with $R_{56} < 0$ is always stable $\mathsf{Tr}(M) < 0$ and will result in a negative threshold current. This inherent consequence limits the linear matrix theory to simple models. The FSF envisages optic with both positive and negative longitudinal dispersion and hence requires a more elaborate numerical model.

The stability criteria for the two complementary approaches are given below.

1) The matrix method

Since the instability results from a beam induced wake one can redefine the partial derivative from Eq. (7.44) as

$$\frac{\partial I}{\partial U} = I_0\, j\, \frac{\partial \phi}{\partial U}\, e^{\,j\phi} \;\rightarrow\; \frac{q}{t_b}\, j\, \frac{\partial \phi}{\partial \mathcal{W}}\, e^{\,j\phi} \tag{7.48}$$

The value $\partial\phi\,/\,\partial\mathcal{W}$ can be read numerically from the first and second injections and substituted into the trace of matrix M for the non-trivial solution of Eq. (7.27). The resulting formula

$$\mathsf{Tr}(M(t)) = \frac{qR}{t_b Q}\left(\Re\frac{\partial\phi(t)}{\partial\mathcal{W}(t)} + \Im\frac{\partial\phi(t)}{\partial\mathcal{W}(t)}\right) - \frac{2}{Q} \tag{7.49}$$

describes a system that is unstable when $\mathsf{Tr}(M(t)) > 0$.

2) The numerical simulations method

In addition to plotting the trend of the wakes as was used in the low current example Fig. 7.7, the complex phase space diagrams should also show the true nature of the oscillations. Below the threshold in Fig. 7.8 the stable solution decays in the form a of a spiral. At the critical threshold the plot takes the form of a circle. Above the threshold in Fig. 7.8 the solutions spiral outwards from the circle and describe an unstable system.

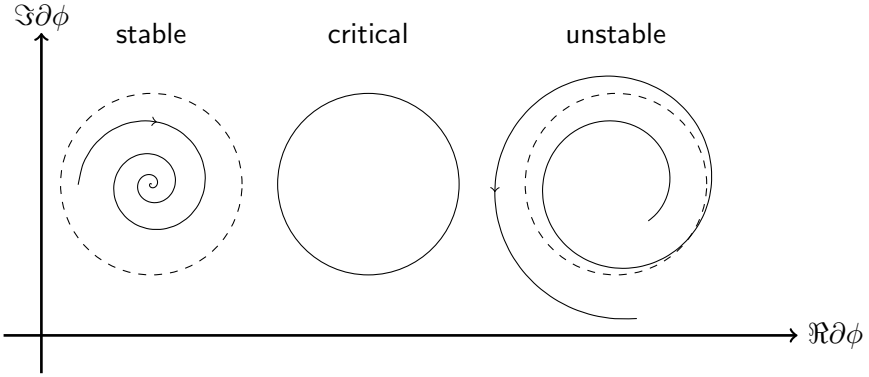

Figure 7.8: Complex phase diagrams across the threshold limit.

These three theoretical situations describing the complex phase plots across the threshold limit are clear to see in the simulation results shown in Fig. 7.9 using the parameters in Table 7.2. Again, one point per injection is plotted. At these higher beam current values, the wake oscillates turn by turn. The offset $\mathcal{W}_\mathsf{T} \sim 0.6\,\mathrm{MV}$ shown in Fig. 7.9a is the beam loading extent due to the induced wakes. Many fresh injections are presented here to portray the trend predicted in Fig. 7.8. In practice only a second injection is required to obtain the state of the stability. Many turns are unjustified, the system either grows exponentially or is damped from the second injection onwards.

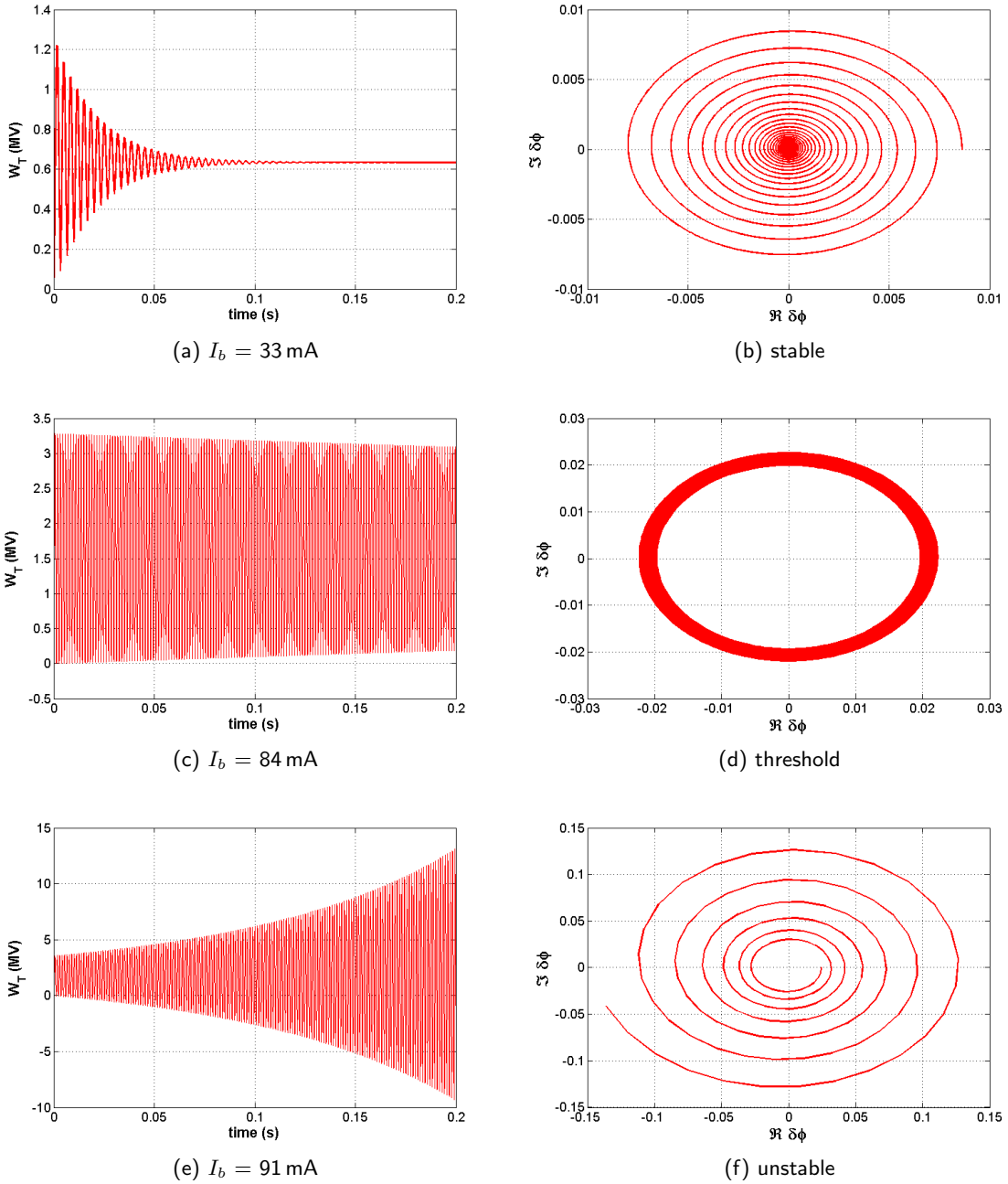

(a) $I_b = 33\,\mathrm{mA}$ (b) stable

(c) $I_b = 84\,\mathrm{mA}$ (d) threshold

(e) $I_b = 91\,\mathrm{mA}$ (f) unstable

Figure 7.9: Numerical based wake simulation results crossing the threshold current.

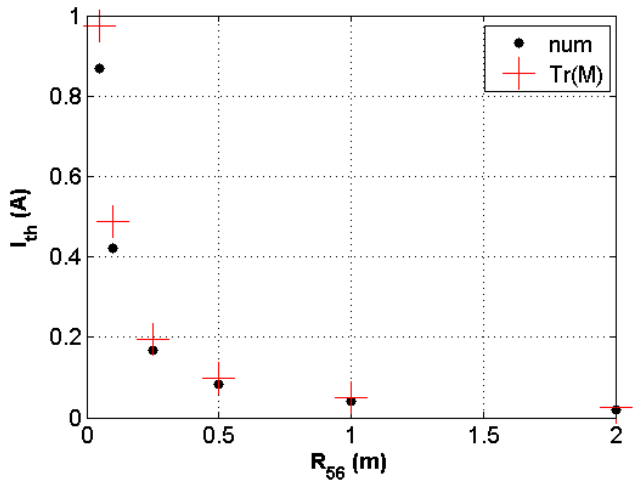

Figure 7.10: Threshold current values due to beam-cavity interaction for numerical and matrix based wake analysis of the 'one linac one turn' model.

Fig. 7.10 shows the numerical wake simulations are in good agreement with those using the linear matrix theory. The trend is as predicted $I_{\text{th}} \sim \text{const}/R_{56}$ with a singularity existing at $R_{56} = 0$. In practice this singularity would not exist if higher order terms where taken into account. Expanding Eq. (7.39) to include 2$^{\text{nd}}$ order terms, the relative phase deviation $\delta\phi_2$ due to the time of flight in the recirculator becomes

$$\delta\phi_2 = \delta\phi_1 + \frac{\omega}{c}\delta E_1 R_{56} + \frac{\omega}{c}\delta E_1^2 T_{566} + ... \tag{7.50}$$

for which T_{566} can be non-zero. Fig. 7.11 shows that by including this term the maximum threshold limit when $R_{56} \to 0$ becomes approximately 4 A.

The intention of this section was not to find an exact value for the threshold current, but to compare the results of the matrix and numerical methods. The positive outcome suggests a more complicated system of multi-turns can be numerically simulated with confidence to find threshold values.

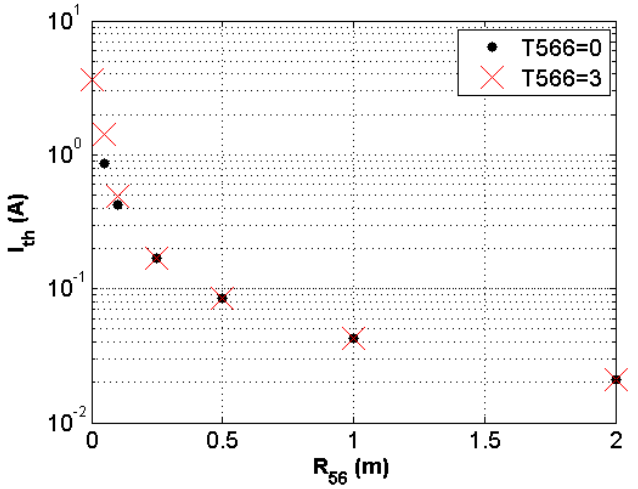

Figure 7.11: Threshold current values due to beam-cavity interaction for first and second order numerical wake analysis of the 'one linac one turn' model.

7.6 Estimation of the Threshold Current for a Multi-turn Split Linac ERL Model

With the FSF layout in mind, the numerical analysis using the summation of wakes is further developed to include a second linac and additional turns. Fig. 7.12 shows the first two turns of the FSF using split linacs where longitudinal dispersion is present in all arcs. The injection stages are neglected in this simplified model. Applying the standard recovery option of the SPM presented in Chapter 6.5, red indicates the acceleration optic from 0.1 to 1.9 GeV. Symmetric deceleration to recover the beam is shown in blue with $R_{56_\mathrm{d}} = -R_{56_\mathrm{a}}$.

The recursive system is more complicated for the split linac model but the strategy is the same as for the previous 'one linac one turn' example. The critical points to consider are that multiple wakes in both linacs develop at different relative times. The path length of the larger turn is 1860.5λ and has a closed dispersion. The smaller arcs however have non-zero R_{56} values and produce phase deviations due to the time of flight. The phase settings of the linacs are either side of on-crest as proposed in the telescopic bunch compression scheme in Chapter 6.4.1.

Using the parameters in Table 7.3 the threshold current is approximately 120 mA. Even though the start-to-end longitudinal dispersion is closed $\sum R_{56} = 0$, a threshold exists as there are intermediate acceleration stages in this split linac model. The imbalance due to the time of flight on recovery induces energy deviations δE_2 given by Eq. (7.40) that do not cancel out.

The initial estimation of 120 mA is more than a magnitude greater than the SPM 6.5 mA specification (5 pC at 1.3 GHz). Although promising, this result needs to be taken with precaution. The model is approximate and restricted due to its simplicity and warrants a discussion.

Firstly, treating this beam-cavity interaction as a single rather than a multi-bunch mechanism is creditable as a threshold exists in either case. One could fill all available RF buckets with low

Table 7.3: Split linac simulation parameters.

f	R/Q	Q	t_b	ϕ_A	ϕ_B	R_{56_1}	R_{56_2}	R_{56_3}	R_{56_4}
1.3 GHz	111 Ω	5·10^7	2*T_0	100 °	70 °	0.2 m	0.08 m	-0.08 m	-0.2 m

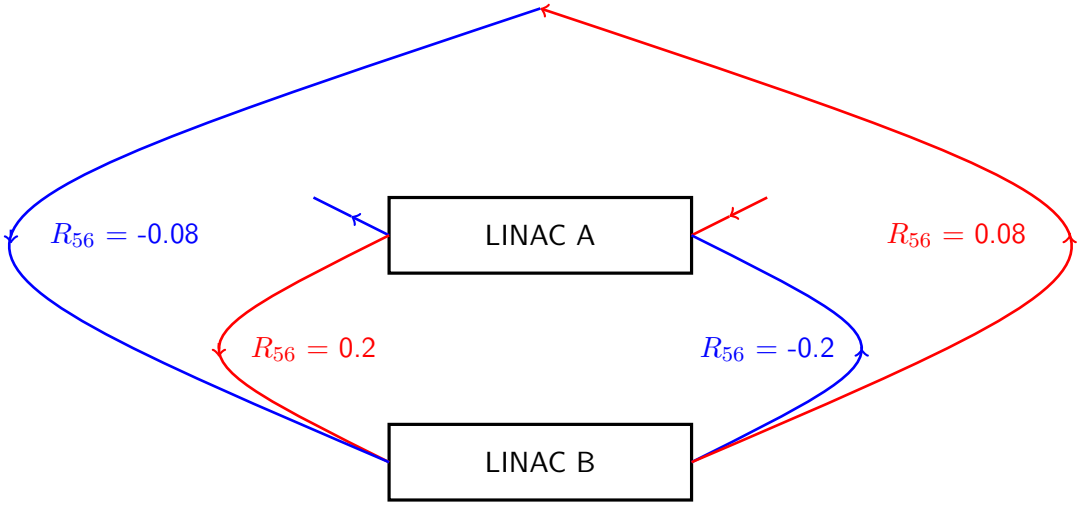

Figure 7.12: Low energy turns of the FSF split linac ERL model.

charge bunches or as indeed in this simulation take a single bunch to represent the summation of the individual charges is a valid approximation.

Secondly, the length of the linac is neglected. It is approximated as a single SRF cavity of zero length, capable of 1 GeV energy acceleration. This is unphysical. Rather a series of nine cryomodules each containing eight standard 7-cell linacs is envisaged. Intermediate stages of magnetic optic also exist to control the transverse optic functions as described in Chapter 6. By dividing the threshold current by the total number of cells which is $N_c = 504$, one could speculate the threshold to be a fraction of 1 mA. This last notion is reasonable but also unjust since the wakes would then be considered as uncoupled and treated for each cavity independently and instantaneously. The linacs make approximately a 5^{th} of the total length of the FSF and therefore significant additional damping time would be neglected.

Thirdly, the model also neglects the high energy arcs $3 \rightarrow 6 \rightarrow 3$ GeV. This estimation would be acceptable if the phase settings in these linacs were all on-crest. Although the optic in these arcs are isochronous, producing no additional longitudinal dispersion, the phase deviation from the lower energy arcs would propagate throughout the acceleration and deceleration stages causing supplementary energy deviations again given by Eq. (7.40). This would then in turn lower the threshold value.

From these suggestions, one could propose that this numerical model is valid per uncoupled linac module. In that sense the beam-cavity interaction is localized along the linac structure depending on the coupled cavity parameters. An exponential growth of the wake in any intermediate stage would limit the threshold current of the whole facility. Given the present FSF linac design each 7-cell module would have a separate generator then the threshold would be in the order of 17 mA.

This scenario is also illustrated in the revised TBBU investigations for the FSF design report [68]. The threshold current can be reduced by a magnitude in a similar fashion as described above if one single excited mode exists, the bandwidths of the mode range partially overlap or all cells have the same mode.

Extensions to the analytical code are foreseen, again in [67] but are beyond the scope of this thesis. Reserve optic should also be considered that can be adapted to reduce the longitudinal dispersion in the arcs and help raise the threshold current. Simply by halving the R_{56} in each turn for this simple model the threshold increases by a factor 5. These parameter changes would however compromise the minimum bunch length achievable using the SPM bunch compression scheme.

The notion one should take from these preliminary findings is the threshold current is theoretically within reach of the FSF design specification and additional investigations are a necessity.

8. Summary

Light sources throughout the world are operated in non-linear regimes where higher order optic plays an integral role to preserve high beam quality. This notion is fundamental to the short pulse mode operation and has played a pivotal role in this thesis. Comprehensive studies of the main attributes associated with theoretically generating femtosecond long electron bunches have met the objective of this work.

Radiation effects were considered in great detail and have been categorized. Analytical expressions describing the most relevant processes were derived in order to estimate the restrictions on the minimum bunch length achievable. Quantification of the incoherent nature of energy fluctuations of many body particle systems have been shown not to limit the bunch length when one considers reasonable optic for low transversal emittance. Effects based on coherent radiation are identified as the main restrictions on both the charge and bunch length. Analytical calculations were verified using particle tracking simulations.

Measurements of the key longitudinal parameters in the low energy stages of two very different ERL light sources were performed. ALICE represents the trend in compact ERL facilities based on SRF technology whereas the NovoFEL is a multi-turn accelerator. The measured injector bunch length at ALICE is already as low as any 3^{rd} generation machine and acts as just a starting point for compression to fs bunch lengths. Experimental setup, data taking and analysis were undertaken and the results are reproducible and confidently lie within the predictions of the theory. The experimental studies address the approaches used to overcome technical limitations by implementing higher order optic, alternative recovery schemes and transversal acceptance optimization. The ERL light source is presently a test stand and novel ideas are required to move this technology onwards.

A theoretical compact arc is devised to combat the collective effects common with short bunches. Transversal emittance growth suppression using phase advance manipulation schemes and unique 2^{nd} order chromatic correction optic are investigated and implemented into a compact arc. These analytical methods are an extension to an already essential field of study to reduce beam degradation due to radiation effects and with it the safe transport of bunches of large energy spreads. These techniques were found to be applicable to maintain the high quality beam parameters of the next generation light source using particle tracking simulations.

If multi-turn ERL based light sources are to be considered as a possible candidate for the future then the results of dedicated start-to-end particle tracking simulations are essential to verify expectations. Producing such an accumulation of optic for a large scale facility was achieved by paying particular attention to the project objectives and incorporating the project milestones in an iterative and dynamic way. The results of this thesis are an essential part of the FSF design report.

The short pulse mode of the FSF concept is thoroughly presented. The simulation objective of producing a 10 fs long bunch is achieved using an innovative longitudinal emittance recovery technique. The evolution of the 6D phase space was studied in order to produce high brilliance photons. A con-

sequence of the extensive investigations into finding the optimum optic for a short bunch, introduced an alternative FEL mode that shows great potential for the future.

The longitudinal stability of future ERLs in short pulse mode operation could be jeopardized by the beam-cavity interaction. Linear matrix based models are derived and compared with a more mandible numerical wakefield approach to estimate the beam current thresholds affiliated with energy deviations due to the time of flight in a recirculator.

In conclusion, experimental and theoretical investigations have given an insight into new thresholds underlining the key parameters related to the short bunch operation of next generation ERL facilities.

Bibliography

[1] First proposal; M Tigner 1965 Nuovo Cimento 37 1228.

[2] O. A. Shevchenko et al., 'Commissioning Status and further development of the Novosibirsk Multi-turn ERL', ERL13, Russia.

[3] D. Douglas et al., 'High average power UV FEL experiment at JLab', IPAC 2012, USA.

[4] Y. M. Saveliev et al., 'ALICE: Status, developments and scientific programme', IPAC 2012, USA.

[5] G. H. Hoffstaetter et al., 'Readiness for the Cornell ERL', IPAC2013, China.

[6] Science at the Hard X-ray Diffraction Limit (XDL2011), Cornell University, USA.

[7] From PICO to FEMTO, Workshop on time-resolved studies at BESSY II, 2015, Germany.

[8] Shim et al., JACS 127 (2007) 8825.

[9] Escalante et al., Nano Letters, 2010. 10(4): p. 1450-1457.

[10] M. Dell' Angela et al., 'Real-Time Observation of Surface Bond Breaking with an X-ray Laser', Science, Vol. 339 no. 6125, pp. 1302-1305.

[11] User and Staff FEL/Light Sources Publications, 2012, www.jlab.org/FEL/felpubs/.

[12] 2014 International Workshop on EUV and Soft X-Ray Sources, Ireland.

[13] R. Bartolini et al., 'Novel Lattice Upgrade Studies for Diamond Light Source', IPAC2013, China.

[14] M. Bär et al., 'BESSY VSR Scientific Case', 2013.

[15] K. Holldack et al., Phys. Rev. Lett. 97 (2006) 074801.

[16] K. L. Brown et al., 'TRANSPORT/360 A Computer Program for Designing Charged Particle Beam Transport Systems' SLAC-91. 1970.

[17] Jackson, 'Classical Electrodynamics', 1998.

[18] A. N. Matveenko et al., 'Isochronous Bend For High Gain Ring FEL', RuPAC, 2004, Russia.

[19] H. Wiedemann, 'Particle Accelerator Physics' Chapter 9, Springer-Verlag, 1993.

[20] E. L. Saldin et al, 'On the Coherent Radiation of an Electron Bunch Moving in an Arc of a Circle', TESLA FEL, 1996.

[21] Ya. S. Derbenev et al., 'Transverse Effects of Microbunch Radiative Interaction', SLAC-PUB-7181, June 1996.

[22] V. Yakimenko et al., "CSR shielding experiment", IPAC11, USA.

[23] http://projects.astec.ac.uk/ERLPManual/index.php/Main_Page

[24] K. Harada et al., 'Lattice and Optics Designs of the Test ERL in Japan', ERL07, UK.

[25] P. Castro, 'Beam trajectory calculations in bunch compressors of TTF2', April 7, 2003.

[26] Ries, Markus: Nonlinear momentum compaction and coherent synchrotron radiation at the Metrology Light Source low-alpha commissioning and development; Dissertation, Humboldt-Universität zu Berlin, Mathematisch-Naturwissenschaftliche Fakultät I , publiziert am 26.05.2014.

[27] R. Williams et al., 'The influence of high intensity terahertz radiation on mammalian cell adhesion, proliferation and differentiation', 2013 Phys. Med. Biol. 58 373.

[28] Y. M. Saveliev et al., 'Effect of DC Photo Injector gun voltage on beam dynamics in ALICE ERL', IPAC12, USA.

[29] F. Jackson et al., 'Longitudinal Beam Dynamics at the ALICE facility', IPAC12, USA.

[30] Image taken directly from official website, http://alice.stfc.ac.uk/files/Website/

[31] Picture courtesy of Yaroslav Getmanov, Budker INP, Russia.

[32] V. P. Bolotin et al., NIM A 557 (2006).

[33] O. A. Shevchenko private communications.

[34] M. Borland, 'elegant: A Flexible SDDS-Compliant Code for Accelerator Simulation', Advanced Photon Source LS-287, September 2000.

[35] R. D. Ryne et al., 'Large Scale Simulation of Synchrotron Radiation Using a Lienard-Wiechert Approach', IPAC 2012, USA.

[36] J. Wu et al., PAC 2001 USA, p.2866-2868.

[37] Hajima, 'R-Matrix Analysis of the CSR effect in a future ERL light source', APAC 2004, Korea.

[38] A. V. Bondarenko et al., 'Suppression techniques of CSR induced emittance growth in ERL Arcs', IPAC14, Germany.

[39] K. L. Brown, 'A First and Second-Order Matrix Theory for the Design of Beam Transport Systems and Charged Particle Spectrometers', SLAC Report-75, 1982.

[40] K. Wille, 'The Physics of Particle Accelerators', Oxford University Press, 2005.

[41] T. Atkinson, 'Accelerator Impedance, Beam Instability and Dynamics considerations in the BESSY II Booster Synchrotron', Internal Technical Report, 2009.

[42] M. Borland, 'Progress towards Ultimate Storage Ring light sources', IPAC12, USA.

[43] J. Knobloch et al., 'Status of the BERLinPro Energy Recovery Linac Project', IPAC 2012, USA.

[44] Petenev, Yuriy: Analysis of injection and recovery schemes for ERL based light source; Dissertation, Humboldt-Universität zu Berlin, Mathematisch-Naturwissenschaftliche Fakultät 1 , publiziert am 02.07.2014.

[45] ASTRA code, A Space Charge Tracking Algorithm, http://tesla.desy.de/∼meykopff/, 2012.

[46] A. N. Matveenko et al., 'Multi-turn ERL-based Synchrotron Light Facility: Injector Design', IPAC14, Germany.

[47] Z. Huang et al., 'Measurement of the LCLS laser Heater and its impact on the X-ray FEL performance', SLAC-PUB-13854.

[48] M. Borland, 'Simple method for particle tracking with coherent synchrotron radiation' Phys. Rev. ST, Vol 4, 070701 (2001).

[49] D. Angal-Kalinin, 'Emittance growth due to incoherent synchrotron radiation', 2nd CLIC Workshop, CERN 2008, Switzerland.

[50] T. Atkinson et al., 'Feasibility Study of Short Pulse Mode Operation for Multi-turn ERL Light Source', LINAC12, Israel.

[51] M. Scheer, 'WAVE - A Computer Code for the Tracking of Electrons through Magnetic Fields and the Calculation of Spontaneous Synchrotron Radiation', ICAP 2012, France.

[52] www.spring8.or.jp

[53] Q. Shen, 'CHESS Technical Memo', JLAB-ACT-01-04.

[54] I. V. Bazarov, 'Synchrotron radiation representation in phase space', Phys. Rev. ST Accel. Beams 15, 050703 (2012).

[55] http://flash.desy.de/accelerator/

[56] C. Behrens et al., 'Few-femtosecond time-resolved measurements of X-ray free-electron lasers', DOI:10.1038/ncomms4762, 2014.

[57] Z. Huang et al., 'Review of x-ray free-electron laser theory', Physical Rev. 10, 034801 (2007).

[58] S. Reiche, 'Numerical Studies for a Single Pass High Gain Free-Electron Laser', DESY-THESIS-2000-012.

[59] http://xfel.desy.de/technical_information/photon_beam_parameter/

[60] K. Bane et al., 'PEP-X Light Source at SLAC', Status Report, June 2008.

[61] G. Hofstaetter et al., 'Beam-breakup instability theory for the energy recovery linacs', Phys. Rev. ST AB 7, 054401 (2004).

[62] M. Liepe et al., 'RF parameter and field stability requirements for the cornell ERL prototype', PAC 2003, USA.

[63] A. Neumann et al., 'CW measurements of Cornell LLRF system at HOBICAT', SRF2011, USA.

[64] L. Merminga et al., 'High Current Energy Recovering Electron Linacs', Annu. Rev. Nucl. Part. Sci. 2003 p421.

[65] T. P. Wangler, 'RF Linear Accelerators', 2nd Edition, Wiley-VCH, 2008.

[66] Ya. V. Getmanov et al., 'Longitudinal Stability of ERLs with two Accelerating RF Structures', IPAC 2011, Spain.

[67] Ya. V. Getmanov et al., 'Longitudinal Stability of Multi-turn ERL with Split Acceleration Structure', IPAC2013, China.

[68] A. Matveenko et al., 'CDR for a multi-turn Energy Recovery Linac-based Synchrotron Light Facility (Femto-Science Factory)', HZB 2014.

Acknowledgements

I would particularly like to thank Prof. Dr. Alexander Matveenko for his unbridled support during my PhD. I am grateful for his dedicated interest in my work.

With regards to the continual support during my application process, contract negotiations and parental leave I would like to thank Prof. Andreas Jankowiak. It is a pleasure to work at HZB knowing you are well looked after by his management under the watchful eye of Frau Darowski.

Special thanks go to my colleagues Alexey, Yuriy, Oleg and Yaroslav. Their supervision and work ethic may have been Russian but I appreciated it.

Sincere recognition goes to my office colleague and dear friend Michael. It is a wonder that he is so faithful to me.

From the remaining HZB team, Axel, Jen and Stephan require a collective thankyou for the endless fruitful discussions.

Without the help and advice from Prof Nolting and his assistant Frau Götsch this whole university process would never have happened. They are both correctly devoted to students.

Finally, I have a young amusing family and will be forever in their debt.

Statement of authenticity

I certify that I have completed this work using only the cited literature and resources.

Selbständigkeitserklärung

Ich erkläre, dass ich die vorliegende Arbeit selbständig und nur unter Verwendung der angegebenen Literatur und Hilfsmittel angefertigt habe.

Berlin, den 24.03.2015 Terry Atkinson